Energy dependent time delays induced by Lorentz Invariance Violation: discriminating source-intrinsic effects with blazar modeling and preparation of population studies with H.E.S.S. MAGIC and VERITAS.

Christelle Levy

▶ **To cite this version:**

Christelle Levy. Energy dependent time delays induced by Lorentz Invariance Violation: discriminating source-intrinsic effects with blazar modeling and preparation of population studies with H.E.S.S. MAGIC and VERITAS. . General Relativity and Quantum Cosmology [gr-qc]. Sorbonne Université, 2021. English. tel-03521095

HAL Id: tel-03521095

https://tel.archives-ouvertes.fr/tel-03521095

Submitted on 11 Jan 2022

HAL is a multi-disciplinary open access archive for the deposit and dissemination of scientific research documents, whether they are published or not. The documents may come from teaching and research institutions in France or abroad, or from public or private research centers.

L'archive ouverte pluridisciplinaire **HAL**, est destinée au dépôt et à la diffusion de documents scientifiques de niveau recherche, publiés ou non, émanant des établissements d'enseignement et de recherche français ou étrangers, des laboratoires publics ou privés.

LPNHE PARIS

l'Observatoire de Paris | LUTH

Laboratoire de l'Univers et de ses Théories

PhD THESIS
OF SORBONNE UNIVERSITÉ

presented by

Christelle LEVY

Submitted in fulfilment of the requirements for the degree of
DOCTEUR DE SORBONNE UNIVERSITÉ

Speciality :

Physics of the Universe (STEP'UP - ED 560)

Energy dependent time delays induced by Lorentz Invariance Violation: discriminating source-intrinsic effects with blazar modeling and preparation of population studies with H.E.S.S., MAGIC and VERITAS.

Defended on *November 24th 2021* in front of the committee:

Mr	Jonathan	BITEAU	Examiner
Mr	Oscar	BLANCH	Referee
Mr	Julien	BOLMONT	Supervisor
Mr	Garett	COTTER	Examiner
Mrs	Elina	LINDFORS	Referee
Mr	Nikolaos	MAVROMATOS	Examiner
Mrs	Hélène	SOL	Supervisor
Mr	Pascal	VINCENT	President

cnrs IN2P3 Les deux infinis

SORBONNE UNIVERSITÉ CRÉATEURS DE FUTURS DEPUIS 1257

université PARIS DIDEROT PARIS 7

Acknowledgements

The last three years (and an extra couple months thanks to the global pandemic situation) that were spent to produce the work presented in this manuscript proved to be extremely rich, intense and a true rollercoaster of emotions. First and foremost, I want to thank Hélène and Julien who accepted to entrust me with this project and made this journey possible. I have been able to acquire a large spectrum of knowledge and grow into the capable physicist I am today thanks to their guidance. I also want to give very special thanks to Sami, aka my "coco(rico)-directeur", for his invaluable help and support during all this time, without whom this thesis would not have been this rich. And of course I thank all the jury members - Elina, Garret, Jonathan, Nick, Oscar and Pascal - for the challenging questions and input provided on this manuscript.

I want to thank all the members of the LIV task force - Alasdair, Cédric, Jelena, Manel, Michele, Tomislav and Tony - for their help in making this work what it is today. And a very special mention to Daniel for the support and many pieces of advice, as well as the fun and memorable times we had in Sydney, Corfu and of course Paris.

I also want to thank Jimmy (aka blue blink, aka DAQ killer), Sami (aka rabbit ears, aka meat lover, my fellow dino) and Volker (aka the red unicorn, our very special film director), but also Albert, Frikkie and Tony for the incredible and unforgettable time we had in shift in Namibia. Let the shifter song, the dino movie, the plane-proof-one-month-old-reblochon-based-tartiflette, the many and overpopulated barbecues, the run number (guinness-book-wannabe) record, the surprisingly calm "joystick at sunrise" moment, and many other memorable moments to be part of the H.E.S.S. anthology. I also want to thank Adelain, François and Sami (yes, again!) for the also unforgettable shift under the especially unfit sky of Adlershof. This will be remembered as the "let's bully the camera" shift as it was blinded, climbed on, sticked in a tree and ultimately set on fire.

Most of my time was spent at LPNHE which was never short of interactions. I would like to thank the members of the H.E.S.S. and CTA group, with a special mention to Jean-Philippe who always took the time to discuss and help me on any subject despite his more than overbooked schedule. The lab is home to an incredible and amazing community of PhD students, post-docs and interns which made the lunch breaks and coffee breaks truly playful and refreshing with the now ritual card games and after-work P&B parties. My thanks go to Ale, Alexander, Ariel, Christina, Enya, Emilie, Florian, Floriane, Giorgos, Guillaume, Jad, Louis d'E., Louis G., Lucile, Luis, Michele (again), Mykola, Reem, Renaud, Romain, Sara, Slava, Steffen, Ting, Vlada and so many others. A special mention goes to my longest standing office mates Gabriel and Julianna who made working hours particularly light and fun, and made the office a safe space to complain our hearts out but also be extatic, along with long and animated discussions

throughout the day. I also want to thank Mathieu, Olivier and Sophie for the many interesting interactions, support and genuine concern they showed during my hardest time.

Although it was not as much as I first intended to, I also had a wonderful and fulfilling time at LUTh. I want to thank Andreas, Catherine, Olivier, Pierre, Zacharia and the other members of the PHE group for all the rich and interesting discussions we had. I also want to thank the PhD students, with a special mention to Anna, Gaëtan, Jordan and of course my office mate and "PhD-step-brother" Anton for the fun we had and their game-changing input.

Because these three years would not have been the same without them, I want to thank the Magistère×(N+1)PAC crew - Alex, Dany, Doudou, Flo, Guillem, Joff, Léo, Louise, Loulou, Marine, Martin, Mic, Noé, Quentin, Robin, Thomachin, Zozo and all the others - for the cathartic parties. A special mention goes to Baptou and Eli my ex-roommates who are never short on puns and are now the founding-parents of the now institutional "gentille coloc", but also to Matmat my "almost-but-not-quite-coloc". I also want to give my most special thanks to No my former ex-roommate (and so much more!) and Nissa the prophet (and so much more!), my two most trusted and salvaging friends who were always there for me both in the brightest and darkest moments. The many all-you-can-eat sushi and endless games on Stardew, Borderlands and TESO with No, Nissa and Hervé were necessary to my well-functionning, especially during lock down. Of course I do not forget Arnaud (my partner in crime), Antoine, Carine, Célia, David, Flofinet, Flora, Florianne, Judee, Judy, Lucia, Michelle, Nelvin, Rémi, Robi, Sophie, Taher and Yolaine with whom I had a great time either these three years or before then. Last but not least, I want to thank Marie and Loki who avoided the writing phase of this manuscript to become a shipwreck.

Bien évidemment, je remercie également ma famille qui m'a toujours soutenue dans ce projet et tous les autres. Ma mère qui a toujours cru en moi. Mon père qui m'a donné ce goût pour la physique. Mon frère qui a toujours été un modèle pour moi. Ma tante et mes cousins qui sont à la fois la famille et mes amis les plus proches. Et enfin mes grands parents qui ont toujours été chaleureux. Un grand merci à tous.

Je tiens aussi à remercier Eric, Marie, Marylène, Papou et Vincent pour leur chaleureux accueil et leur bienveillance ces trois dernières années.

Finally, I want to thank Thomas, my most special person, who has been a pillar during these three years. We went through the thick and thin of our PhDs together. The emotional rollercoaster was all manageable thanks to you. You are the reason I was able to stand the pressure and this thesis would not have been here today if not for you.

December 8th, 2021

Contents

Liste des figures

Liste des tables

Introduction

One of the most challenging ambition of modern physics is to unify the realms of the infinitely small and infinitely large, currently described by quantum field theory and general relativity. This unification could be achieved through a still hypothetical unique quantum gravity theory that aims at describing physics at the Planck scale ($E_P \sim 19^{19}$ GeV) where the two realms should connect. Several tentative models have been proposed, amongst which string theories and loop quantum gravity appear as the most matured and popular approaches to build a universal theory. At present, no Earth based instrument is capable to attain the colossal energies typically involved in quantum gravity theories. Moreover, extracting observable predictions from these tentative models has been notoriously difficult. Constraining or rejecting such models is therefore a highly non trivial effort.

Nevertheless, specific models can give rise to effects that can be indirectly probed at currently accessible energies. One of which is a possible departure from the Lorentz symmetry at Planckian energies. This effect, which usually takes the form of a Lorentz invariance violation (LIV), can manifest through the alteration of the propagation of photons in vacuum. This leads to energy-dependent velocities inducing delays in the arrival time of gamma-ray photons with different energies. Provided very high energy photons propagate through very long distances, such delays are expected to be detectable.

A strategy currently in use to search for LIV signatures is to look for energy-dependent time delays in the gamma-ray signal coming from remote and variable cosmic sources such as active galactic nuclei (AGN), pulsars (PSR) and gamma-ray bursts (GRB) detected at TeV energies with imaging atmospheric Cherenkov telescopes. However, time delays can also be generated from the intrinsic radiative processes at work in the sources which are yet to be properly disentangled from LIV-induced time delays. One way to address this issue is the study of these intrinsic effects through the modelisation of sources emission mechanisms. Considering intrinsic time delays are not expected to directly depend on the distance, contrary to LIV-induced ones, another discrimination strategy relies on population studies involving a large number of sources over a broad range of redshifts.

This thesis attempts to explore these two approaches and proposes analysis tools for the discrimination between LIV and intrinsic effects. This manuscript is separated in three parts.

Part I focuses on the scientific framework. We start with an introduction on quantum gravity, LIV and the associated phenomenology in Chapter 1. We then continue with a presentation of blazars and discuss their emission properties in Chapter 2, followed by the different methods of detection brought by contemporary gamma-ray astronomy in Chapter 3.

Part II focuses on the interpretation of intrinsic time delays arising from blazar modeling along with tools that can be used for discrimination. The model, based on a leptonic synchrotron

self-Compton scenario, is specified in the first part of Chapter 4. The associated intrinsic time delays are then fully characterised and interpreted in the second part of this chapter. Chapter 5 presents a multi-frequency study highlighting for the first time a strong correlation and symmetry between intrinsic time delays in the X-ray (unaffected by LIV) and gamma-ray (where LIV effects could arise) domains. Analysis tools are proposed to achieve proper discrimination.

Finally, Part III focuses on population studies. Chapter 6 summarises the current state of the art when it comes to LIV time-of-flight studies, with the different analysis techniques and most notable results. A preparation for actual population studies is reported on Chapter 7 with the presentation and testing of a new multi-source analysis tool, along with the first results obtained from realistic simulations of GRB, AGN and PSR signals and their interpretation.

Part I

Scientific Framework

Chapter 1

Quantum gravity and departures from Lorentz invariance tested with photons from astrophysical sources

Contents

The four fundamental interactions known to exist today have been described by two contemporary theories. On the one hand, general relativity describes the dynamic of large scale objects governed by gravitation understood as the manifestation of spacetime curvature. On the other hand, quantum field theory (QFT) gave rise to the standard model of particle physics that classifies elementary particles and describes their interactions - electromagnetic, strong and weak forces - as quantised fields mediated by bosons - photons, gluons, and W and Z bosons respectively. Both theories have proven to be extremely successful and are today the best confirmed set of fundamental theories with notably the recent discoveries of gravitational waves [1] and of the Higgs boson [2, 3].

They however both suffer from some failures indicating they are incomplete, especially when quantum and gravitational effects are at the same scale. This limit is known as the Planck scale and is defined by characteristic time t_P, length l_P, mass m_P and energy E_P:

$$t_P = \sqrt{\frac{\hbar G}{c^5}} \sim 5.39 \times 10^{-44}\ \text{s}, \tag{1.1}$$

$$l_P = \sqrt{\frac{\hbar G}{c^2}} \sim 1.6 \times 10^{-35}\ \text{m}, \tag{1.2}$$

$$m_P = \sqrt{\frac{\hbar c}{G}} \sim 2.18 \times 10^{-8}\ \text{kg}, \tag{1.3}$$

$$E_P = \sqrt{\frac{\hbar c^5}{G}} \sim 1.22 \times 10^{19}\ \text{GeV}, \tag{1.4}$$

with $c \sim 3 \times 10^8$ m.s^{-1} the speed of light in vacuum, $\hbar = h/2\pi \sim 6.58 \times 10^{-16}$ eV.s the reduced Planck constant and $G \sim 6.67 \times 10^{-11}$ m^3.kg^{-1}.s^{-2} the universal gravitational constant. In particular, general relativity allows the existence of singularities where spacetime curvature becomes infinite, typically in the very early universe and inside black holes. Alternatively, the standard model is built on special relativity where spacetime is assumed to be flat (Minkowski spacetime). Since gravity can only arise from a curved spacetime, gravitational interaction are made impossible in this formalism.

One could expect to circumvent these issues by simply combining general relativity and QFT in a single framework that describes all four interactions. Unifying formalisms are generally labeled quantum gravity (QG) theories. Two approaches can be explored: either understand the quantum gravity theory as a properly quantised general theory of relativity completed by the standard model; or view general relativity and QFT as effective field theories i.e. a low energy/large scale limit of a more general and yet unknown theory of quantum gravity.

Generally speaking, the first approach aims at combining theories with dramatically opposed properties. On the one hand, general relativity is a classical, deterministic and background independent (i.e. where spacetime is a physical entity that can interact with other entities) framework. On the other hand, QFT is quantum, probabilistic and relies on a fixed non-dynamical background (i.e. spacetime is a scene or setting that does not interact with physical entities). It so happens we do know how to infuse quantum mechanical effects into gravity, but only up to the Planckian scale. As the energy (or the distance) gets closer to the Planck scale, the theory

can be renormalised modulo an increasing number of parameters to absorb the infinities that occur in calculations. Past the Planckian limit, the number of parameters grows to become infinite and the theory is no longer renormalisable. As a consequence, it loses its predictivity and becomes unavailing. Alternatively, gravity has been introduced in the QFT formalism by modifying the presupposed flat spacetime to a curved one. The most notable success of this approach was the discovery of the Hawking radiation *evaporating* from black holes. However, it suffers from similar issues, the theory becoming non-renormalisable nearing the Planckian scale.

In the next section, we instead explore the second approach by viewing general relativity and QFT as effective field theories.

1.1 Quantum gravity built on effective field theories

This section benefits from reading [4], [5], [6], [7] and [8].

At present, there are many approaches to the open question on how to quantise gravity, amongst which string theories (ST) and loop quantum gravity (LQG) are considered the most popular and matured effective field theories as of today. Non-commutative geometry [9], asymptotic safety [10], group field theory [11] or causal dynamical triangulation [12] are examples of other notable approaches. For a complete review on quantum gravity searches, the reader is invited to refer to [13]. In this section, I give an overview of string theories and LQG which go beyond the scope of this thesis.

String theories and LQG both solve the renormalisation issue by introducing elementary objects with a finite size, getting rid of infinities brought by point-like objects or smooth geometry in general relativity or QFT. They however tackle the problem starting from two very distinct philosophies which leads them to diverge on results. While ST easily recovers low energy limits theories, it struggles to describe Planck scale quantum spacetime. In contrast, LQG manages to quantise spacetime and describe it at Planckian scale but struggles to link it to the low energy physics.

1.1.1 String theories

String theories (ST) provide a picture where fundamental particles are no longer viewed as point-like but one-dimensional objects with a finite extent [7]. These objects, called strings, evolve in a smooth and continuous background spacetime and have vibrational modes which are interpreted as particles (perturbation theory). In that sense, string theories are closer in nature to QFT rather than to general relativity. They were initially developed by particle physicists to describe the strong interaction before Quantum Chromodynamics was favored in the standard model. It was nonetheless soon realised the string formalism necessarily includes a massless particle of spin 2 that can be identified as a graviton, a boson carrying the gravitational interaction. String theories then naturally became candidates for a quantum theory of gravity.

Strings can be either open or closed, and of bosonic or fermionic nature. Depending on their characteristics, different theories can be built. However, physical and theoretical consistency systematically requires strings to live in a spacetime with a number of dimensions that is not compatible with the observed $3+1$ dimensions accessible at current energies: 26 for bosonic strings, 11 for the M-theory or 10 for the supersymmetric strings. To correct for this discrepancy,

the extra dimensions are compactified with processes that introduce large amount of arbitrariness in the predicted mass and spin of particles. Furthermore, all of these theories require the use of supersymmetry which is progressively being ruled out as predictions are disputed by observations from the large hadron collider (LHC) experiment [14].

Then again, contrary to any other approaches, string theories provide with a truly unified view of the four fundamental interactions, instead of considering quantum gravity as a separate problem. Furthermore, it is able to describe everything there is with a single "master entity". There is only one unknown and adjustable parameter, the string length l_s. This parameter, which is the only measurement that would be needed to make predictions on gravitational interactions at arbitrary distances, has to be determined by experiment. The string length is however expected to be of the order of the Planck length $l_P \sim 10^{-35}$ m which is way beyond any contemporary detector capability.

Interestingly enough, string theories come up with their own cosmology. They introduce a class of extended objects called D-branes (hypersurfaces of D-dimension) evolving in a higher-dimensional space called bulk. Open strings must be attached to these branes from which they cannot escape, and make up for the matter contained in the brane they are linked to. Closed strings on the other hand can freely travel between branes. As a consequence, since our Universe is presumed to be a compactified three-dimensional brane, it is impossible to check whether other D-branes exist or not. The origin of time and matter (Big Bang) is then supposed to be the result of a collision between our universe and another D-brane [15].

1.1.2 Loop quantum gravity

LQG starts from a radically different concept. This picture gives up on the notion of smooth and continuous background geometry, and replaces it with one that is discrete and built out of elementary quantum objects [8]. This theory does not attempt to unify the fundamental interactions, but rather build a background independent QFT (diffeomorphism invariant). Although it is built on quantum mechanics fundamentals (Hilbert space, quantum field operators, transition amplitudes, etc.), LQG concept of spacetime is closer to the general relativity one as it stands as a non-perturbative theory.

The elementary objects used to build spacetime are "simplices", i.e. elementary geometric objects (vertex, line segment, triangle, tetrahedron, etc.), that are linked together with holonomies (operators) to create loop states. As a way to oversimplify the underlying concepts, we can view spacetime as a collection of these loops stacked together like Lego® bricks. Distance would then be given by the number of lined-up loops, while time is assimilated to how these loops continuously transform in one another or the number of steps needed for these transformations. In this theory, as there is no fixed background, only coordinates independent quantities are physical: only the relative position of a loop with respect to others is significant.

Although LQG is successful at describing a non-perturbative discrete spacetime at Planck scale, one will find difficulties in recovering the low energy classical limit (i.e. general relativity). More precisely, difficulties arise when it comes to building a smooth and continuous spacetime out of simplices. Furthermore, there remains the open question on how to describe elementary particles (e.g. quarks, electrons, neutrinos) in terms of quanta of geometry.

Similarly to string theories, LQG comes up with its own cosmology which gave birth to the subfield known as loop quantum cosmology (LQC). It gives a minimal size to the initial state of the Universe, getting rid of the Big Bang singularity. Instead, LQC formulates a periodic cosmological model involving what is called the "Big Bounce". In this picture, the Universe alternates between the Big Bang (expansion up a maximal size) and the so-called Big Crunch (collapse down to a minimal size). The Big Bounce then describes events where the Big Bang immediately follows the Big Crunch. However, LQC requires for the Universe to decelerate following a Big Bang episode in order for the Big Crunch to take over and initiate, which are in contradiction with actual observations of the Universe accelerating expansion.

1.2 Departures from Lorentz invariance

This section benefits from reading [13]

Special relativity, which is the building foundation for both general relativity and QFT, make all physical phenomena appear the same to inertial observers. It relates long wavelengths to short ones through Lorentz symmetry, thus implying spacetime should be the same at all length scales. As indicated above, quantum gravity theories give a different picture of spacetime with an either foamy or discrete nature that becomes perceptible to physical objects at lengths or energies near the Planck scale. This fuzzy structure occurs as a consequence of spacetime discreteness, its non-commutativity or dimension reduction. A small number of very specific quantum gravity models predict a departure from Lorentz invariance, either breaking or deforming the symmetry, when physical objects interact with spacetime fuzziness. Lorentz invariance is then viewed as an emergent symmetry at low energies (in effective field theories) which is lost beyond Planck scale.

1.2.1 Breaking Lorentz symmetry

Rather than deforming Lorentz symmetry, the few quantum gravity models that tamper with Lorentz invariance tend to break it, leading to a proper Lorentz invariance violation (LIV). Observers connected by a Lorentz boost[1] would then describe different laws of physics. This implies the existence of a preferred frame of reference in which Lorentz violation is small and these laws take a specific form. Contemporary cosmology suggests this frame could be the reference system at rest with respect to the cosmic microwave background (CMB).

LIV has been introduced in several ways in quantum gravity models, with different ways to describe spacetime fuzziness. String theories allows for Lorentz symmetry to be spontaneously broken in the early Universe. It can introduce small relic background fields (vacuum expectations value) which point in a chosen direction and spread through spacetime. This implies there should exist preferred directions in spacetime for particles interaction leading to a modification of their dispersion relation. This effect has been studied in the standard model extended (SME) [16] which describes all particles interaction when Lorentz invariance is broken for particles while being retained for observers.

Alternatively, another approach to string theory labeled "Liouville cosmology" [17] introduces fluctuations to spacetime (aka "foam") in the form of point-like D0-branes resulting in the vacuum

[1] Lorentz transformations include both boosts and rotations. Most of the time, quantum gravity models that break the symmetry only suffer from a loss of boost invariance while retaining the rotational one.

behaving as a dispersive medium. Elementary particles are then predicted to undergo stochastic effects leading to a modification of dispersion relations and violations of Lorentz invariance.

LQG models should predict a similar dispersion effect due to the discrete nature of spacetime they work with. One can refer to the semi-classical approach introduced by Gambini and Pullin [18] which steers such dispersion effects along with an intrinsic birefringence of spacetime.

1.2.2 Deforming Lorentz symmetry

A more recent approach to departure from Lorentz invariance called doubly special relativity (DSR) modifies special relativity to introduce a second invariant quantity [19, 20]. In addition to the in-vacuo speed of light c, there is now a fundamental inverse-momentum (or equivalently a length) we will denote here l_{DSR}. This picture aims to conciliate the contradicting concepts of unbound length contraction in special relativity and minimal length (quanta of distance) in quantum gravity. This formalism introduces a curved momentum space with constant curvature, which is associated to the observer-independent inverse-momentum l_{DSR}. As a consequence, the energy-momentum dispersion relation would be different for each observer. In order to retain Lorentz invariance, the laws of transformation between inertial frames and composition of momenta need to be modified. In other words the energy-momentum conservation laws are necessarily deformed in this formalism and become observer-dependent (i.e. depend on l_{DSR}).

DSR models are commonly viewed as effective (i.e. low energy) descriptions of a flat-spacetime limit of quantum gravity. In this picture, the minimal length is replaced by an energy or momentum cut-off, and the spacetime fuzziness vanishes (preventing any stochastic effect breaking Lorentz symmetry) while maintaining momentum space curvature (leading to a deformation of Lorentz symmetry). Current searches on the DSR formalism aim at generalising this picture to a curved spacetime.

1.3 Phenomenology

The ST and LQG models considered above yield a departure from Lorentz invariance as a consequence of a modified energy-momentum dispersion relation (MDR). Each formalism predicts a specific MDR which affects given elementary massless (or nearly so) particles depending on the underlying modification of Lorentz symmetry, leading to a similar but not identical set of phenomenological predictions. Most notably, MDR can steer time-of-flight difference between matter fields, a modification of kinematics for particles interaction, but also a birefringent, fuzzy or foamy nature of vacuum. Processes forbidden in the special relativity framework will also be forbidden in DSR approaches, but may be allowed in LIV formalisms. In contrast, processes allowed in both formalisms will yield more virulent phenomenological effects with formalisms incorporating a broken (LIV) rather than deformed (DSR) Lorentz symmetry.

Nevertheless, the family of MDR yielded by these distinct models can be represented with a single toy-model built from the standard low-energy dispersion relation for massless particles corrected over n orders of magnitude:

$$E^2 \simeq p^2c^2 \times \left[1 \pm \sum_{n=1}^{\infty} \left(\frac{E}{E_{QG}}\right)^n\right] \tag{1.5}$$

with E_{QG} the characteristic quantum gravity energy scale expected to approach the Planck energy E_P. One can therefore anticipate very tiny phenomenological effects at currently accessible energies[2]. Having negligible LIV or DSR effects is equivalent to $E_{QG} \to \infty$ where correction terms vanish and one recovers the standard dispersion relation.

The observation of a deviation from the standard dispersion relation would indicate quantum gravity models breaking Lorentz invariance are on the right track. However, it would not be enough to properly distinguish between them. Alternatively, measuring $E_{QG} \gg E_P$ would indicate these models should be rejected. Considering the sensitivity of current experiments, this phenomenology is limited to the first two orders of correction $n = 1$ and $n = 2$.

1.3.1 Time delays

From Equation 1.5 one can derive the group velocity of massless particles propagating in vacuum:

$$v_g(E) = \frac{\partial E}{\partial p} \simeq c \times \left[1 \pm \frac{n+1}{2} \left(\frac{E}{E_{QG}}\right)^n\right]. \tag{1.6}$$

The $\pm$ sign allows both subluminal and superluminal velocities. This new expression allows massless (or nearly so) particles - photons, neutrinos and gravitational waves - with distinct energies to propagate with a different speed through an LIV or DSR modified nature of vacuum. As a consequence, it is expected for two massless particles i and j with energies $E_i < E_j$ differing by amount $\Delta E = E_j - E_i$, supposedly emitted simultaneously from a source located at a euclidian distance d from the detector, to be observed with a time delay $\Delta t \neq 0$. First introduced by Amelino-Camelia et al. [21], the relative time lag between particles can be obtained by integrating Equation 1.6 over time and reads:

$$\Delta t = \pm \frac{n+1}{2} \frac{\Delta E^n}{E_{QG}^n} \times \frac{d}{c} \tag{1.7}$$

with $\Delta E^n = E_j^n - E_i^n$ the particles energy difference at order n. As both time and energy are measured quantites, it is a common practice to work instead with the time delay over energy difference noted τ_n and defined as:

$$\tau_n = \frac{\Delta t}{\Delta E^n} = \pm \frac{n+1}{2} \frac{1}{E_{QG}^n} \times \kappa(d) \tag{1.8}$$

where a new notation for the propagation term is introduced as $\kappa(d) = d/c$. The quantity τ_n will usually be given in units of s.TeV^{-n}.

As mentionned above, since it is generally expected to have $E_{QG} = \mathcal{O}(E_P)$, the phenomenological effects are expected to be tiny at currently accessible energies. For the sake of illustration, let's consider two photons of energy $E_i = 1$ TeV and $E_j = 2$ TeV, and take $E_{QG} = E_P \sim 10^{16}$ TeV. This yields a time difference between the respective time-of-flight at first order correction $n = 1$ of $\Delta t \sim d \times 10^{-24}$ s. In comparison, the typical unit for extragalactic distance is either the parsec (pc) where 1 Mpc $\sim 3 \times 10^{22}$ m, or the redshift z where $z = 1$ is approximately equivalent to 10^{26} m. Taking for instance a source located at 100 Mpc ($z \sim 0.024$), the time difference would

[2] Hundreds of TeV for massless particles emitted by astrophysical sources, or tens of TeV when generated in Earth-based accelerators.

be of order $\Delta t = \mathcal{O}(10^{-2})$ s. This simple calculation suggests astrophysical emittors are natural candidates for time-of-flight studies.

Now that we are considering astrophysical sources and cosmological distances, it is necessary to modify Equation 1.7 to account for the Universe expansion. The computation of time-of-flight difference that incorporates cosmological corrections was first proposed in [22] and later corrected by Jacob and Piran in [23]. The propagation term was derived starting from the MDR given in Equation 1.5, making it an especially fitting description of the comoving trajectories of massless and ultrarelativistic particles when LIV effects are at play. It was however pointed out this calculation may be too simplistic as it presupposes translations not to be affected by Planck-scale effects [24]. The term $\kappa(d) = d/c$ in Equation 1.8 is now replaced by an expression that depends on both the correction order n and the redshift z:

$$\kappa_n^{J\&P}(z) \equiv \frac{1}{H_0}\int_0^z \frac{(1+z')^n dz'}{\sqrt{\Omega_m (1+z')^3 + \Omega_\Lambda}} \tag{1.9}$$

with H_0 the Hubble constant, Ω_m the matter density parameter and Ω_Λ the dark-energy density parameter. Although there is no consensus yet on the values they should be assigned with, the precision on LIV studies blurs these uncertainties on cosmological parameters and does not strongly affect their final results. In the rest of the manuscript, we will use $H_0 = 67.74 \pm 0.46$ km.s^{-1}.Mpc^{-1}, $\Omega_m = 0.3089 \pm 0.0062$ and $\Omega_\Lambda = 0.6911 \pm 0.0062$ as given in [25].

In DSR approaches the in-vacuo Lorentz invariant dispersion relation is more complex as it accounts for both momentum space curvature and cosmological expansion. The associated empirical time delay formula was first introduced by Rosati et al. in [20] where, once again, only the propagation term $\kappa(d) = d/c$ in Equation 1.8 is replaced by a more complex expression given by:

$$\kappa_n^{DSR}(z) \equiv \int_0^z \frac{1}{(1+z')^n} \frac{h^{2n}(z')dz'}{\sqrt{\Omega_m (1+z')^3 + \Omega_\Lambda}} \tag{1.10}$$

with

$$h(z') \equiv 1 + z' - \sqrt{\Omega_m (1+z')^3 + \Omega_\Lambda} \int_0^{z'} \frac{dz''}{\sqrt{\Omega_m (1+z'')^3 + \Omega_\Lambda}}. \tag{1.11}$$

Amongst the massless (or nearly so) particles cited above, neutrinos and gravitational waves are particularly hard to detect, leaving only photons as serious candidates and target of choice for such studies. Time-of-flight studies with astrophysical photonic emission and search for time delays in the observational data will be the main focus of this work. We still present in more details the modification of particle interaction kinematics as it could be coexisting with time-of-flight effects.

1.3.2 Kinematic interactions and threshold effects

A MDR can lead to a modification of kinematic interactions between particles. In particular, it can change the energy threshold at which a given physical process is allowed to happen. As mentioned before, the extent of these modifications depends on whether the Lorentz invariance is properly broken or simply deformed. LIV and DSR formalisms will therefore steer different phenomenological predictions. Processes that are forbidden by special relativity - i.e. for which the energy threshold is not defined - are also forbidden in DSR approaches. In contrast, LIV

approaches can steer a new energy threshold thanks to the existence of a preferred frame of reference. Newly allowed processes notably include vacuum Cherenkov radiation ($e^{\pm} \to e^{\pm}\gamma$), photon decay in vacuum ($\gamma \to e^{+}e^{-}$) or photon splitting ($\gamma \to 3\gamma$). As a consequence, Lorentz symmetry breaking formalisms are of particular interest for this type of phenomenology.

Amongst the processes allowed with both approaches, a notable effect is the modification of the pair production ($\gamma\gamma \to e^{+}e^{-}$) energy threshold. The LIV-modified (first order) energy threshold for pair production from a head-on collision with both leptons at rest is given by:

$$\epsilon_{th} = \frac{(m_e c^2)^2}{E_\gamma}\left[1 \pm \frac{1}{4}\left(\frac{E_\gamma}{E_{LIV}}\right)^{n+2}\right], \tag{1.12}$$

with E_γ the incident photon energy, $m_e c^2$ the electron rest mass and $E_{LIV} = 29.6 \times (E_{QG,1}/E_P)^{1/3}$ TeV. The threshold is allowed to be either increased or decreased by the $\pm$ sign. The classical limit can be recovered for $E_{LIV} \to \infty$ leading the correction terms to vanish. Similarly to the time delay effects, the modification of the energy threshold is expected to be tiny at currently accessible energies. This effect can be efficiently tested with the monitoring of high energy photon flux propagating through cosmological distances. In such case, a correction term accounting for cosmological effects must be added and Equation 1.12 is modified as follows:

$$\epsilon_{th} \longrightarrow \frac{\epsilon_{th}}{1+z} \tag{1.13}$$

with z the source redshift.

Particles emitted by astrophysical sources encounter absorbing medium on their way to Earth. In particular, high energy photons can interact with what is known as the extragalactic background light (EBL), a diffuse emission filling the Universe and made up of all the light produced by all the sources throughout cosmic history[3] which spectrum can be seen in Figure 1.1. As a consequence, the high energy flux tends to be attenuated by the EBL absorption. In the classical limit, interactions with the EBL opens for E_γ between[4] 10 GeV and 100 TeV and can significantly absorb the VHE photons depending on the source distance[5]. In the equivalent superluminal case, the threshold is lowered and photons undergo a stronger absorption leading to steeper energy spectra. Alternatively, the equivalent subluminal case (which is generally preferred) yields a higher threshold leading to a reduction of very high energy (VHE) photon absorption and less attenuated energy spectra. Figure 1.2 shows the pair production interaction energy threshold for various values of E_{QG} at linear order.

[3] The CMB constitutes a fraction of the EBL spectrum defined in the 0.03 - 100 cm wavelength domain.

[4] From Equation 1.12 at first order, $E_\gamma \sim 10^{-11}/\epsilon_{th}$. From Figure 1.1, the EBL is in the wavelength window defined by $10^{-7}\,\mathrm{m} < \lambda_{ebl} < 10^{-3}\,\mathrm{m}$, which is equivalent to the energy window $10\,\mathrm{eV} > \epsilon_{th,ebl} > 10^{-3}\,\mathrm{eV}$. Interactions with the EBL is therefore allowed for photons with energy $10^{10}\,\mathrm{eV} < E_\gamma < 10^{14}\,\mathrm{eV}$. At energies smaller than ~ 10 GeV, the X-ray and gamma-ray diffuse photon field are taking over the interaction process.

[5] There exists a distance $z_h(E_\gamma)$ (the gamma-ray horizon) at which point the Universe becomes optically thick to photons with energy larger than E_γ along the line of sight. This horizon gets closer as E_γ gets larger. The observation of extragalactic and cosmological sources are usually limited to photons energy reaching up to a few TeV at maximum while observed galactic source photons can reach tens or hundreds of TeV. At energies smaller than ~ 10 GeV, the diffuse photon field becomes nearly optically transparent to incident photons, regardless of the source's redshift.

Although these two phenomenological aspects - differences in time-of-flights and the modification of kinematic interactions - are usually treated and studied separately, one could expect massless particles to be affected by both effects simultaneously. Such a scenario is briefly explored and discussed in a later chapter. We invite the reader to refer to Section 5.3 for more details.

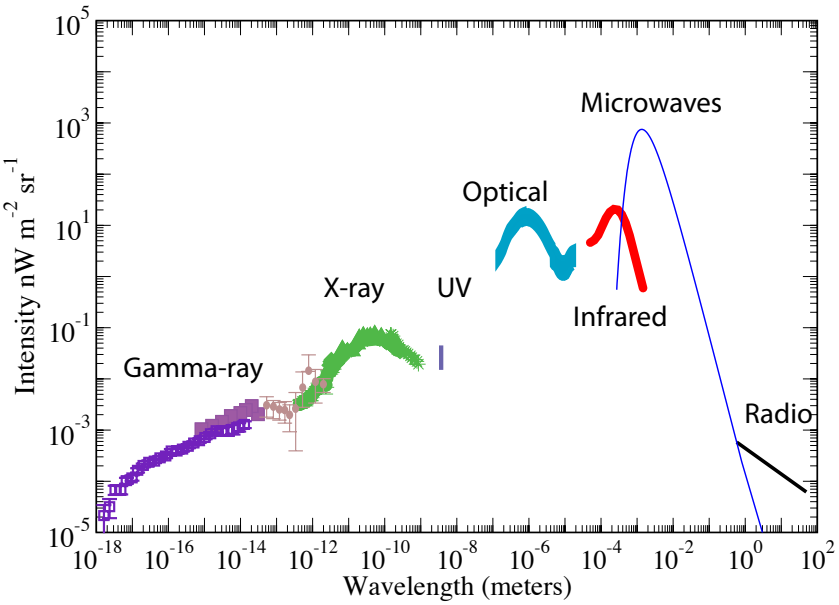

Figure 1.1: Intensity of the extragalactic background light as a function of the wavelength. Interaction with EBL photons (wavelength between $\sim 10^{-7}$ and 10^{-3} m) opens for gamma-rays between 10 GeV and 100 TeV. Figure extracted from [26].

1.4 Astrophysical probes

As mentioned above, the quantum gravity and related phenomenological effects are expected to be small. It is of interest to choose sources of photons which help maximise them. The measurable quantity associated to time-of-flight studies is given in Equation 1.8, which can be maximised for sources emitting photons:

- over large distances, ideally cosmological;
- distributed over a high-valued and large energy band, to maximise the term ΔE^n.

Moreover, the measurement of time delays can only be performed over photon emissions that show some variability. The higher the variability, the better the precision on that measurement. Transient or periodic astrophysical sources emitting VHE photons (E > 1 GeV) are therefore of particular interest for LIV time-of-flight studies. Three candidate sources fit this description: gamma-ray bursts, pulsars and flaring active galactic nuclei. This section gives a brief overview of these objects. A review on the state of art for LIV studies performed with such sources can be found in Chapter 6.

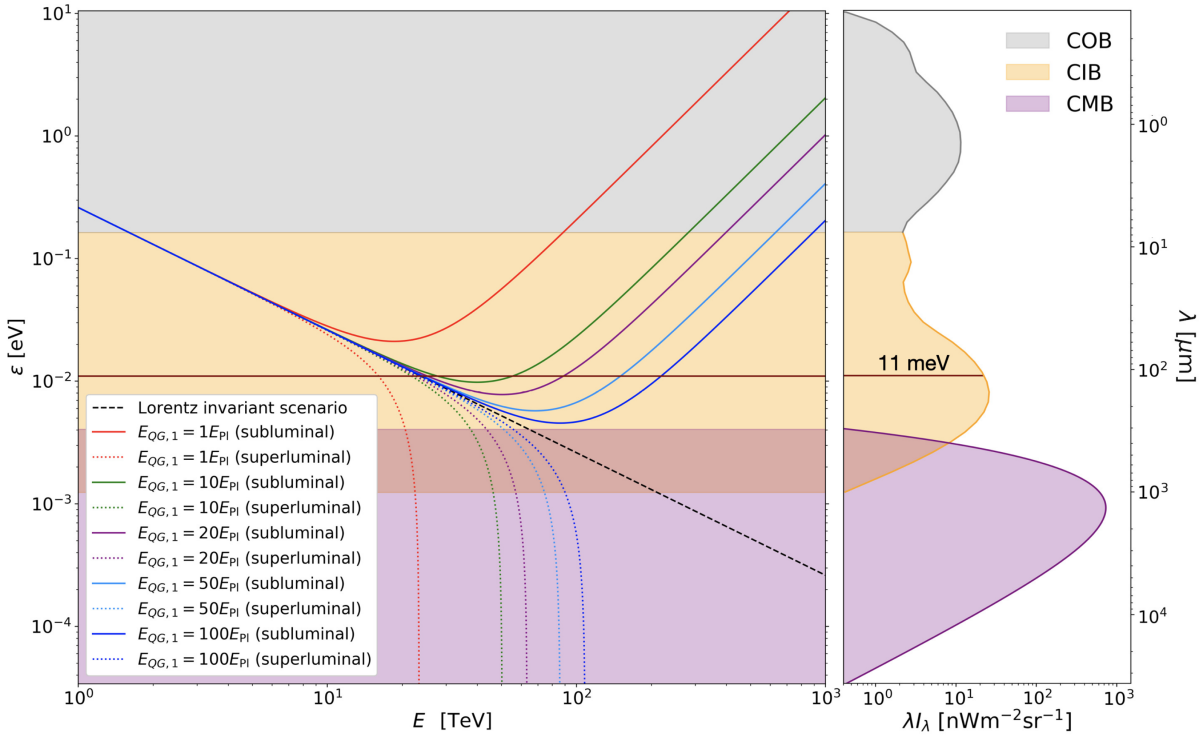

Figure 1.2: Evolution of the background photon energy threshold ϵ_{th} (here noted ϵ) for pair production reaction as a function of a gamma-ray energy E_γ (here noted E). Left panel: evolution of ϵ_{th} for various LIV effects at first order encoded by $E_{QG,1}$ for redshift $z = 0$. Right panel: spectral energy distribution of the cosmic background light in the optical (COB), infrared (CIB) and microwave (CMB) domains. Credit: [27].

1.4.1 Gamma-ray bursts

Gamma-ray bursts (GRB) [28] are extra-galactic transient and random phenomena releasing a tremendous amount of energy reaching typically $10^{54} \sim 10^{54}$ erg.[6] They are characterised by a short burst of intense emission (prompt phase) lasting from miliseconds to a few hundred of seconds, followed by a long-lasting phase (afterglow) where the observed flux and photon energy quickly decrease over a period of hours up to several days. The widely accepted picture describes GRBs as newborn black holes associated to a relativistic jet (i.e. a collimated outflow of relativistic particles) as shown in Figure 1.3.

GRBs are sorted out into two distinct classes depending on their duration. Long GRBs characterised by a prompt emission lasting typically longer than 2 seconds represent the vast majority of these objects. Since they are thought to be associated with nearby supernovae, long GRBs are believed to originate from the collapse of fast rotating massive stars. The rest of the population is gathered in the short GRB class. Their rare occurrence makes it difficult to determine their origin. They are however believed to be connected to the merging of compact

[6] 1 erg is equivalent to 10^{-7} J generally used to characterise astrophysical phenomena. For comparison, the total energy radiated by a supernova typically reaches 10^{49} erg.

objects (two neutron stars or a neutron star and a black hole)[7].

In light of their cosmological distance (observed up to $z = 9.4$), highly energetic emission and fast variability, they are ideal sources to probe LIV. However, the redshift cannot be measured or estimated for all bursts. Furthermore their random and sporadic appearance makes them particularly difficult to catch, especially for ground-based detectors due to their narrow field of views. Alternatively, they can be easily detected with satellite-embarked wide-field detectors, but their small collection area greatly limits the highly energetic photon detection. More details will be given on this subject in Chapter 3.

1.4.2 Pulsars

Pulsars [30], also noted PSR[8], are highly magnetised and fast rotating neutron stars created from the death of a massive star that exploded into a supernova. While the outer layers are blown out into a supernova remnant, the core of the star collapses under the action of gravity. The leftover electrons and protons combine to form neutrons highly condensed in a newly formed neutron star. The angular momentum being conserved during the process, the neutron star rotates with a very short period ranging from tens of seconds down to a few milliseconds. A part of the rotational energy is lost under the form of electromagnetic radiation, making pulsars comparable to a magnetic dipole emitting highly energetic particles in the form of collimated outflows originating at each magnetic pole. As a consequence, the pulsar rotation slows down with time. When these poles are not aligned with the rotation axis, pulsars are seen as pulsating objects with a periodic emission. An illustration can be seen in Figure 1.4.

Contrary to GRBs, pulsars are fixed and continuously emitting sources. The very fast variability - and consequently sharply peaked photon emission - allows for a very good precision on time delay measurement. On the down side, they are "local" galactic objects located at short distances such that lesser LIV effects are to be expected. However, this locality lessens the EBL absorption resulting in energy spectra being less attenuated at TeV energies.

1.4.3 Flaring active galactic nuclei

Active galactic nuclei (AGN) are the core of distant galaxies hosting a central supermassive black hole fed by a surrounding accretion disc mainly made up of gas and dust. About 10% of the observed galaxies possess such a system which is referred as the central engine. It is further surrounded by a larger torus of gas and dust, along with the so-called broad and narrow line region (BLR and NLR) made up of ionised gas. The accretion disc which emits light in the optical/UV spectrum can be obscured by the surrounding torus, which emits in the IR spectrum, depending on the viewing angle. The BLR and NLR reprocess the disc emission into spectral emission lines. The central engine emission is intense enough (typically between 10^{51} and 10^{54} erg.s^{-1}.cm^{-2}) to overshadow the light emitted by the galaxy itself.

In roughly 10% of AGNs, a fraction of the accreted gas infalling into the black hole is ejected in the form of two luminous extended jets of relativistic and magnetised plasma. Such AGNs are labeled as radio loud, as opposed to radio quiet AGNs where the jet, if any, would emit very low

[7] This has been further confirmed by the detetion of GRB 170817A that followed the gravitational wave merger event GW 170817 [29]

[8] PSR is actually the name of a catalog of pulsar sources, used in this work as an acronym for pulsars.

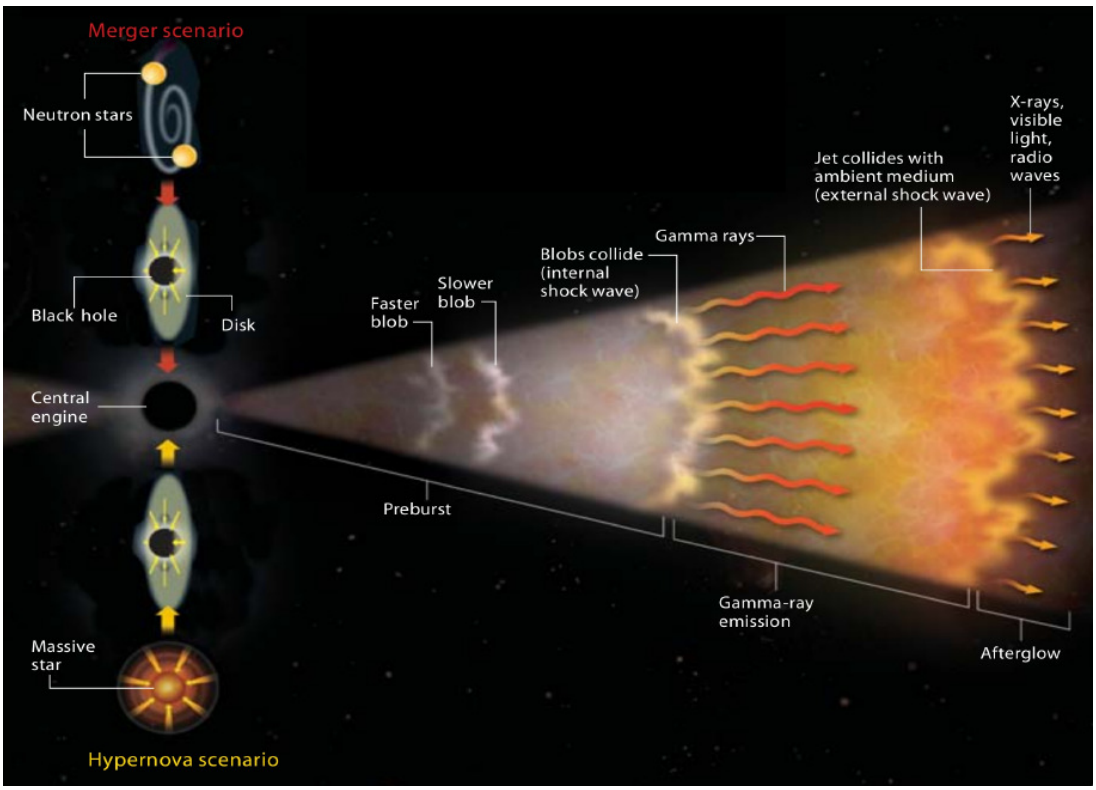

Figure 1.3: Illustration of the commonly accepted view of a gamma-ray burst (prompt phase and afterglow), displaying a core black hole and a relativistic jet. The merger and supernovae scenarii are the two phenomena thought to be at the origin of GRBs. Credit: [28].

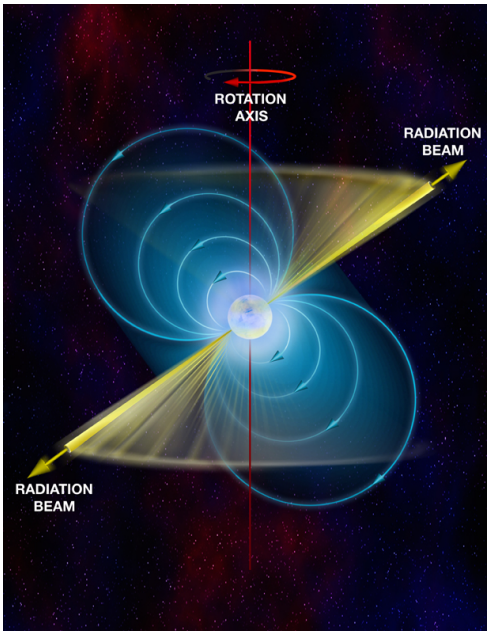

Figure 1.4: Illustration of a pulsar, a fast rotating neutron star displaying two beams of particles at each magnetic pole. The pulsation is a consequence of the misalignment between the magnetic poles and the rotation axis. Credit: [31].

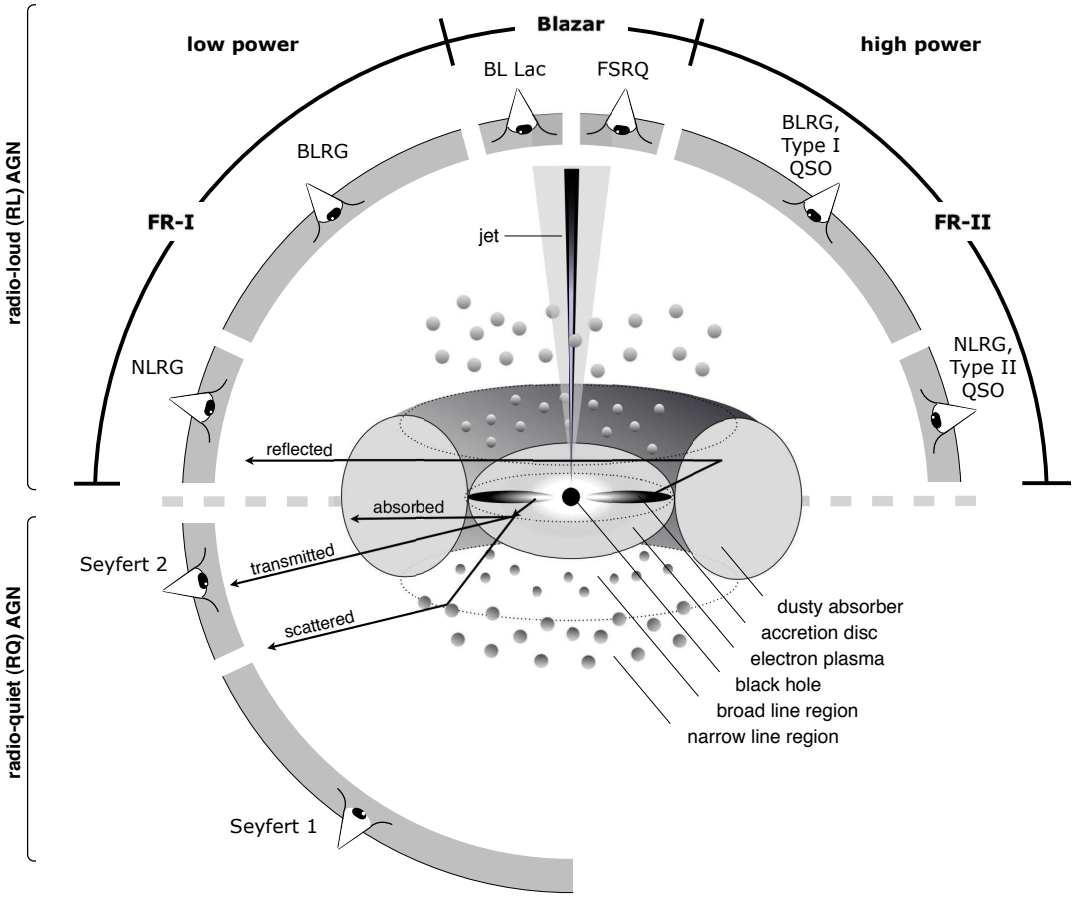

Figure 1.5: Illustration of an AGN and its classification. Categories depend on the presence of a jet, the visibility of the broad line region, the visibility of the jet beamed radiations and the power of the AGN. Abbreviations used: NLRG - Narrow Line Radio Galaxy; BLRG - Broad Line Radio Galaxy; QSO - Quasi Stellar object; FSRQ - Flat Spectrum Radio Quasar. Credit: [32].

fluxes which cannot be observed. The core where the jets originate can be detected in the radio spectrum. In addition, the jets end into so-called radio-lobes (emitting in the radio spectrum) created from the interaction between the jet plasma and the interstellar medium. The jet itself on the other hand generates a beamed emission covering a large fraction of the electromagnetic spectrum. The jets structure and underlying processes at the origin of this beamed emission will be covered in extended details in Chapter 2.

Many objects, gathered today under the AGN label, were originally given different names depending on the observation technique and wavelength at which they were detected. For instance, while VHE photons are absorbed by the EBL limiting the range of detection to redshift $z = 1$, radio surveys can detect sources up to redshift $z = 6$. Additionally, the source configuration (structure, orientation, etc.) is key and can lead to dramatically different observed spectra. As a consequence, more than 50 categories of AGN were created. A full review on the selection effects and AGN properties can be found in [33].

A unified picture of AGN was later introduced by Antonucci [34] and Urry & Padovani [35], reducing the classification to the following properties:

- presence of a jet;
- bolometric luminosity L_{bol};
- orientation of the central engine and/or jet with respect to the observer line of sight.

Figure 1.5 shows an illustration of an AGN and its classification according to these three criteria. The AGNs of interest in the context of LIV searches are grouped under the label of "blazar", namely AGNs comprising a jet which is oriented in the direction of the line of sight emitting highly variable TeV spectra. An extended discussion on blazars will be given in Chapter 2. Such objects occasionally undergo flaring episodes when their emission is heighten as compared to their continuous emission (quiescent state). Such episodes usually have a time scale ranging between a few minutes up to several hours.

In view of blazars being extra-galactic sources emitting potentially large fluxes of highly energetic photons, they appear as promising candidates for LIV studies when in flaring state. However, even though their location is fixed, there is no way to predict when a flaring episode will occur and become random events that are rather difficult to catch. This problem is partly answered by monitoring campaigns and alert systems established by gamma-ray astronomy experiments. As a consequence they appear as the best compromise between GRBs and pulsars.

1.5 LIV vs source intrinsic effects

Probing LIV by studying the time-of-flight of photons emitted by astrophysical sources relies on the crucial assumption that there is no correlation between photons energy and the times at which they are emitted. However, there is no absolute certainty on the sources emission mechanisms and nothing guarantees the simultaneity of emission for photons with different energies. Quite on the contrary, there is now rising evidence that source physical processes can induce energy-dependent time delays between photons at the moment of emission. These

intrinsic time delays will be added to LIV-induced ones leading to a total measured time delay decomposing as follows:

$$\Delta t_{n(\text{total})} = \Delta t_{n(\text{LIV})} + \Delta t_{n(\text{source})}(z+1) \tag{1.14}$$

or equivalently

$$\Delta \tau_{n(\text{total})} = \Delta \tau_{n(\text{LIV})} + \Delta \tau_{n(\text{source})}(z+1). \tag{1.15}$$

The LIV term incorporates a correction for the cosmological effects induced by the source distance or redshift. While LIV-induced time delays are a consequence of a propagation effect which cumulates with the distance travelled by the test particles, intrinsic time delays are generated at the source and stay constant whichever distance the test particles travel (see Figure 1.6).

As a matter of fact, the presence of energy-dependent time delays in GRBs was investigated by Norris & Bonnell, and is now a well-established fact. Although no significant time delay was found in short GRB data [36], they found a correlation between intrinsic time delays and the luminosity in long GRB data [37] and extracted the following relationship

$$L_{53} \sim 1.3 \left(\frac{\tau}{0.01\text{s}} \right)^{-1.14} \tag{1.16}$$

where L_{53} is the luminosity in units of 10^{53} erg.s^{-1} and τ is the spectral lag. A recent survey by the *Fermi* collaboration leading to the second GRB catalog [38] further established this lag-luminosity correlation as can be seen in Figure 1.7. LIV-induced time delays could therefore be distinguished from intrinsic ones in long GRB data, while such distinction will be more difficult to make for short GRBs.

Regarding pulsars, no intrinsic delay at very high energies has been found so far. Nevertheless, they could easily be distinguished from LIV-induced ones thanks to the periodicity of the signal and the increasing rotational period. Any intrinsic time delay expressed in rotational phase - i.e. in terms of the phase $\phi = t/r_p$, with $r_p \equiv r_p(t)$ the time-dependent rotation period - will not vary as the pulsar slows down and yield $\Delta\phi_{(source)} = \text{cst}$.[9] In contrast, a LIV-induced time delay would increase with time, as a function of the rotational period variation $\Delta\phi_{n(LIV)} \equiv f(r_p)$ [39].

Lastly, intrinsic effects in AGNs appear as the least known and most difficult to distinguish from LIV ones. This is mostly due to the source complexity and its emission mechanisms being not well-enough constrained to efficiently extract and isolate intrinsic time delays from measured ones. In this work, we perform a deep study on time delays generated via blazar emission processes (leptonic model) in order to find a way to discriminate intrinsic from LIV-induced lags in AGN data. We explore two possible ways to achieve this goal:

- On the source side, by **modeling blazar emission mechanisms** and study the steered energy-dependent time delays. This approach will be discussed in Part II.
- On the data analysis side, by performing a **population study** combining the data from sources sitting at various distances in order to blur or even suppress noise-like intrinsic time delays. This approach will be discussed in Part III.

[9] Ephemerides (astronomical tables) are used to express the temporal emission in terms of rotational phase r_p ($t \longrightarrow \phi$). This transformation encodes the phase variation and corrects it, along with any intrinsic effect.

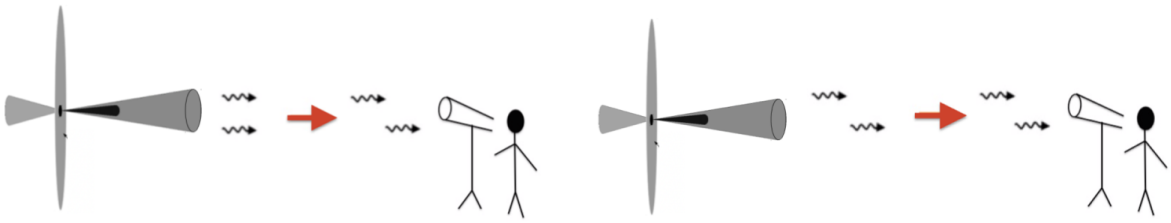

(a) LIV effect. (b) Intrinsic effect.

Figure 1.6: Illustration of the difference between LIV-induced and intrinsic effects. (a): Photons are emitted without time delay. LIV-induced delays appear and cumulate as photons travel large distances. (b): Intrinsic delays are generated at the emission and unchanged by the source distance. Photons arrive at the observer with the same delay as they had at the moment of emission.

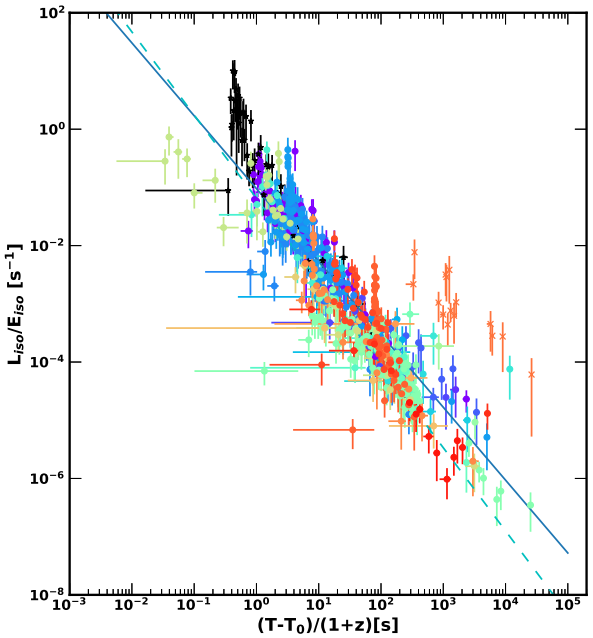

Figure 1.7: Lag-luminosity correlation established from a sample of 34 GRBs in the 10 MeV to 100 GeV range. Each color represents a separate GRB. The solid line shows a linear fit giving a decay of 1.25 ± 0.03, while the dashed line shows a decay of 10/7. Credit: [38].

Chapter 2

Blazars

Contents

Following the discussion on blazars given in Section 1.4.3, a more detailed presentation will now be provided. They were introduced as some of the most promising canditate sources for LIV time-of-flight studies: extra galactic sources undergoing flaring episodes lasting down to the minute scale and emitting a large spectrum of very high energy photons. The underlying processes at the origin of such emission will be reviewed in this chapter.

2.1 Characteristics

As mentionned in Section 1.4.3, AGNs are classified with respect to their *radio loudness*, partly defined by the presence or absence of well-developed radio jets. Blazars make up for a fraction of the radio loud AGNs which have their jets pointing very close to the observer line of sight, an approaching one and a receding one. As a consequence of this specific orientation, the detailed observation of blazars' jet can be difficult. Their interpretation partly rely on their counterpart radio loud AGNs, which jets are oriented farther from the line of sight (quasars, Seyferts and radio galaxies).

Radio-interferometry techniques, in particular very long baseline interferometry (VLBI), allowed to resolve and map the jets structure down to their launching region neighbouring the core black hole. They are believed to be a consequence of a spinning blackhole, ejecting a fraction of the accreted matter tightly collimated at its base by a powerful magnetic field. Observations indicate jets to be non uniform, featuring bright regions called "knots" moving within a dimmer and larger scale structure. Since AGNs detected at TeV energies mostly fall within the blazar category, the TeV emission is associated to the jet's relativistic beaming. Moreover the fast variability implies compact emission zones and tends to indicate the jet's knots are mainly responsible for the high energy emission. These knots, which are assumed to be highly dense and magnetised regions of the jet, appear to emit in various energy bands up to TeV, with a prominent flux in the X-ray energy domain. Both energy bands - radio and X-ray - show so to speak universal power law spectra indicating underlying non-thermal[1] processes.

2.1.1 Superluminal motion and relativistic beaming

Superluminal motion

From consecutive observation campaigns targeting specific blazars, it is possible to track and monitor the evolution of knots within a jet. Over the course of several months or a few years, one can witness the birth and disappearance of one or several knots, travelling several kpc from the jet base (nuclear jet) to the lobes[2]. The knots usually appear to move in the nuclear jet with apparent superluminal velocity, which arise from relativstic and geometrical effects induced by the jet orientation as illustrated in Figure 2.1.

Consider an observer positionned such that its line of sight makes a small angle θ with respect to the jet orientation. Let a knot move along the direction θ at speed v and emit two photons at coordinates (t_1, d_1) and (t_2, d_2). Within the time window $\Delta t = t_2 - t_1$, the knot travels a distance $\Delta d = d_2 - d_1 = v\Delta t$ along the direction θ while the two photons travel along the line of sight.

[1] This widely used terminology can lead to confusion regarding the nature of the radiation which *is* thermal. In practice, it refers to a continuum emission which cannot be described by a black-body radiation.

[2] In practice, the knots can only be tracked with VLBI-interferometry over parsec scales when they are the brightest i.e. in the nuclear jet. The propagation over kpc or Mpc scales is then estimated with various physical models.

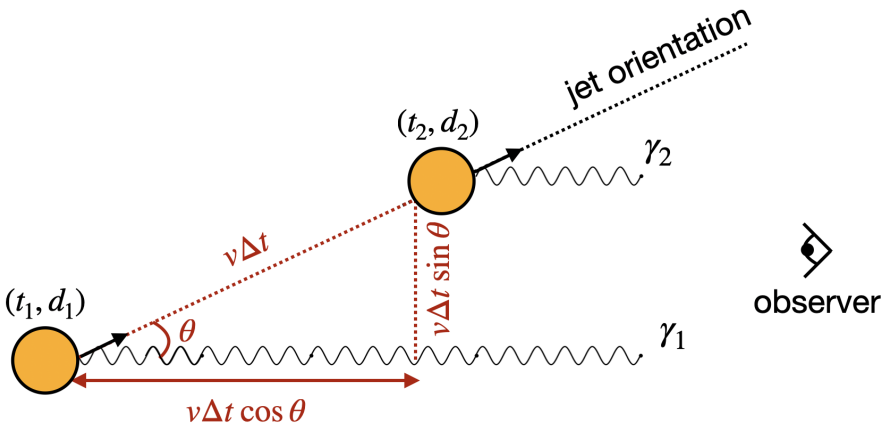

Figure 2.1: Illustration of the geometrical effect inducing apparent superluminal motion of knots (yellow sphere) in blazar jets.

The observer has only access to the projection of this displacement such that $\Delta d_{obs} = \Delta d \sin\theta$. As the knot moves towards the observer, the time difference Δt_{obs} does not reflect the true emission time difference Δt. From the path difference we have

$$\Delta t_{obs} = \frac{c\Delta t - v\Delta t \cos\theta}{c} = \Delta t(1 - \beta\cos\theta) < \Delta t \tag{2.1}$$

leading to the observed apparent velocity

$$v_{obs} = \frac{\Delta d_{obs}}{\Delta t_{obs}} = \frac{v\sin\theta}{1 - \beta\cos\theta} > v \tag{2.2}$$

The maximum apparent velocity is reached for $\cos\theta \equiv \beta$ in which case $v_{obs} \equiv \Gamma v$ with $\Gamma = (1 - \beta)^{-1/2}$ the associated Lorentz boost. The knots superluminal velocity provide strong evidence of their relativistic motion within the jet.

Relativistic beaming

Although radio loud AGNs feature two opposite relativistic jets, blazars display highly anisotropic patterns and are usually observed with only one visible jet (the one approaching) as a consequence of their specific orientation. A relativistic beaming (or Doppler boosting) is applied to the jet emission as a consequence of special relativity effects, i.e. from the time dilation and spatial compression induced by Lorentz transformation. When observed at small angle θ, the emission coming from an object moving at a relativistic speed $v = \beta c$ with corresponding Lorentz boost $\Gamma = (1 - \beta)^{-1/2}$ is affected by the Doppler factor that reads

$$\delta = \frac{1}{\Gamma(1 - \beta\cos\theta)}. \tag{2.3}$$

It results in alterations where the observed time scales are reduced while the observed frequencies are amplified:

$$t_{obs} = \frac{t}{\delta} \quad \Longleftrightarrow \quad \nu_{obs} = \delta\nu \quad \Longleftrightarrow \quad E_{obs} = \delta E. \tag{2.4}$$

This alteration has a direct influence on the observed flux. Starting from the specific intensity $I(\nu)/\nu^3$ being a Lorentz invariant, the observed emission intensity is transformed as follows:

$$I_{obs}(\nu_{obs}) = I\left(\frac{\nu_{obs}}{\nu}\right)^3 = \delta^3 I(\nu). \tag{2.5}$$

The corresponding total intensity is then given by

$$I_{obs} = \int_0^\infty I_{obs}(\nu_{obs}) d\nu_{obs} = \int_0^\infty \delta^3 I(\nu)\delta d\nu = \delta^4 I(\nu). \tag{2.6}$$

The emitted flux is linked to the radiated intensity through the following relationship:

$$F = \int_0^\infty I(\nu) d\nu, \tag{2.7}$$

and the observed flux writes

$$F_{obs} = \delta^4 F. \tag{2.8}$$

The jet emission is therefore highly amplified and tends to overshadow almost entirely the galaxy emission. In contrast, the receding jet is heavily dimmed and does not appear as visible to the observer.

To summarise, the jet emission undergoes a relativistic beaming which amplifies the observed photon flux, photon energy and source variability. This tends to greatly benefit LIV time of flight studies (see Section 1.4) and explains the particular interest for blazars rather than other types of AGNs.

2.1.2 Blazar emission

Since the relativistic beaming makes the jet emission so prominent, the typical blazar emission is generally attributed to processes happening within the jet, and more specifically within the knots. Although the temporal distribution of photons (or light curve) is variable and specific to each blazar, the spectral distribution tends to follow a characteristic pattern. Blazar energy distributions span over more than 15 decades in energy, from radio to TeV gamma-rays, and can entirely be described with only broken power laws. The corresponding spectral energy distributions (SEDs), which are simply another way to present energy distributions, are characterised by a two-bump structure.

The low energy bump, usually spanning between radio and X-ray energies, is attributed to a synchrotron emission as charged particles move through the knot magnetic field. Since protons are deemed inefficient at synchrotron processes due to their larger mass, the most plausible source of synchrotron light is found in light leptons (i.e. electrons and positrons). Knots are therefore believed to be filled with a hot, dense and relativistic plasma of either leptons only, or a mixture of leptons and protons.

The high energy bump on the other hand stretches up to TeV energies. Contrary to the low energy emission, there is yet to be a consensus on the physical processes at the origin of the high energy emission. The most common view involves inverse Compton scatterings where plasma leptons transfer part of their energy to soft (IR to X-ray) photons and accelerate them to gamma-ray energies. The dominant photon fields for such scattering are two folds:

- the synchrotron field produced by the plasma leptons in the knot. As leptons are believed to scatter on the very synchrotron photons they generated, this process is called synchrotron self-Compton (SSC).

- photon fields external to the jet. They can be generated by the blazar structure itself including most notably the accretion disc thermal emission, the optical/UV BLR emission or IR emission from the torus. They can also be external to the blazar's central engine and come from its environment such as the EBL or the CMB. This type of process is therefore labeled as external inverse Compton (EIC).

Other photon fields can contribute to both EIC processes and the overall blazar emission. In particular significant contributions to the radio and optical components are brought by the large scale jet and the host galaxy respectively.

2.1.3 Blazar sequence: BL Lac vs. FSRQ

From a statistical study based on a large selection of blazars (126 in total), Fossati et al. [40] found out the observed radio luminosity and the synchrotron (low energy bump) peak within blazars SED are anti-correlated. This study brought to existence the "blazar sequence" shown in Figure 2.2 (right) which unified the two classes of blazars: from bright and low frequency flat spectrum radio quasar (FSRQ) to dim and high frequency BL Lacertae (BL Lac). A more detailed classification of the blazar sequence is defined with respect to the synchrotron peak frequency $\nu_{peak,s}$:

- **FSRQ** with $\nu_{peak,s} \sim 10^{12} - 10^{13}$ Hz;
- **LBL** (low frequency BL Lac) with $\nu_{peak,s} \sim 10^{13} - 10^{14}$ Hz;
- **IBL** (intermediate frequency BL Lac) with $\nu_{peak,s} \sim 10^{15} - 10^{16}$ Hz;
- **HBL** (high frequency BL Lac) with $\nu_{peak,s} \sim 10^{17} - 10^{18}$ Hz.

Later on, Ghisellini et al. [41] performed a revision of this sequence with a total of 747 blazars, also shown in Figure 2.2 (left). In this re-edition, the gamma-ray luminosity is preferred to the radio one for the classification. This choice is motivated by current understanding of physical processes at the origin of the high energy emission. Although there is no general consensus, it is commonly believed the especially large flux observed in FSRQs at high energy is caused by the presence of important external photons fields. They thus introduce a significant inverse Compton emission which boosts the SED high energy bump. Alternatively, SSC processes are usually enough to model BL Lacs emission and make up for a standard picture.

Either way, although HBLs emit the most energetic photons and are therefore the most interesting types of blazar for LIV studies, they tend to be observed at the low redshifts due to their lower luminosity. Other types of blazars are therefore still considered as strong candidates as they offer an acceptable compromise between energy and distance.

2.2 Physical processes in relativistic jets

This section will be dedicated to the blazars emission mechanisms, focusing on one of the most commonly accepted scenario. As discussed above blazars SED are dominated by two non-

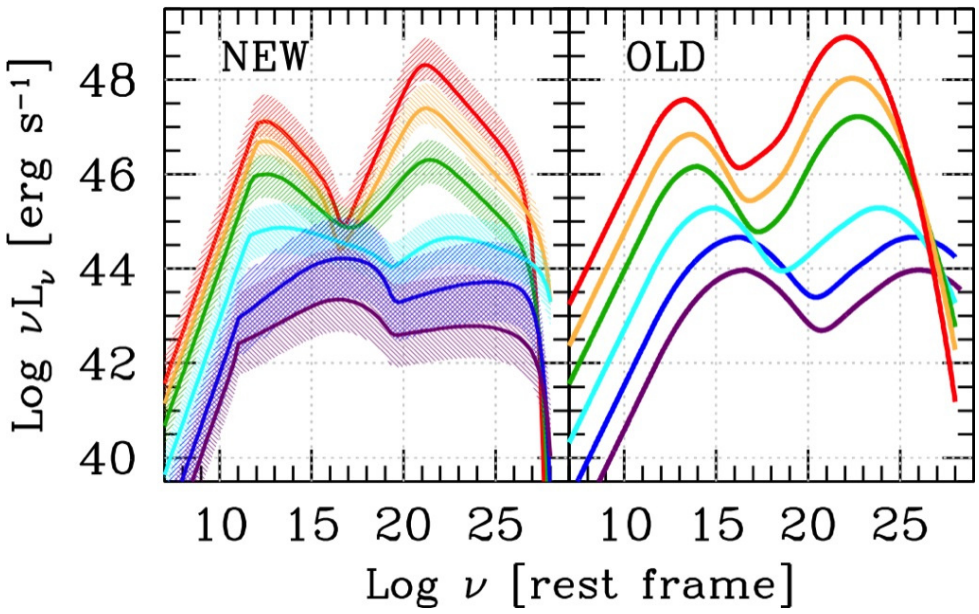

Figure 2.2: Sequences of blazar SEDs. The original sequence (right) provides a classification based on the radio luminosity (low energy synchrotron bump) while the revised version (left) is based on the gamma-ray luminosity (high energy inverse Compton bump). Credit: [41].

thermal components, the low energy one being attributed to synchrotron processes while the high energy one is believed to arise from inverse Compton processes involving leptons found in the knot plasma. Either way, the two components can only be explained when particles are found to be highly energetic, which indicates the presence of efficient and powerful acceleration mechanisms. Only the leptonic processes will be discussed in this work, providing with a brief overview and essential concepts and formulae that will be used later on. We invite the reader to refer to [42, 43] for a broader and more detailed review of current knowledge on blazar emission mechanisms (including hadronic and lepto-hadronic models).

2.2.1 Acceleration

Extragalactic jets usually extend over tens or hundreds of kpc, up to a few Mpc[3] for the most powerful AGNs, as indicated by their non-thermal emission. This implies the relativistic particles must undergo acceleration processes within the jet and be injected locally if they are to continuously cool down over such distances. We briefly present here three acceleration mechanisms often invoked to explain in-jet processes. As we will not be referring to it in the rest of the manuscript, we choose to focus on the underlying ideas rather than to develop the full calculation which can easily be found in many publications (including the ones referenced here) or textbooks.

Second order Fermi acceleration: stochastic mechanism

Fermi proposed two mechanisms resulting in the acceleration of charged particles from their repeated reflection on a magnetic mirror [44], now viewed as the primary mechanisms by which

[3] 1 kpc $\sim 3 \times 10^{19}$ m. For comparison, galaxies have a typical diameter ranging from 1 to 100 kpc. Relativistic jets scale can therefore be several orders above their host galaxy size.

astroparticles gain non-thermal energies. One scenario describes how a charged particle can gain energy from its relativistic motion in the presence of a randomly moving magnetic mirror (non relativistic motion) as illustrated in Figure 2.3 (left). It can be shown with changes of reference frame that a reflection occurring as the mirror moves towards the particle (head-on "collision") will lead to a gain in energy for the particle. The particle will however lose energy as the reflection occurs while the mirror is receding (head-tail "collision"). Since the probability for a head-on collision is slightly larger than the head-tail one, the average variation of energy is non zero and particles will gain energy in second order of $\beta_m = v_m/c$:

$$< \frac{\Delta E}{E} > \propto \beta_m^2, \tag{2.9}$$

with v_m the magnetic mirrror velocity. In the knotted relativistic jet picture, the magnetic mirror is assimilated to the knot's magnetic field turbulences that accelerates the leptons and/or the protons in the knot plasma. It is however a slow acceleration process which requires "pre-accelerated" particles.

First order Fermi acceleration: shock mechanism

A second and more efficient scenario enables particle acceleration through shock waves. In this picture, the magnetic mirror is played by the inhomogeneities in the shocked (upstream) and inert (downstream) media as illustrated in Figure 2.3 (right). Once again, this process is better grasped with the help of changes of reference frame. Whether we are placing ourselves in the upstream or downstream reference frame (i.e. where the corresponding medium is at rest), the moving medium will have a head-on motion. A particle coming from the downstream (resp upstream) medium at rest and passing through the shock front will then see the upstream (resp. downstream) medium as a magnetic cloud coming towards it. From the second order Fermi mechanism, this head-on motion induces an energy gain for the particle. The diffusion effects provoked by the magnetic turbulences (inhomogeneities) in the medium decreases the probability of particle escape. Changing the reference to the rest frame of the upstream (resp downstream) medium, the particle is likely to be once again reflected on the other medium, which is also seen with a head-on motion. As a consequence, as long as the particle cannot escape the shock system, it will undergo multiple reflections. The critical difference with the second order mechanism is that all the collisions are now head-on. For each round-trip, the particle will gain an average energy

$$< \frac{\Delta E}{E} > \propto \frac{r-1}{r}\frac{v_{shock}}{c} \propto \frac{\Delta v}{c} \equiv \beta_{shock}, \tag{2.10}$$

with r the compression factor between the upstream and downstream media, $\Delta v = v_{up} - v_{down} > 0$ the relative velocity between the upstream and downstream media, and $v_{\rm shock} = \beta_{\rm shock} c$ the shock front velocity. In the knotted relativistic jet picture, the shock front is for instance assimilated to the transition between a knot and the large scale jet. Although this process also requires "pre-accelerated" particles, it provides faster acceleration than the second oder Fermi mechanism.

Magnetic reconnection

Other acceleration mechanisms can occur in astrophysical sources. The currently most common mechanism (aside Fermi ones) involves magnetic reconnection. It describes events where

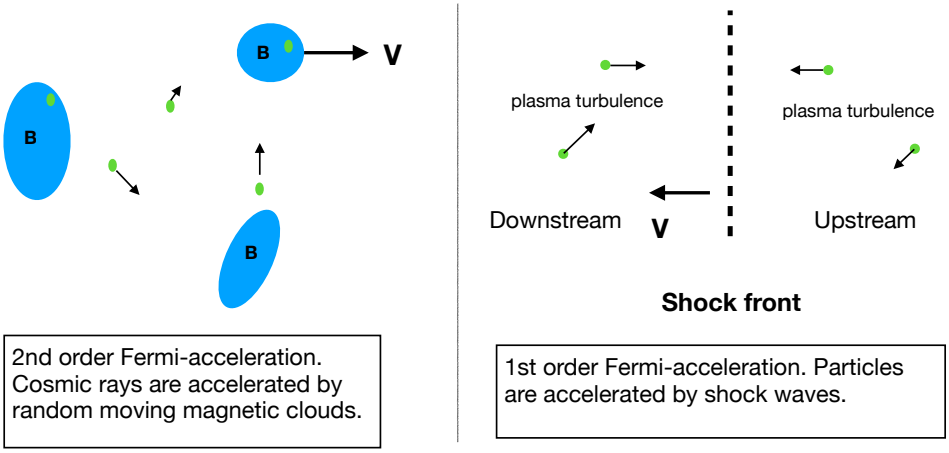

Figure 2.3: Illustration for the second (left) and first (right) order Fermi acceleration. Credit: [45].

magnetic lines can overlap and fuse, leading to a new magnetic topology. As they do so, the magnetic lines liberate magnetic energy which is converted and transferred to the surrounding plasma, enabling an efficient acceleration of particles. This phenomenon is invoked in AGNs where magnetic field lines are frozen in the highly conductive plasma (found for instance in the accretion disc) and thus governed by the plasma motion; or in pulsars to explain the energy dissipation, for instance via striped wind or wind nebulae [46].

2.2.2 Leptonic radiation processes

Leptonic models are able explain and represent blazar SEDs from the evolution of a single population of particles. Compared to hadrons, light leptons (electrons and positrons) care easier to accelerate with the above mechanisms. The two relevant interactions enabled by the system - synchrotron and inverse Compton processes - can then each fully explain one of the SED bumps.

2.2.2.1 Synchrotron

The accelerated leptons immediately start to radiate as they move through the magnetic field present in the jet and the knot. In the classical picture this radiation arises from the rather simple process called cyclotron, and occurs at a specific frequency given by

$$\nu_{cyclo} = \frac{qB}{mc}, \tag{2.11}$$

with q and m the charge and mass of the moving particle, and $B = ||\vec{B}||$ the magnetic field strength, and c the speed of light in vaccum. For relativistic motions, the process which is now called synchrotron yields a more complex frequency spectrum. We only provide the core expressions that will be needed later in the manuscript. Detailed mathematical derivations can be found in Rybicky & Lightman [47], Longair [48] or many other textbooks.

Assuming knots are spherical objects of radius R_k, the radiated multi-wavelength synchrotron spectrum can be obtained by solving the following transfer equation:

$$I_s(\nu) = \frac{j_s(\nu)}{k_s(\nu)}\left(1 - \frac{2}{\tau^2}[1 - e^{-\tau}(\tau - 1)]\right), \tag{2.12}$$

where $\tau = 2R_k k_s(\nu)$ is the optical depth. $j_s(\nu)$ and $k_s(\nu)$ are the synchrotron emission (or emissivity) and self-absorption coefficients.

Both coefficients are expressed in terms of the emitted power P. In the specific case of ultra-relativistic leptons or protons ($\beta \sim 1$) with Lorentz factor $\gamma = E/mc^2$, the emitted power per unit frequency ν for each particle is given by

$$P(\gamma, \psi, \nu) = \frac{\sqrt{3} q^3 B \sin\psi}{mc^2} \cdot \left(\frac{\nu}{\nu_c}\right) \int_{\nu/\nu_c}^{\infty} dx\, K_{5/3}(x), \tag{2.13}$$

where $\nu_c = \frac{3}{4\pi}\frac{\gamma^2 qB\sin\psi}{mc}$, and ψ is the pitch angle i.e. the angle between the magnetic field lines and the particle trajectory ($\vec{v}\cdot\vec{B} = \cos\psi$). $K_{5/3}(x)$ is a modified Bessel function of the second kind of order 5/3, i.e. solution of the Bessel differential equation that have a singularity at the origin ($x = 0$). In the specific case of leptons with isotropically distributed velocities and pitch angles, the averaged emitted power per lepton is given by

$$P_s(\gamma) = \frac{4}{3} c\beta^2\gamma^2\sigma_T U_B, \tag{2.14}$$

with $U_B = \frac{B^2}{8\pi}$ the magnetic energy density, $\sigma_T = \frac{8\pi r_e^2}{3}$ the Thomson cross section, and $r_e = \frac{e^2}{m_e c^2}$ the classical electron radius.

In the knot frame, the emission and auto-absorption coefficient for a distribution of particles $N(\gamma)$ and an isotropic distribution of pitch angle ψ write:

$$j_s(\nu) = \frac{1}{8\pi}\int_0^{2\pi} \sin\psi\, d\psi \int_{\gamma_{\min}}^{\gamma_{\max}} d\gamma\, N(\gamma) P(\gamma, \psi, \nu), \tag{2.15}$$

$$k_s(\nu) = -\frac{1}{16\pi m\nu^2}\int_0^{2\pi} \sin\psi\, d\psi \int_{\gamma_{\min}}^{\gamma_{\max}} d\gamma\, \gamma^2 \frac{d}{d\gamma}\left[\frac{N(\gamma)}{\gamma^2}\right] P(\gamma, \psi, \nu). \tag{2.16}$$

From the solution of Equation 2.12, one can derive the total emitted flux as seen in the knot's rest frame by integrating over the solid angle Ω:

$$F_s(\nu) = \int d\Omega\, I_s(\nu). \tag{2.17}$$

The observed flux can then be obtained following the transformation given in Equation 2.8 and reads

$$F_{s,obs}(\nu_{obs}, t) = \frac{\pi R_k^2}{d^2}(1+z)\delta^3 I_s(\nu), \tag{2.18}$$

where R_k is the emitting zone radius, $d = 2c(1 + z - \sqrt{(1+z)})/H_0$ is the luminosity distance with z the redshift, H_0 the Hubble constant and $\nu_{obs} = \nu \times (\delta/1+z)$.

2.2.2.2 Inverse Compton

The inverse Compton scattering (see Figure 2.4) is the interaction between a high energy (hard) lepton and a low energy (soft) photon, during which the lepton transfers part of its energy to the photon. The interaction therefore results in the boost of soft photons such that $E_{\gamma,f} > E_{\gamma,i}$. From energy and momentum conservation laws, it can be shown the photon energy in the lepton rest frame after the scattering $E'_{\gamma,f}$ is given by

$$E'_{\gamma,f} = \frac{E'_{\gamma,i}}{1 + \frac{E'_{\gamma,i}}{m_e c^2}(1 - \cos\theta')}, \tag{2.19}$$

with θ' the scattering angle in the lepton rest frame and $m_e c^2$ the electron rest mass. The corresponding energy in the laboratory frame is obtained from the following transformation:

$$E_{\gamma,f} = E'_{\gamma,f} \times \gamma(1 - \cos\theta'). \tag{2.20}$$

The probability of such an interaction is given by the Klein-Nishina cross section:

$$\sigma_{KN} = \sigma_T . \frac{3}{4}\left[\frac{1+\epsilon}{\epsilon^3}\left(\frac{2\epsilon(1+\epsilon)}{1+2\epsilon} - \log(1+2\epsilon)\right) + \frac{1}{2\epsilon}\log(1+2\epsilon) - \frac{1+3\epsilon}{(1+2\epsilon)^2}\right], \tag{2.21}$$

with $\epsilon = E'_{\gamma,i}/m_e c^2$ the reduced energy. In the limit of the Thomson regime where $\epsilon \ll 1$, the probability of such an interaction reduces to the Thomson cross section σ_T. Furthermore, the low energy regime leads to $E'_{\gamma,i} \simeq E'_{\gamma,f}$ such that the initial and final energies as seen by the observer obey the following relationship:

$$E_{\gamma,f} \propto \gamma^2 E_{\gamma,i}. \tag{2.22}$$

Such an energy gain is enough to accelerate soft photon to gamma-ray energies.

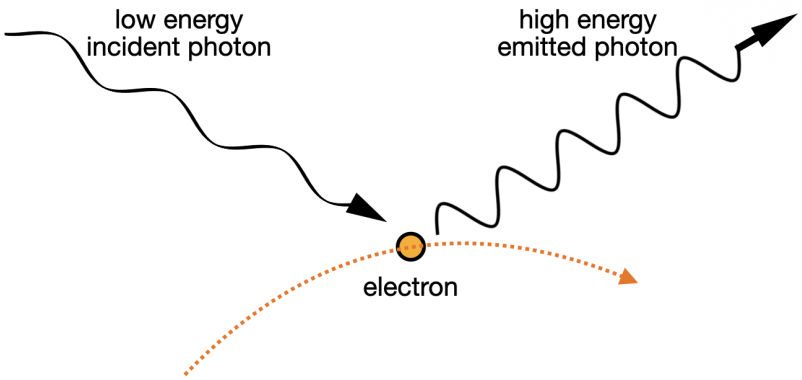

Figure 2.4: Schematic of an inverse Compton scattering between an incident low energy photon and an electron.

Conversely in the high energy regime - called Klein-Nishina regime - where $\epsilon \gg 1$, the cross section reduces to

$$\lim_{\epsilon\to\infty} \sigma_{KN} = \frac{3}{8}\frac{\sigma_T}{\epsilon}\left(\log 2\epsilon + \frac{1}{2}\right), \tag{2.23}$$

meaning the cross section decreases with the reduced energy as $\sigma_{KN} \sim \log(\epsilon)/\epsilon$. Furthermore, we get that $E'_{\gamma,f} \simeq m_e c^2$, that is to say the photon ends up transferring its excess energy to the electron[4], and the final photon energy seen by the observer is given by

$$E_{\gamma,f} \propto \gamma m_e c^2. \tag{2.24}$$

To summarise, while soft photons are boosted by a factor γ^2 and proportional to their initial energy, hard photons are boosted by a factor γ and proportional to the electron rest mass $m_e c^2$. In other words, the higher the energy of the incident photon, the smaller the probability it will interact through inverse Compton scattering and the lesser the boost it will receive.

The very high energy photon emission in blazars is therefore believed to be mainly generated through inverse Compton scatterings undergone by soft photon fields. In the case where this field is made up the synchrotron photons emitted by the leptons accelerated in the knot, the scattering process is referred as the synchrotron self-Compton (SSC) process. The inverse Compton spectrum can be described following a similar treatment to the one used for the synchrotron spectrum. The central difference resides in the expression of the inverse Compton emissivity coefficient. Considering a population of leptons $N(\gamma)$ and a photon field described by its initial density $n(\epsilon_0)$ at energy ϵ_0, the inverse Compton emissivity for SSC processes is given by

$$j_{IC}(\nu) = \frac{h}{4\pi}\epsilon q(\epsilon). \tag{2.25}$$

$q(\epsilon)$ is the differential photon production rate given by

$$q(\epsilon) = \int d\epsilon_0\, n(\epsilon_0) \int d\gamma\, N(\gamma) C(\gamma, \epsilon, \epsilon_0), \tag{2.26}$$

with $C(\gamma, \epsilon, \epsilon_0)$ a Compton kernel. Its expression was derived by Jones in [49]:

$$C(\gamma, \epsilon, \epsilon_0) = \frac{2\pi r_e^2 c}{\gamma^2 \epsilon_0}\left[2\kappa\log\kappa + (1+2\kappa)(1-\kappa) + \frac{(4\epsilon_0\gamma\kappa)^2}{2(1+4\epsilon_0\gamma\kappa)}(1-\kappa)\right], \tag{2.27}$$

where $\kappa = \frac{\epsilon}{4\epsilon_0\gamma(\gamma-\epsilon)}$. The reduced energy ϵ of the outgoing inverse Compton photon is bound in an allowed kinematic range determined by the photon initial energy ϵ_0 and the lepton Lorentz boost γ:

$$\epsilon_0 \leq \epsilon \leq \frac{4\epsilon_0\gamma}{1+4\epsilon_0\gamma}. \tag{2.28}$$

The lower bound indicates only energy transfers from leptons to photons are allowed, therefore forbidding conventional Compton scatterings. On the other hand, the upper bound indicates the scattered photon cannot gain more than the excess energy carried by the scattered lepton.

In contrast, the absorption by leptons of highly energetic scattered photons can be neglected such that $k_{IC}(\nu) \sim 1$. The inverse Compton photons boosted at energy E_γ may however interact

[4] We are no longer in an inverse Compton but a standard Compton process.

back with the knot's synchrotron field of energy $\epsilon \in [\epsilon_1, \epsilon_2]$ via pair production. The optical depth τ_{IC} associated to this phenomenon for an isotropically distributed synchrotron field is given by:

$$\tau_{IC}(\epsilon) = R_k \int_{\epsilon_1}^{\epsilon_2} d\epsilon \, n(\epsilon) \sigma_{\gamma\gamma}(E_\gamma, \epsilon), \tag{2.29}$$

with R_k the knot's radius and $\sigma_{\gamma\gamma}(E, \epsilon)$ the pair production cross section. Aharonian et al. [50] provided an approximated expression for that cross section which reads

$$\sigma_{\gamma\gamma}(s) = \frac{3\sigma_T}{2s^2}\left[\left(s + \frac{1}{2}\log s - \frac{1}{6} + \frac{1}{2s}\right)\log(\sqrt{s} + \sqrt{s-1}) - \left(s + \frac{4}{9} - \frac{1}{9s}\right)\sqrt{1 - \frac{1}{s}}\right], \tag{2.30}$$

with $s = \frac{E_\gamma \epsilon}{m_e^2 c^4}$. This process can be accounted for by introducing τ_{IC} in the radiated intensity, expressed similarly to that of Equation 2.12:

$$I_{IC}(\nu) = j_{IC}(\nu)\left(1 - \frac{2}{\tau_{IC}^2}[1 - e^{-\tau_{IC}}(\tau_{IC} - 1)]\right). \tag{2.31}$$

The observed emitted flux can then be obtained similarly to that of the synchrotron process, following the transformation given in Equation 2.18.

Finally, the power emitted by one lepton through inverse Compton processe can be obtained by integrating Equation 2.25. For an electron with Lorentz boost γ, the emitted power averaged over isotropically distributed velocities in the Thomson regime is given by

$$P_{IC}(\gamma) = \frac{4}{3}\sigma_T c \beta^2 \gamma^2 U_{ph}, \tag{2.32}$$

with U_{ph} the energy density associated to the photon field. In the SSC framework, U_{ph} is taken as the energy density associated to the *synchrotron* photon field. (see Equations 4.10).

2.2.2.3 External inverse Compton

Other than the synchrotron field, inverse Compton processes can occur in blazars from the interaction between leptons and a photon fields external to the jet or the AGN itself. The additional number of photons brought by external fields will contribute to generate very high energy photons and boost the flux in the SED inverse Compton bump. External photon fields can originate from

- **the accretion disc** radiating in the optical to UV spectrum;
- **the BLR** as it scatters the accretion disc radiation in the UV spectrum with a possible extension to X-rays;
- **the dust torus** radiating in the IR and radio spectrum;
- **the large scale jet** radiating in the radio spectrum from synchrotron processes possibly up to X-rays;
- **the host galaxy** mostly in the optical spectrum;
- **the EBL** mostly in the microwave to optical spectrum.

Although the large scale jet emission would take the form of a power law, external photon fields can generally be modeled with a blackbody emission centered on a specific temperature. A fraction of the external photons - those that are directed or reflected head-on towards the knot - should be blue-shifted in the knot's rest frame. As a consequence, the external photons can reach higher energies. In particular, photons emitted by the accretion disc or scattered by the BLR can reach keV energies (X-rays) and therefore be boosted up to TeV energies through inverse Compton interactions with the knot's leptons.

We give here the example for the accretion disc emission. We consider two frames of reference: the knot "k" and the accretion disc "ad". The derivation is very similar to that of the inverse Compton from the SSC process. The only difference lies within the photon field distribution $n(\epsilon_0)$ introduced in Equation 2.26, used to compute the emissivity and radiated intensity. Following Inoue and Takahara [51], we introduce the accretion disc photon field as a diluted blackbody centered at the external temperature T_{AD} which intensity in the disc frame writes

$$I_{EIC,ad} = \frac{\tau L_{AD}}{4\pi d^2} f_{\nu,ad}(T_{AD}). \tag{2.33}$$

τ is the optical depth for Thomson interaction, L_{AD} is the accretion disc luminosity, and d is the distance between the accretion disc and the knot. The blackbody spectrum can be expressed with the specific normalised Planck distribution that writes

$$f_{\nu,ad}(T_{AD}) = \frac{\pi}{\sigma_{SB} T_{AD}^4} \frac{2h\nu_{ad}^3}{c^2} \frac{1}{e^{h\nu_{ad}/k_B T_{AD}} - 1}, \tag{2.34}$$

with σ_{SB} the Stefan-Boltzman constant and k_B the Boltzman constant. The transformation to go from the disc to the knot frame is done by applying a Doppler boosting to the intensity:

$$I_{\nu,k}(\nu_k) = \frac{1}{4\pi} \int d\Omega_k \, \delta_k^3 I_{\nu,ad}(\nu_{ad}) = \Gamma_k \frac{\tau L_{AD}}{4\pi R^2} \, f_{\nu,ad}(T_{AD}), \tag{2.35}$$

with δ_k the knot's Doppler factor (see Equation 2.3) and Γ_k the knot's Lorentz boost in the disc frame. We applied the transformation $d\Omega_k = \delta_k^2 d\Omega_{ad}$, and made the assumption of an ultra-relativistic head-on collision leading to $\delta_k \sim 2\Gamma_k$. The observed emitted flux can then be obtained similarly to that of the SSC process, following the transformation given in Equation 2.18.

Chapter 3

Gamma-ray astronomy with imaging atmospheric Cherenkov telescopes

Contents

In this chapter we introduce gamma-ray astronomy and the detection principles, either direct with space observatory or indirect with ground astronomy through imaging atmospheric Cherenkov telescopes. We then present one of the leading IACT, the high energy stereoscopic system (H.E.S.S.) experiment, from its structure to the data acquisition and the analysis strategies. Finally, we give an overview of the future of ground-based gamma-ray astronomy with the Cherenkov telescope array (CTA).

3.1 VHE gamma-ray astronomy

Typically ranging from a few hundred keV to hundreds of TeV, gamma-rays are the most energetic form of light. Most photons are produced through thermal processes. The hotter the source, the higher the frequency of the radiated light. However, objects can hardly get hot enough to produce highly energetic gamma-rays[1] such that they are mostly generated through non-thermal mechanisms including:

- radioactive decay typically procuding $E_\gamma \sim$ MeV gamma-rays;
- electron-positron annihilation ($e^+ + e^- \longrightarrow \gamma + \gamma$) creating two photons of minimum energy $E_\gamma = 511$ keV in the annihilation rest frame;
- pion decay ($\pi^0 \longrightarrow \gamma + \gamma$) with an energy distribution peaking at $E_\gamma \sim 70$ MeV;
- synchrotron radiation producing gamma-rays with energies that depend on the energy of the charged particle moving in the magnetic field, and the magnetic field strength (c.f. Section 2.2.2.1);
- inverse Compton scattering producing gamma-rays which energies depend on the initial photon and lepton energies (c.f. Section 2.2.2.2);
- *bremsstrahlung* radiation by decelerating charged particles which produce gamma-rays with energies that depend on the degree of deceleration.

Gamma-ray astronomy focuses on the most energetic photons with the goal to uncover the nature of objects, and phenomena at their origin. As they propagate through the cosmos, these gamma-rays may interact with non relativistic matter via three interaction channels:

- photoelectric effect (ionisation of an atom) - dominant up to $E_\gamma \sim 50$ keV;
- Compton scattering ($\gamma + e^- \longrightarrow e^- + \gamma$) - dominant in the range $E_\gamma \sim 0.1 - 5$ MeV;
- pair production ($\gamma + \gamma \longrightarrow e^- + e^+$) - dominant above $E_\gamma \sim 5$ MeV.

The fraction of emitted gamma-rays that survived their trip en route to Earth are later massively screened by the Earth atmosphere. As a consequence, direct gamma-ray detection with ground-based instruments is impossible. There are two ways to work around this issue: either bypass the atmosphere with space-based direct detection, or ground-based indirect detection with by-products of gamma-ray interactions with the atmosphere.

[1] From Wien's law: 0.2898 (cm K) $= \lambda_{\max} T$. The most brilliant objects known today (e.g. 3C273 quasar) reach $\sim 10^{13}$ K corresponding to 23 GeV. For comparison, the Sun's core temperature $T_{\text{sun}} = 15 \times 10^6$ K corresponds to ~ 10 keV.

3.1.1 Direct detection: satellite-embarked instruments

Typical setup

Direct detection while bypassing the atmosphere requires to send a detector in space, embarked on board a satellite. Due to financial and technical reasons, the weight and size of such detectors is greatly limited by rocket standards, with typical scales of ~ 1 m^3 and a few hundred kilograms. The detectors' collection area and internal structure are therefore limited in size and weight, greatly restricting their potential. However, the field of view (FoV) of such instruments is generally very large (typically a few steradians[2]) such that a large fraction of the sky can be monitored at each orbit.

The gamma–ray flux emerging from the ensemble of astrophysical gamma-ray sources is characterised by a decreasing power law energy spectrum. As a consequence, this flux gets dimmer as photon energy increases. Therefore, a collection area close to 1 m^2 in size has a very small probability to catch photons with energy exceeding a few hundreds GeV.

The detection principle is a destructive one where gamma-rays go through a limited number of heavy material layers in order to provoke interactions, and die out by depositing all or part of their energy in the detector. The penetration depth - distance at which the photon starts to interact with the medium - increases with photon energy such that very energetic gamma-rays can cross the detector through and through, and go undetected. This major limitation inherent to gamma-ray space-telescopes defines a differenciation between high energy (HE) and very high energy (VHE) photons. Direct detections are limited to the detection of HE photons only.

Leading satellite-based experiments

***Fermi*-LAT: Large Area Telescope** One of two instruments mounted on the low orbit (~ 550 km altitude) *Fermi* Gamma-ray space telescope launched in 2008 [52]. *Fermi*-LAT has a 0.8 m^2 collection area along a 2 sr FoV, and it is sensitive between 20 MeV and 300 GeV. This experiment is mainly managed by US, italian, french and japanese institutions.

***Swift*-BAT: Burst Alert Telescope** One of the three instruments mounted on the Neil Gehrels Swift observatory [53], launched in 2004 and orbiting at ~ 550 km altitude. *Swift*-BAT has a 1.4 sr FoV, for a sensitivity on energy ranging between 15 and 150 keV. This experiment is essential as it triggers an alert to other experiments when it detects a burst. It is mainly managed by US, UK and italian institutions.

3.1.2 Indirect detection: ground-based imaging atmospheric Cherenkov telescopes

The composition of Earth's atmosphere allows for different levels of penetration provided particles nature and characteristics. Photons being no exception, the level of penetration depends on their frequency, and in particular TeV gamma-rays rarely reach below 10 km altitude.

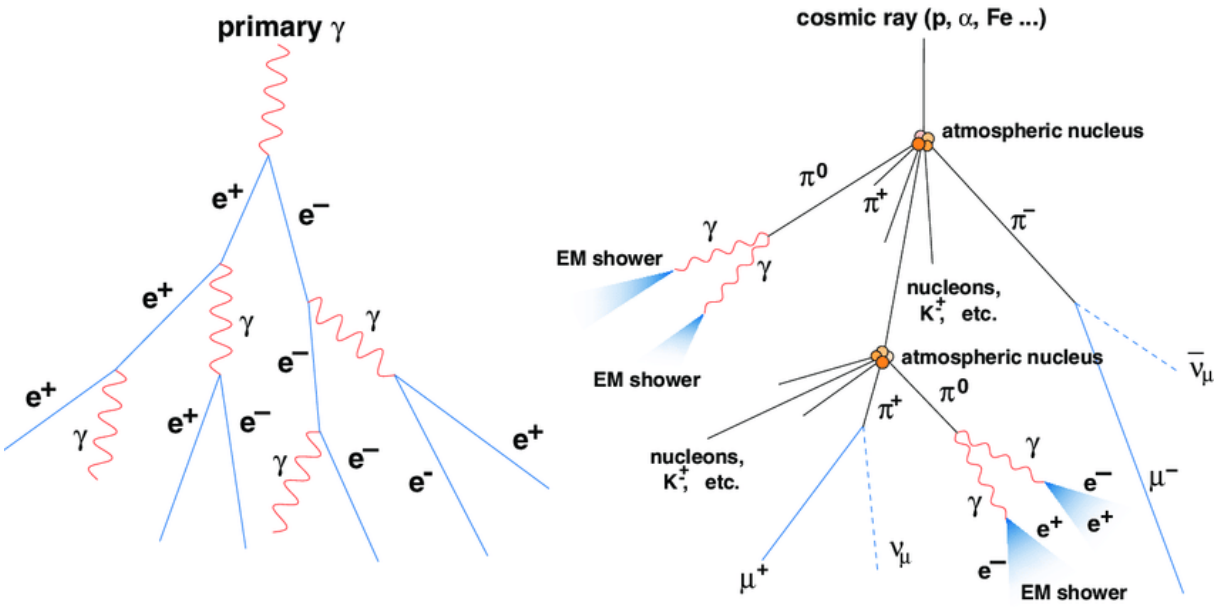

Figure 3.1: Schematic view of an electromagnetic (left) and hadronic (right) extensive air shower. Credit: [54].

3.1.2.1 Extensive air showers

A VHE gamma-ray penetrating the upper atmosphere will inevitably interact with air molecules via pair creation. The secondary electron and positron undergo *bremsstrahlung* emission resulting in new gamma-rays of smaller energy, which in turn will interact via pair creation. In a dense medium like the atmosphere, the process repeats itself countless times resulting in a shower made up of sometimes billions of particles as shown in Figure 3.1 (left). When secondary photons fall below a critical energy $E_{crit} \sim 85$ MeV, ionisation losses become more important than *bremsstrahlung* emission. As a result, the process is stopped and particles end up being absorbed by the medium. The atmosphere behaves as a natural inhomogeneous calorimeter from which gamma-rays can hardly escape. This process is called *extensive air shower*. In the case of incoming photons or leptons, we talk about electromagnetic air showers.

Similarly, there exists hadronic air showers which are started by heavier particles such as protons (e.g. cosmic rays) or more complex nuclei. The process is started by the splitting of nuclei resulting in the production of hadrons, excited nuclei, kaons and pions. Charged pions interact with the atmosphere resulting in muonic leptons[3], while neutral pions decay into two gamma-rays which dissipate their energy into electromagnetic showers as shown in Figure 3.1 (right). The process stops when charged pions reach a critical energy leading to their decay into muons, and when gamma-rays reach the pair-creation threshold. The overall development and decay of hadronic showers is more complex than electromagnetic ones, leading to a more asymmetrical and wide-spread shower profile.

[2] 1 sr = 3283 deg^2

[3] $(\pi^+ \longrightarrow \mu^+ + \nu_\mu)$ and $(\pi^- \longrightarrow \mu^- + \bar{\nu}_\mu)$

3.1.2.2 Cherenkov radiation

Whether it is an electromagnetic or hadronic air shower, highly energetic particles such as gamma-rays result in secondary charged particles travelling at velocities close to the classical in-vacuo speed of light c, often taking over the speed of light in the medium such that $v > c/n$, with n is the refractive index of said medium. As they move through the medium these charged particles induce a pertubation in the electron shells of each atom they encounter. Electrons move away from their initial position as they get polarised, then fall back to their ground state as the charged particle moves away. De-excitation gives rise to a radiation prominent at small wavelengths - blue to UV light in the visible spectrum - which fades away as successive waves combine in destructive interferences. At velocities $v > c/n$, successive waves start to interfere in a constructive way and end up in phase at the surface of a cone producing a visible effect that is called *Cherenkov radiation*.

From simple trigonometry, the characteristic cone angle θ - called *Cherenkov angle* - can be expressed as a function of the charged particle velocity v:

$$\cos\theta = \frac{c}{vn}. \tag{3.1}$$

Since both the refractive index n for air and the low-energy speed of light in vacuum c are known, measuring the Cherenkov angle gives direct access to the charged particles velocity v. Furthermore, the particle continuously slows down as it travels through the medium. When its velocity falls below the speed of light in the medium c/n, the Cherenkov emission stops.

3.1.2.3 Imaging atmospheric Cherenkov telescopes

Detection principle

Air showers are characterised by what is called the shower maximum - altitude at which the number of particles in the shower is maximal - typically located at ~ 10 km. At such altitude, the refractive index of air is $n_{max} = 1 + \epsilon$ with $\epsilon \sim 10^{-4}$. Starting from the Cherenkov inequality $v > c/n$, we can derive the minimum energy (threshold) needed by a particle to start a Cherenkov radiation: $E_{th} > m/2\epsilon$. For electrons or positrons, this energy threshold is ~ 35 MeV which is below the critical energy $E_{\text{crit}} = 85$ MeV that stops the shower. In other words, the particles in air showers continuously emit Cherenkov radiation such that the pool of light projected on the ground is not a ring but a full disc. Furthermore, from Equation 3.1 we find the Cherenkov angle can be expressed as $\theta \sim \sqrt{2\epsilon} \sim 0.8°$ such that the disc has a typical radius of ~ 120 m. An illustration of this layout can be found in Figure 3.2.

Indirect detection takes advantage of EAS by sampling this projected Cherenkov light using imaging atmospheric Cherenkov telescopes (IACTs) allowing for reconstruction of the primary particles main properties including nature, energy, time of incidence or direction. The light pool properties impose the location, disposition, size and optical techniques used for such telescopes. However, even if showers start to develop for gamma-rays with energy above $E_{\text{crit}} = 85$ MeV, the Cherenkov signal is too weak to be detected by this method and a much higher threshold is required, typically about tens of GeV. This limitation defines yet another but similar differenciation between high energy (HE) and very high energy (VHE) photons. IACTs are limited to

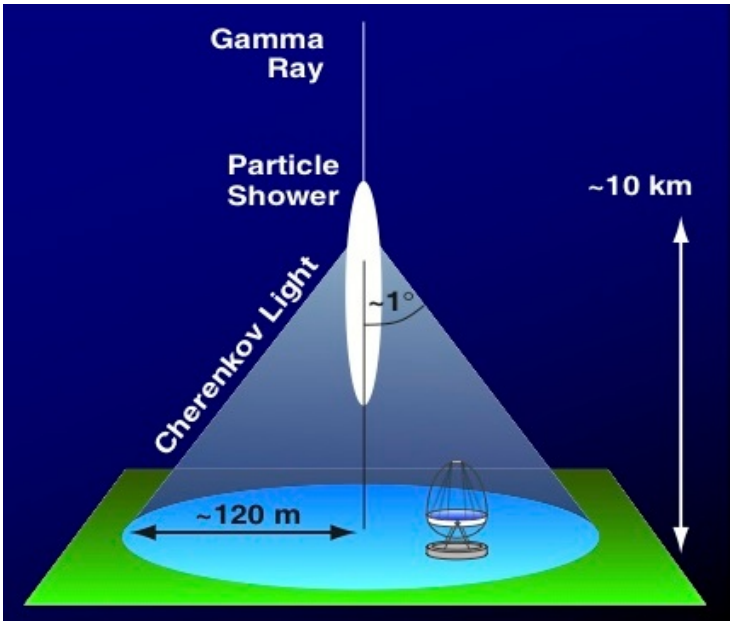

Figure 3.2: Popular illustration of the layout for indirect detection in gamma-ray astronomy. Extensive air showers form at ~ 10 km above the ground level, resulting in a cone of Cherenkov light illuminating the ground over a circular area of radius ~ 120 m. An imaging atmospheric Cherenkov telescope located in the pool of light records the shower profile.

the detection of VHE photons only.

Typical setup

A typical IACT will consist of a large dish made up of multiple segmented mirrors installed on a mount controlling the pointing direction. The mirrors add up to form detection areas of hundreds of m^2 and allow photon detection down to tens of GeV and up to tens of TeV. They are used to reflect the Cherenkov light onto a camera to record the EAS image patterns. Given each primary particle generates a very fast (a few nanoseconds) and very faint flash of Cherenkov light, IACT cameras are usually made up of photomultipliers (PMT) coupled with fast electronics in order to resolve nanoesecond events and amplify the originally faint signal.[4]

Such a detection technique therefore imposes observations to be made at night in the absence of strong moonlight, greatly limiting the observational times and duty cycles of IACTs, as opposed to satellite-embarked instruments. Furthermore, it imposes small field of views typically reaching a few degrees generally preventing the simultaneous monitoring of multiple sources.

IACTs are usually built on high altitude grounds (1 to 3 km high) in order to get closer to the EAS maximum and therefore detect larger (in the sense of less diluted) fluxes. Moreover, such location brings the telescope above the level of certain types of clouds and reduces the chances of absorption or scattering of Cherenkov photons. IACTs should however not be placed higher than 3 km as mirrors would then be in the reach of shower particles and suffer heavy damages.

[4] A classic CCD camera could not be used as their typical time resolution of microsecond and typical sensitivity could not resolve such events.

Such altitude further reduces the number of detectable showers as the light pool becomes smaller.

Leading IACT experiments

MAGIC: ***Major Atmospheric Gamma-ray Imaging Cherenkov telescopes*** System of two 17 m-dish IACTs built in 2004 at La Palma in the Canary Islands (Spain) at 2200 m altitude [55]. From the 236 m^2 detection area and 3.5 degrees FoV, MAGIC is sensitive between 25 GeV and 30 TeV. This experiment is mainly managed by spanish, italian and german institutions.

VERITAS: ***Very Energetic Radiation Imaging Telescope Array System*** System of four 12 m-dish IACTs operating since 2007 from Arizona, USA at 1268 m altitude [56]. VERITAS has a 260 m^2 detection area and 3.5 degrees FoV with a sensitivity between 100 GeV and 50 TeV. It is maintained by US institutions.

H.E.S.S.: ***High Energy Stereoscopic System*** An extensive description of this experiment is provided in the next section.

3.2 H.E.S.S.: the high energy stereoscopic system

3.2.1 Overview of the H.E.S.S. array

The H.E.S.S. array, shown in Figure 3.3, consists of five telescopes located at 1800 m altitude in the Khomas highlands region in Namibia. As such, it is the only IACT currently in operation in the southern hemisphere making it especially suited for the study of galactic sources and the galactic center. The namibian overall dry and clear climate along with its excellent atmospheric quality and absence of light pollution is furthermore particularly favourable for ground-based astronomy.

H.E.S.S started operations in 2003 with four identical 13 m-dish telescopes - CT1-4 for the first phase HESS-I (CT stands for Cherenkov Telescope) [57]. They are arranged in a square, each separated from the neighbouring one by 120 m to optimise the sensitivity at low energies, leading to a detection range between 100 GeV and 10 TeV. The fifth very large 28 m-dish telescope - CT5 for the second phase HESS-II - now sitting at the center of the square, was built and commissioned nearly ten years later, in 2012 [58]. Its much larger mirror enables detection at lower energies[5], the array now reaching a sensitivity down to 30 GeV. The four small telescopes operate in stereo-vision only, while CT5 can operate either in monoscopic mode (by itself) or stereoscopic mode with the other telescopes.

3.2.2 Structure and optical system

The five H.E.S.S. telescopes are single dishes installed on alt-azimuthal steel mounts. The small telescopes are equipped with 380 spherical mirrors of 60 cm diameter, adding up to a 13 m diameter for an effective reflective surface of 107 m^2. The mirrors are arranged following a Davies-Cotton design, i.e. they are positionned along a spherical surface which focal length

[5]The lower the primary particle's energy, the fainter the flux of Cherenkov light. A larger detection area enables to collect more Cherenkov photons and yield higher flux that is in excess against the background light.

Figure 3.3: The H.E.S.S. array. Credit: H.E.S.S. collaboration.

corresponds to exactly half that of the mirrors ($f = 15$ m).

A parabolic design was preferred for CT5. Indeed, the Davies-Cotton design induces a temporal dispersion of the Cherenkov photons that increases with the dish diameter. On the very large telescope, such a design would lead to a significant dilution of the signal and thus greatly deteriorate the signal to noise ratio. With a paraboloid design, the arrival time of Cherenkov photons in the focal plane is isochronous. On the down side, this design tends to foster optical aberration which requires to perform observations on a limited field of view. The large telescope is equipped with 876 hexagonal mirrors of 90 cm diameter, for a total reflective dish of 28 m and an effective area of 614 m^2.

Camera

Each small telescope is supplied with a camera made of an octogonal network of 960 PMTs (pixels), arranged in 60 units (drawers) of 16 pixels. Each PMT is equipped with a Winston cone to guide and focus Cherenkov photons on the photocathode, and consequently reduce the loss of signal between PMTs. These cameras reach a total field of view of 5 degrees, enabling the observation of extended sources.

Up until october 2019, the large telescope was equipped with a bigger camera made of 2048 PMTs organised in 128 drawers of 16 pixels. It could therefore reach a much higher resolution on the shower images. Each PMT was again equipped with Winston cones, adding up to a total field of view of 3.2 degrees. It was recently replaced with a prototype camera *FlashCam* [59] designed for the future Cherenkov telescope array observatory CTA (more in Section 3.3). This new camera is equipped with 1758 PMTs arranged in hexagonal pattern, with 588 drawers of 12 pixels for a total field of view of 3.4 degrees.

3.2.3 Data acquisition

3.2.3.1 Trigger system

A typical observation night is divided in observation runs of 28 minutes during which the received signal is recorded following a trigger strategy. The trigger system has three levels of selection:

- **1st level:** cleared when an event triggers the internal system of each individual telescope with at least one pixel (PMT) having a collected charge exceeding a threshold of four photo-electrons (p.e.).
- **2nd level:** cleared when at least three pixels that exceeded the threshold are located within four neighbouring drawers (called a sector), and the signal occurs within a 1.3 ns window[6].
- **3rd level:** the signal correlation between each individual telescope is checked with a central trigger with three possible outcomes.
  - At least two telescopes triggered the event (passed the first two levels) within a window of 80 ns[7]: the event is recorded in stereo mode;
  - Only CT5 was triggered: the event is recorded in mono mode;
  - Only one HESS-I telescopes (CT1-4) was triggered: the event is discarded.

This trigger strategy helps to decrease the load on the data aquisition system (DAQ) and reduce dead time during event readout. With a typical trigger rate of ~ 1 kHz over the whole array, the average duration between two events is 1 ms such that the probability to record coincident noise events with multiple telescopes is low. The third level therefore greatly contributes to night sky background light (NSB) rejection in stereo mode.

3.2.3.2 Calibration

Before analysing the obtained data, a number of operations must be performed to convert and calibrate the signal.

- **Pedestal subtraction.** The pedestal refers to the PMT output signal in absence of light (i.e. noise). It is estimated with a pedestal run which is an observation run performed while the camera lid is closed using an external trigger. The pedestal is then subtracted to the signal.
- **Flat fielding.** A flat field run is an observation run where the camera pixels are homogeneously illuminated by light emitting diods (LEDs) mounted on the telescope dish. The response of each pixel is corrected such that the PMT array yields a flat signal.

[6] Duration needed to take into account the difference of emission time and travelled distance of associated photons.

[7] Duration needed to take into account the telescope separation (photons travel 400 m in 80 ns in optical fiber) and electronic lag time.

- **Single p.e. conversion.** It is estimated with a single p.e. run, an observation run where LEDs send pulsed light flashes to the camera pixels. The LEDs light intensity is adjusted for the photocathode of each PMT to emit on average one p.e. per flash. This is used to evaluate the conversion factor between ADC counts and p.e.

- **Pointing correction.** Its role is to take into account the structural deformation of the telescopes' mount and positionning errors. This correction is estimated with pointing runs, observations runs where the telescope points at a star with known position. The image reflected by the mirrors is compared to an image obtained with a CCD camera located at the back of the camera.

- **Optical efficiency.** Optical efficiency includes the transmittance of Cherenkov photons by the atmosphere (heavily dependent on meteorological conditions), the photon collection rate (geometric factor), the mirrors reflectivity, and the PMTs overall efficiency. This estimation is done with muonic events which do not trigger showers of their own but produce Cherenkov light by moving through the atmosphere and are seen by the cameras as a ring or an arc image. The images obtained through observation are compared to expected images generated with an analytical model.

3.2.4 Analysis

There are two independent analysis chains in H.E.S.S. - ParisAnalysis and H.E.S.S. analysis package (HAP) - which provide cross-checks for every published analysis, but also help identify and correct bugs in the softwares. Distinct algorithms were developped for each analysis chain: Model++ for ParisAnalysis [60], ImPACT for HAP [61], and the Hillas model [62] used by both analysis chains.

3.2.4.1 Event reconstruction

The event reconstruction is performed following the Hillas model. It is first preceded by a two-stage image cleaning used to remove a maximum of NSB signal: all the pixels with a charge lower than 5 p.e. are set to zero while pixels with a charge exceeding 10 p.e.[8] are directly stored. Pixels having a charge between 5 and 10 p.e. are stored only when the closest neighbouring pixels also possesses a charge exceeding 5 p.e. The images are then ready to be analysed.

- First, the **incident direction** of the primary particle is retrieved from the image orientation in the camera plane. The images are modeled with 2D ellispes parameterised following the Hillas parameters illlustrated in Figure 3.4:

  - length of the semi-major L and semi-minor W axes;
  - center of gravity of the shower image d;
  - total number of photons contained within the ellipse (total charge or amplitude of the shower image);
  - position of the ellipse with respect to the camera center;
  - distance from the center of gravity to the expected source position.

[8] This threshold is sometimes set to 7 p.e. when the signal is too faint.

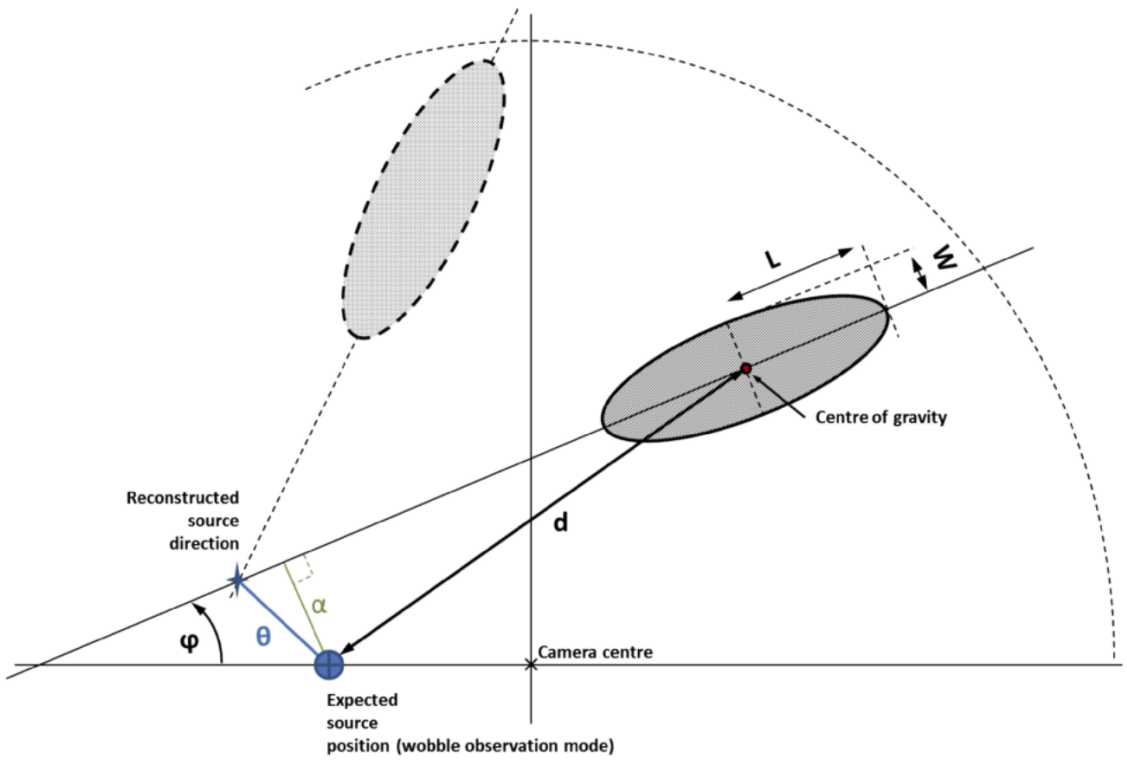

Figure 3.4: Illustration of the Hillas parameters. Credit: [63].

In mono mode, the incident direction is given by the vector along the 2D image ellipse major axis. The incident position is therefore degenerate. A 3D image of the events can be recovered from the different viewpoints offered by each telescope in the stereo mode. It provides a higher accuracy on the incident direction of the primary particle. Its incident position can then be precisely pin-pointed from the intersection of the major axes of each image.

- Then, the **type** of the primary particle is judged based on the air shower image shape and morphology. As EAS produced by hadronic primary particles are 10^5 times more frequent than that generated by gamma-rays, hadronic showers tend to interfere with observations and it is therefore crucial to efficiently discriminate them. While gamma-ray events generate rather elliptical and uniform shower images, the ones generated by hadrons are more irregular with in particular the presence of multiple islands due to the sub-cascades. The cosmic-ray background can be suppressed by applying a threshold (or cut value) on the spread of the photon angular distribution (L and W axes). The events with a spread wider than the threshold are classified as hadrons and are rejected. Therefore, only well-defined ellipses are kept in the analysis.

- Finally, the **energy** of the primary particle is estimated from the image total intensity. The flux of Cherenkov light is correlated to the number of charged particles in the EAS, and thus to the primary particle energy for a given distance and zenith angle.

The Model++ and ImPACT algorithms are improvements of the Hillas model aiming at providing a finer estimation of the primary particle properties. Model++ predicts the amount

of light collected by each pixel by comparing shower images detected by the camera and ones that are simulated with a semi-analytical model with a statistical fit. The use of the information provided by each individual pixel (rather than treating them as an ensemble) allows to avoid the image cleaning. It therefore yields a more precise fitting of the shower image along with a precise estimation of the NSB contribution in each pixel. The reconstructed energy and incoming direction are therefore more precise than with the Hillas model. The ImPACT model on the other hand is fully analytical which allows to include fine effects such as Earth magnetic field or biases in the electronics. The NSB is however less precisely estimated than in Model++. Moreover, both algorithms are able to predict the events type (either gamma-ray, hadron or muon) from either Goodness-of-fit method (Model++) or a boosted decision tree method (ImPACT).

3.2.4.2 Signal extraction

Due to the large number of hadron events, some are inevitably misidentified as gamma-rays and pass the selection cuts. The data thus shows a uniform background of events with a potential excess from the target photon source. In H.E.S.S., this background is estimated with ON and OFF regions. The ON region is believed to contain the signal originating from the target source along with a background contribution, while the OFF regions (control regions) contain only background signal. OFF regions are selected close to the ON region in order for all regions to have a comparable background contribution. The excess of signal is then given by

$$E = N_{ON} - \alpha N_{OFF}, \tag{3.2}$$

with N_{ON} and N_{OFF} the number of events from the ON and OFF regions, and α a scaling factor corresponding to the ratio of acceptance (c.f. Section 7.1.4.1) between the regions.

The main and most effective procedure to define OFF regions is the reflected background method [64]. In this method, ON and OFF regions are of the same size and are all defined with the same offset angle with respect to the camera center around the source position (see Figure 3.5). This strategy guarantees the ON and OFF regions to have the same acceptance. The scale factor α then simply becomes the inverse of the number of OFF regions, i.e. it can be determined without knowing the telescope acceptance. In order to limit systematic errors and work with a symmetric coverage around the source, the direction of the offset alternates between observation runs.

Two other notable strategies include the ring background model [64] which uses a ring of OFF regions around the source, and the template technique [65] where a background model is fitted over the field of view.

3.2.4.3 Spectral and temporal analysis

The source energy spectrum and light curve - i.e. the energy and temporal distributions of photons - can finally be determined. The standard spectral analysis is performed with a forward-folding technique [66]. The reconstruction of the energy spectrum requires an initial hypothesis on the spectral shape with a given set of free parameters. It is generally taken as a power law that can be broken or have an exponential cutoff. Then, the photon detection predicted with this model is generated while taking into account the instruments response and atmospheric conditions. This step provides expected counts of gamma-rays and background events. The predicted detection is then compared with the observed signal in the ON and OFF

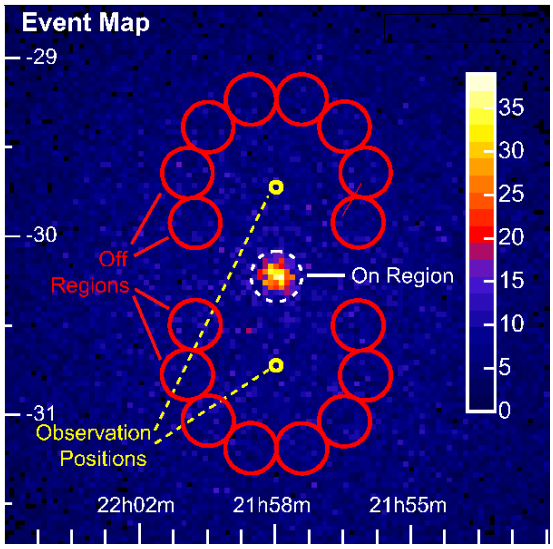

Figure 3.5: Reflective background technique applied to an observation with two runs. Credit: [64].

regions to provide the likelihood of this model to be the real one. The set of free parameters that maximises the likelihood function is finally taken as the "true" model parameters.

The light curve can then be determined from the reconstructed energy spectrum. For each time step (bin), the number of signal events n_γ and background events n_{bkg} are obtained from the reconstructed spectrum, and normalised based on the number of events observed in the ON and OFF regions (N_{ON} and N_{OFF}), using either a statistical treatment or by using the excess number of events. Each point in the light curve is then produced by integrating the renormalised spectrum over the associated time step.

3.3 CTA: the Cherenkov telescope array

The Cherenkov telescope array (CTA) observatory[9] is a global effort involving about 150 institutes from 25 countries. It is divided in two arrays of IACTs, one in each hemisphere, meant to come after the currently operating experiments H.E.S.S., MAGIC and VERITAS. The North site is located in La Palma (current location of MAGIC telescopes) while the South site will be in the Atacama desert in Chile. The choice of a double array was made to achieve an almost complete coverage of the night sky.

CTA flux sensitivity is expected to be at least one order of magnitude higher than that of currently operating experiments as can be seen in Figure 3.6. It is meant to enable the detection of fainter fluxes, with extended energy range, larger detection areas, improved angular resolution and wider field of view. This is achieved with the implementation of multiple sizes of telescopes as presented in Figure 3.7:

- **Large sized telescopes (LST):** with a 23 m diameter reflecting dish (370 m^2 detection area) and 4.3 degrees FoV, they are most sensitive to low energy showers ranging from 20

[9]Detailled informations about CTA can be found in the dedicated website https://www.cta-observatory.org/

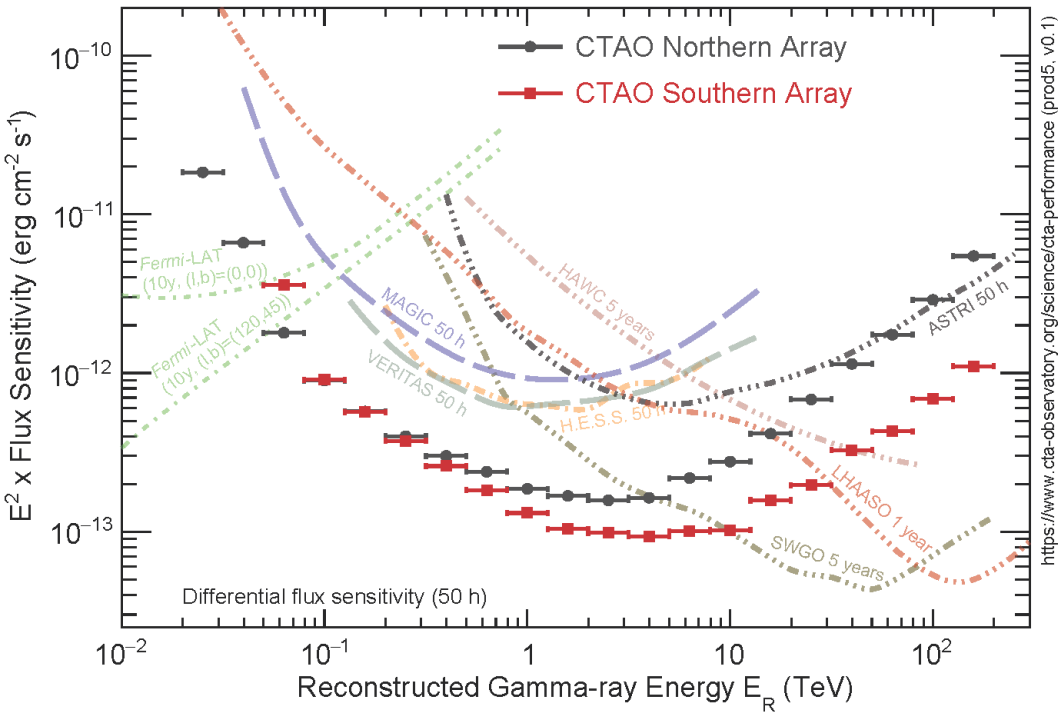

Figure 3.6: Comparison of the expected flux sensitivity of CTA (50h) with current experiments. Credit: CTA collaboration (https://www.cta-observatory.org/science/ctao-performance/).

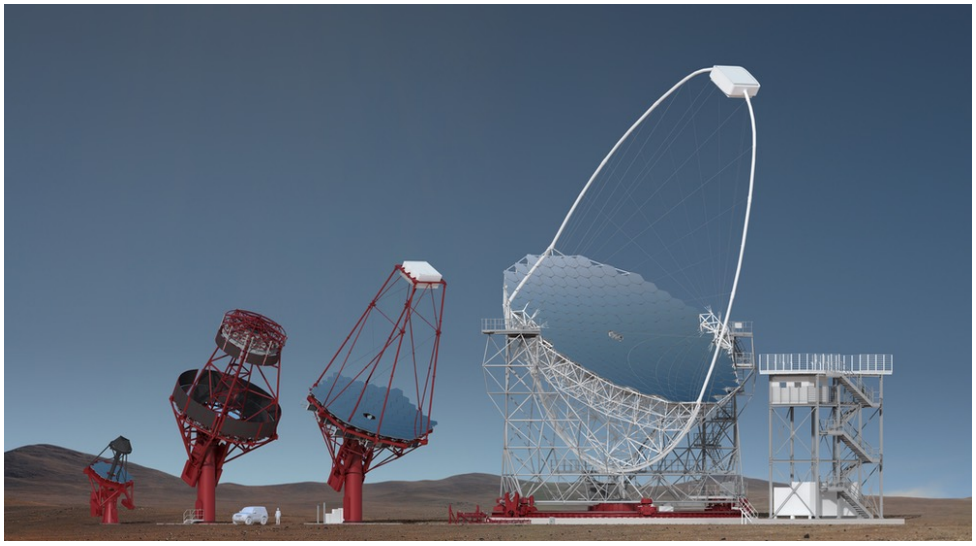

Figure 3.7: Illustrated view of the CTA telescopes. From left to right: SST, SCT, MST and LST. Credit: CTA collaboration.

to 150 GeV. They are designed to achieve short repositioning times (33 seconds for 360 degrees) to catch fast transient phenomena such as GRBs.

- **Medium sized telescopes (MST):** with a 12 m diameter reflecting dish (88 m^2 detection area) and ~ 7.6 degrees FoV, they are most sensitive to the CTA core energies ranging from 150 GeV to 5 TeV. One of the two camera prototypes for MSTs, FlashCam, is currently installed on the H.E.S.S. large telescope for benchmark testing. The other prototype, NectarCAM, has been run and tested on a prototype of MST. An alternative design called SCT (for Schwarzschild-Couder Telescope) was developed in parallel by the U.S. branch and will most likely join the MST network.

- **Small sized telescopes (SST):** with a 4 m diameter reflecting dish (8 m^2 detection area) and 10.5 degrees FoV, they are most sensitive to the highest energies ranging from 5 to 300 TeV. A large number of these telecsopes will be deployed to sample a large area (4.5 km^2).

As many galactic sources are expected to be detectable in the energy range covered by SSTs, the small telescopes will be placed in the southern site only. While the southern site aims to host 4 LSTs, 25 MSTs and 70 SSTs for a focus on galactic and extragalactic sources, the northern site should only host 4 LSTs and 15 MSTs.

A core scientific programme has been defined by the CTA collaboration, expected to employ 40% of the available observing time over the first 10 years of operation [67]. The key science projects include dark matter searches, galactic and extragalactic surveys, monitoring of transients, PeVatrons and AGNs, the study of star-forming systems, etc. The remaining is to be employed for a variety of independent projects selected from observation proposals. All the data collected by the observatory will subsequently be made available to the public. It is now in construction phase. The first and only operating CTA prototype telescope up to date, LST1 (North site), was inaugurated in October 2018 and is currently in commissioning phase. The remaining telescopes are expected to be completed and start operations around 2024. CTA will then inevitably become of major importance in the future decades.

Part II

Modelisation of blazar emission and interpretation of intrinsic delays

Chapter 4

Intrinsic time delays in blazars

Contents

In this chapter we present a blazar model based on a leptonic synchrotron self-Compton scenario and derive all the steps needed to extract energy-dependent time delays. We then provide a full characterisation and interpretation of the time delays and discuss their observability with instruments operating at present or in the near future. The content introduced in this chapter has been presented at the TeV Particle Astrophysics conference (TeVPA, 2019).

4.1 Time-dependent modeling of blazar

Several time dependent AGN emission models have been proposed in the litterature uncovering the existence of intrinsic time delays generated from emission mechanisms [68, 69, 70, 71, 72, 73]. A full study on intrinsic delays in blazars (restricted to BL Lacs) has been proposed by Perennes et al. [74] further interpreting their origin and highlighting the significant impact model parameters can have on delays' amplitude and behaviour. We reproduced the model used for the aforementionned study and brought it a step further by presenting intrinsic delays evolution under a new approach, as well as extend the model to a richer description. Further improvements have been incorporated to better compare intrinsic delays from LIV induced delays, as will be discussed in Chapter 5.

4.1.1 Generating a flare

As discussed in Chapter 2, the gamma-ray spectrum emitted by blazars takes its origin from knots i.e. compact zones of condensed ultra-relativistic matter (leptonic or lepto-hadronic plasma) with a stronger magnetic field than that of the ambient jet. Due to the relativistic beaming effect (see Section 2.1.1), blazars emission models can be limited to the description of these knots.

To study intrinsic delays, ones that are inevitable and necessarily arising from emission mechanisms, we first build a minimalist model based on the most fundamental processes needed to generate a flare: acceleration and radiative SSC cooling. This will be used as a foundation for the interpretation of intrinsic delays behaviour arising in BL Lacs, before adding adiabatic expansion/compression and external photon fields to extend the description to FSRQs. For a coherent approach to the minimalist restriction, we choose to work with leptonic models that are extensively used in the litterature to describe flares evolution and are fairly constrained, thus limiting the number of free parameters to juggle with. Although they start to show their limitation, they are still considered as reference models by the astrophysics community providing reliable descriptions of blazar flares.

4.1.1.1 Homogeneous one-zone SSC model

Working towards simplicity of the model, we choose to describe the emitting zone with only one spherical bulk of dense leptonic plasma, the surrounding jet medium being neglected. A generic transfer equation - the Ginzburg-Syrovatskii equation [75] originally intended to describe the evolution of the number density $N(\vec{r}, t, \gamma)$ of cosmic rays - can be used to describe our bulk's plasma evolution. For a type of particle i created at time t_0 - in this case electrons or positrons - the Ginzburg-Syrovatskii equation for $N_i(\vec{r}, t, \gamma)$ with dependencies on position $\vec{r}$, time t and

Lorentz factor $\gamma = (1-\beta^2)^{-1/2}$ reads

$$\frac{\partial N_i}{\partial t} - \nabla(D_i \nabla N_i) + \frac{\partial}{\partial \gamma}(b_i N_i) - \frac{1}{2}\frac{\partial^2}{\partial \gamma^2}(d_i N_i) = Q_i - p_i N_i + \sum_k p_i^k N_k. \tag{4.1}$$

On the left hand side, $D_i(\vec{r},t,\gamma)$ is the diffusion coefficient, $b_i(t,\gamma) = d\gamma/dt$ describes the systematic Lorentz boost change $\Delta\gamma$, and $d_i(t,\gamma) = d(\Delta\gamma)^2/dt$ the fluctuations in this Lorentz boost change. The right hand side deals with injection and loss of particles: $Q_i(\vec{r},t,\gamma)$ is the source term describing injection of particles, $p_i = nv\sigma_i$ is the probability particles i will suffer a destructive collision and $p_i^k = nv\sigma_{ik}$ is the probability of appearance of particle i due to collisions between particles k. n is the particle density, $v = \beta c$ the particle velocity and σ the cross section of the interaction. The plasma is considered as inert such that its volume stays constant throughout time - i.e. there is neither expansion nor compression of the bulk. To simplify this model, we make the following assumptions:

- the plasma is homogeneous and emitting isotropically, freeing ourselves from the spatial component $\vec{r}$ and leading to $\nabla N_i = 0$;
- the second order Lorentz boost changes (fluctuations) are neglected leading to $d_i(t,\gamma) = 0$;
- all injection, escape, creation and loss of particles are neglected freeing ourselves from the right hand side of the equation.

The lepton number density in a minimal scenario is finally described by the following equation:

$$\frac{\partial N(t,\gamma)}{\partial t} + \frac{\partial}{\partial \gamma}\{b_i(t,\gamma)N(t,\gamma)\} = 0, \tag{4.2}$$

where $N(t,\gamma)$ is given in cm^{-3}.

Following Katarzynski et al. treatment [71, 76] an analytical solution can be found at the expense of further simplifications.

Acceleration

Particle acceleration can be explained with shock and stochastic processes or magnetic reconnection (c.f. Section 2.2.1). These mechanisms can be approximated with a simple parametrisation which is no longer dependent on the particles Lorentz boost γ:

$$A(t) = A_0 \left(\frac{t_0}{t}\right)^{m_a}, \tag{4.3}$$

with A_0 the initial acceleration amplitude given in s^{-1} and m_a the evolution index. These two parameters are taken as independent of other parameters that could induce an acceleration (e.g. independent of the magnetic field). t_0 is the characteristic evolution time expressed in seconds, taken as the time needed for a sound wave to propagate through a spherical bulk of relativistic plasma of radius r. In our specific case, r is the initial and constant radius we denote R_0 and

$$t_0 = \frac{R_0}{c/\sqrt{3}}. \tag{4.4}$$

The variation of Lorentz boost due to the acceleration can then be expressed as a function of this parameterisation and reads

$$b_{\rm acc}(t,\gamma) = \gamma A(t) = \gamma C_{\rm acc}(t). \tag{4.5}$$

Cooling

As they are accelerated, particles immediately start to cool down through synchrotron and synchrotron self-Compton (SSC) processes as a result of their interaction with the bulk's magnetic field $B(t)$ (see Section 2.2.2). Following the above acceleration treatment, we parameterise the magnetic field which then reads

$$B(t) = B_0 \left(\frac{t_0}{t}\right)^{m_b}, \tag{4.6}$$

with B_0 the initial magnetic field strength given in mG, and m_b the evolution index. From Equations 2.14 and 2.32, both processes radiate with a power $P_{\rm rad} \propto \gamma^2$. Consequently, the variation of Lorentz boost γ induced by the two cooling processes - synchrotron and inverse Compton - can be expressed in the Thomson regime as follows:

$$b_{\rm syn}(t,\gamma) = \gamma^2 \frac{4\sigma_T}{3m_e c} U_B(t), \tag{4.7}$$

$$b_{IC}(t,\gamma) = \gamma^2 \frac{4\sigma_T}{3m_e c} U_{\rm syn}(t), \tag{4.8}$$

where σ_T is the Thomson cross-section and m_e is the electron rest mass. $U_B(t) = B^2(t)/8\pi$ and $U_{\rm syn}$ are the magnetic and synchrotron fields energy density. The energy density is related to the radiated intensity as follows

$$U(t) = \frac{4\pi}{c} \int_0^\infty d\nu I(\nu). \tag{4.9}$$

From Equations 4.9 and 2.12, it comes the energy density associated to the synchrotron photon field is given by

$$U_{\rm syn}(t) = \frac{4\pi}{c} \int_0^\infty d\nu I_{\rm syn}(\nu) \equiv \int_0^\infty d\gamma\, b_{\rm syn}(t,\gamma) N(t,\gamma), \tag{4.10}$$

with $N(t,\gamma)$ the bulk's lepton density. We then introduce the function $\eta(t)$ defined as

$$U_{\rm syn}(t) = \frac{U_B(t)}{\eta(t)}, \tag{4.11}$$

from which we can rewrite the cooling parameter as follows:

$$b_{\rm rad}(t,\gamma) = \gamma^2 \frac{4\sigma_T}{3m_e c} U_B(t) \left(1 + \frac{1}{\eta(t)}\right) = \gamma^2 C_{\rm rad}(t), \tag{4.12}$$

where $C_{\rm rad}(t) \propto B^2(t)$. The leptons transfer equation finally becomes

$$\frac{\partial N(t,\gamma)}{\partial t} = \frac{\partial}{\partial \gamma} \left\{ \left[C_{\rm rad}(t)\gamma^2 - C_{\rm acc}(t)\gamma \right] N(t,\gamma) \right\}. \tag{4.13}$$

However, the $\eta(t)$ function is too complex to find an analytical solution to Equations 4.13. Additional simplifications are therefore necessary. Although it is quite distant from reality, the easiest simplification we can implement is to replace the $\eta(t)$ function by a constant scalar η, thus introducing a systematic error into the solution that is time-dependent. This error can be kept to a minimum when the η term is kept large. In other words, the solution and subsequent spectra we obtain are trustworthy and close to the real solution when the scalar term η is relatively large. We consider the error on the solution to be acceptable for $\eta \geq 1$.

To fully work out the analytical solution, an initial condition must be provided. We choose to impose a power law with a sharp cut-off at high Lorentz factor that reads

$$N(t_0, \gamma) = N_0 \gamma^{-n} \left[1 - \left(\frac{\gamma}{\gamma_{\rm cut}(t_0)} \right)^{n+2} \right], \tag{4.14}$$

where N_0 is the initial lepton number density, $\gamma_{\rm cut}(t_0)$ is the imposed Lorentz boost cut-off and n is the power law index. We impose a minimum Lorentz factor $\gamma_{\rm min}$ for leptons to start with, and allow the acceleration to boost leptons up to an upper bound $\gamma_{\rm sup}$. Using the above parameterisations, simplifications and initial conditions, we can derive an analytical solution to the transfer equation given in Equation A.1. For interested readers, the full derivation of this solution can be found in Annex A).

4.1.1.2 Extended scenario

External Inverse Compton (EIC) process

The above model which is only fit to properly describe BL Lac emission can be extended to FSRQs by introducing another contribution to the cooling term $b_{\rm rad}(t, \gamma)$. Following the example of an external photon field generated by the accretion disc as presented in Section 2.2.2.3, we compute the energy density associated to external inverse Compton processes. From Equations 4.9 and 2.35, it comes the energy density associated to the external photon field is given by

$$U_{\rm ext} = \Gamma_b^2 \frac{\tau L_{AD}}{4\pi d^2 c}. \tag{4.15}$$

The variation of Lorentz boost γ due to the cooling processes is therefore modified as follows

$$b_{\rm rad}(t, \gamma) = \gamma^2 \frac{4\sigma_T c}{3 m_e c} \left[U_B(t) \left(1 + \frac{1}{\eta} \right) + U_{\rm ext} \right] = \gamma^2 C_{\rm rad}(t). \tag{4.16}$$

Although the additional term $U_{\rm ext}$ is not time-dependent, it results in a non trivial modification of the analytical solution. Indeed, the solution is obtained after multiple integrations. As the SSC and EIC contributions yield expressions with different dependencies, the solutions must be computed separately and take distinct forms (refer to Annex A for more details).

Adiabatic processes

It is possible to relax the constraint on the bulk's radius R_0 previously considered as constant and allow for slow expansion or compression. The radius is no longer a scalar but a time-dependent function that reads

$$R(t) = R_0 \left(\frac{t_0}{t} \right)^{-m_r}, \tag{4.17}$$

with $R_0 \equiv R(t=0)$ the initial bulk's radius given in cm, and m_r the evolution index encoding expansion for positive values and compression for negative ones.

Assuming a uniform adiabatic evolution and introducing $\vec{v}(t) = v(t)\frac{\vec{R}(t)}{R(t)}$, the adiabatic coefficient and associated Lorentz boost evolution read

$$C_{\rm adia}(t) = \frac{1}{3}\vec{\nabla}\vec{v} = -\frac{m_r}{t}, \tag{4.18}$$

$$b_{\rm adia}(t) = \gamma C_{\rm adia}(t). \tag{4.19}$$

Additionaly, the lepton density $N(t,\gamma)$ which is defined with respect to the bulk's volume must be modified accordingly. The bulk's expansion/compression can be accounted for by introducting an evolution term to the lepton number density:

$$N^*(t,\gamma) = N(t,\gamma)\left(\frac{t_0}{t}\right)^{3m_r}, \tag{4.20}$$

such that $N^*(t,\gamma) = N(t,\gamma)$ for $m_r = 0$, i.e. when the bulk's radius stays constant through time. The transfer equation finally becomes

$$\frac{\partial N^*(t,\gamma)}{\partial t} = \frac{\partial}{\partial \gamma}\left\{\left[C_{\rm rad}(t)\gamma^2 - (C_{\rm acc}(t) - C_{\rm adia}(t))\gamma\right]N^*(t,\gamma)\right\}. \tag{4.21}$$

The extra cooling term brought by the external field contribution adds a simple and independent term to the solution. The sign attributed to the adiabatic coefficient determines whether it contributes to expanding or compressing the bulk's volume. If negative, the bulk is expanding and a loss of energy is embedded, working against the acceleration; if positive, the bulk is compressing and contributes to energy gains together with the acceleration processes.

4.1.1.3 Domains of parameters

In addition to the conditional validity where we impose $\eta \geqslant 1$, the use of parameterisations leads to forbidden areas in the parameter space for the analytical solution. All the validity conditions discussed below are summarised in Table 4.1.

Minimalist scenario

The simplest form of the transfer equation involves only two parameterised functions, the acceleration and the magnetic field. From the solution S (c.f. Equation A.1 of Annex A), we must exclude the cases with evolution rates $m_a < 0$ and $m_b < 0$ that would otherwise lead to divergent integrals. Besides, as $A_0 < 0$ would lead to acceleration behaving as a random cooling process, we impose $A_0 > 0$. Furthermore, since we consider there is no particle injection, we must have $m_a > 0$. From the way we define the magnetic field, we necessarily have $B_0 > 0$. As it is bound to decay with time as the bulk moves away from the AGN core where the magnetic field is at its strongest, we must have $m_b > 0$.

Given the solution involves the integral of a term inversely proportional to m_a, we need to differentiate between the cases where $m_a = 1$ and $m_a \neq 1$.

When $m_a = 1$ - the acceleration evolves linearly with time - the solution takes its simplest form and the only requirement is to avoid divergences leading to $m_b - A_0 \neq 1$. When $m_a \neq 1$, an

incomplete gamma function (c.f. Equation A.16) has to be involved to achieve a solution and imposes $m_a > 1$ and $m_b \geqslant 1$.

Adiabatic processes

When introducing adiabatic processes, we make use of an extra parameterisation - the radius function $R(t)$ - which takes a slightly different form from the others. The evolution rate m_r is allowed to take negative values to account for the bulk's compression, but also be set to zero which leads back to the most basic case governed by Equation 4.13. Let us add that this description is valid for limited durations and limited radius variations only. Indeed, an indefinite or excessive expansion (resp. compression) would lead to the bulk "evaporating" (resp. tending towards a singularity) in which case the model would no longer hold.

While the derivation is not straight forward, the extra term in m_r can be factorised with the existing solution. A simple treatment is allowed where one can substitute m_b with $m_b + m_r$.

Again, we need to differentiate between the cases $m_a = 1$ and $m_a \neq 1$. From this simple substitution, we can easily retrieve the conditions from the basic equation case: $m_a = 1$ requires $m_b + m_r - A_0 \neq 1$ while $m_a \neq 1$ requires $m_a > 1$ and $m_b + m_r \geqslant 1$.

External inverse Compton processes (FSRQ treatment)

Even if the external photon field does not introduce another parameterisation, it does change the solution and imposes new constraints on the parameter space.

Once again, the two cases where $m_a = 1$ and $m_a \neq 1$ need to be considered. For $m_a = 1$, the constraints are doubled: we need both $m_b - A_0 \neq 1$ and $m_b + m_r - A_0 \neq 1$ meaning we also must have $m_r \neq m_b - A_0$. For $m_a \neq 1$, a second incomplete gamma function is needed and combining the forbidden parameter space we must now have $m_a > 1$, $m_b + m_r \geqslant 1$ and $m_r > 1$ which means we *necessarily have adiabatic expansion when introducing external photon fields.* This also means we cannot have adiabatic compression together with EIC treatment which is a reasonnable condition. Be that as it may, the model only requires a small expansion rate to fall back to a valid description.

Conditions	pure SSC	SSC + adiabatic	SSC + adiabatic + EIC
general	$\eta \geqslant 1$	$\eta \geqslant 1$	$\eta \geqslant 1$
	$A > 0$	$A > 0$	$A > 0$
	$B > 0$	$B > 0$	$B > 0$
	$m_b > 0$	$m_b > 0$	$m_b > 0$
$m_a = 1$	$m_b - A_0 \neq 1$	$m_b + m_r - A_0 \neq 1$	$m_b - A_0 \neq 1$
			$m_b + m_r - A_0 \neq 1$
			$m_r \neq m_b - A_0$
$m_a \neq 1$	$m_a > 1$	$m_a > 1$	$m_a > 1$
	$m_b \geqslant 1$	$m_b + m_r \geqslant 1$	$m_b + m_r \geqslant 1$
			$m_r > 1$

Table 4.1: List of the necessary conditions on parameters for the model to be valid.

4.1.2 Generating astrophysical observables: the AGNES simulator

The minimalist model described above was first implemented to a simulation code by Katarzynski et al. [71, 76]. It was later on adapted to time delay studies by Perennes et al. [74] with the introduction of temporal evolution and intrinsic time delay treatment. For this work, an optimisation was performed while being entirely re-written into a more stable and user-friendly software called *AGN Evolution Simulator (AGNES)* that is planned to be made open to public. This new version now incorporates the extended model with adiabatic and EIC processes, but also a LIV treatment which will be introduced and fully exploited in Chapter 5.

Reference set of model parameters

We introduce here a reference set of model parameters listed in Table 4.2 to be used in the simulations where we distinguish SSC emission, evolution and EIC parameters. The SSC set has been formed based on the archetypal Mkn 501 TeV-emitting BL Lac, whereas the evolution set has been chosen such that the generated flare would last a couple hours. In contrast, the EIC set is chosen to translate conditions with an strong EIC component of various intensity. As little to none time delays have been detected so far, the parameters have been chosen to yield suppressed time delays which best represent current observations (more in Section 4.2.2.2).

	SSC parameters	Value	Unit
Redshift	z	0.03	-
Doppler boost	δ_b	40	-
Magnetic field strength	B_0	87	mG
Bulk radius	R_0	5×10^{15}	cm
Lepton density	N_0	300	cm^{-3}
Lorentz boost min	γ_{min}	2	-
Lorentz boost cut-off	γ_{cut}	4×10^4	-
Power law index	n	2.4	-
	Evolution parameters		
Acceleration strength	A_0	4.5×10^{-5}	s^{-1}
Acceleration evolution rate	m_a	5.6	-
Magnetic field evolution rate	m_b	1	-
Bulk radius evolution rate	m_r	0	-
	EIC parameters		
Blackbody temperature	T	1.5×10^5	K
Re-emission factor	ρ	1	-
Accretion disc luminosity	L_{AD}	1×10^{41}	$\mathrm{erg.s}^{-1}$
Bulk-disc distance	d	5×10^{17}	cm

Table 4.2: List of reference input parameters.

4.1.2.1 Lepton spectrum

From the analytical solution, we can build lepton spectra and track the lepton number density evolution over time. Figure 4.1a shows the distribution for $\gamma^2 N_t(\gamma)$ in logarithmic scale for better graphical readability. As time increases, the sharp Lorentz boost cut $\gamma_{\mathrm{cut}}(t)$ is pushed towards higher values while the overall flux increases until the most energetic leptons reach γ_{max}

at time $t_{\max}$. Past this point, these leptons start to lose their energy and slowly decelerate. By fitting a power law with a sharp cut-off over these spectra, we can retrieve the evolution of $\gamma_{\rm cut}(t)$ translating into the maximal Lorentz boost reached by leptons as shown in Figure 4.1b from which we can extract the quantity $t_{\max}$.

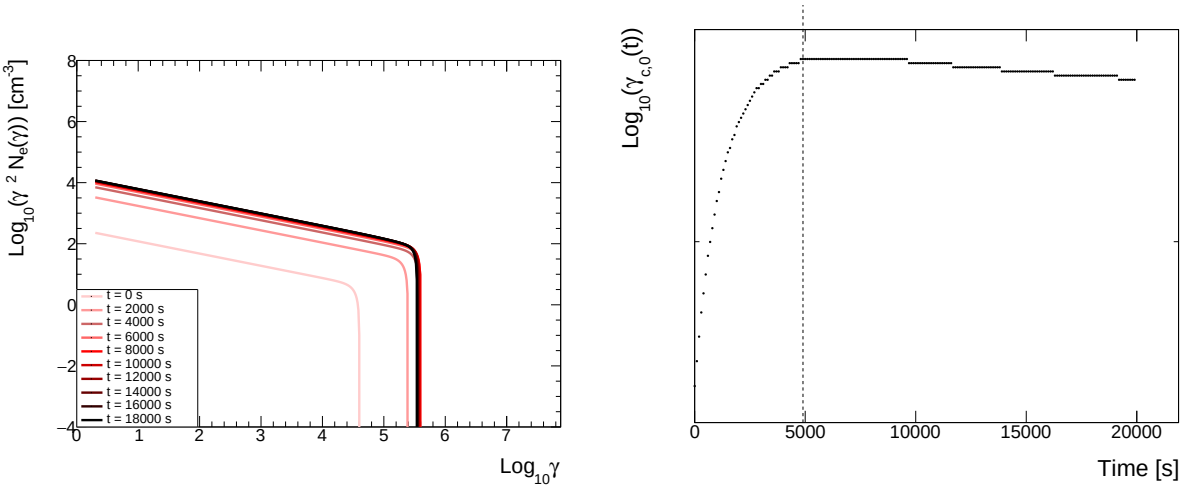

(a) Evolution of leptons spectra with time generated with the reference set paramters listed in Table 4.2 (reads from light red to black curves).

(b) Evolution of the Lorentz boost cut $\gamma_{\rm cut}(t)$ with time. The vertical line denotes the time $t_{\max}$ at which leptons reach their global maximum Lorentz factor (here $\gamma_{\max} \simeq 5.58$ and $\gamma_{t=20000} \simeq 5.51$).

Figure 4.1: Lepton spectra and tracking of gamma maximum value.

4.1.2.2 Energy spectrum

The next step is to build the energy spectrum that characterises the source. To do that, we need the radiation transfer occurring in the bulk, involving both synchrotron and inverse Compton processes derived in Section 2.2.2. The total radiated flux can be expressed as the sum of synchrotron and inverse Compton fluxes with an EBL absorption correction following Kneiske et al. model [77, 78]:

$$F(\nu_{\rm obs}, t) = F_{\rm syn}(\nu_{\rm obs}, t) + F_{IC}(\nu_{\rm obs}, t) \exp[-\tau_{\rm ebl}(\nu_{\rm obs}, z)]. \tag{4.22}$$

From this quantity, we can build spectral energy distributions as seen in the observer frame at specific time t. This can be seen in Figure 4.2 with the evolution of $\nu_{\rm obs} F_t(\nu_{\rm obs})$ as a function of energy $E = h\nu_{\rm obs}$ in logarithmic scale for a better graphical readability. Computing SEDs for each time step allows for a visible evolution over time. We observe here a similar behaviour as was found for lepton spectra. It begins with a fast acceleration phase translating into an increase in flux and energy until a maximum is reached, and is followed by a strong cooling phase where flux and energy slowly decrease.

4.1.2.3 Light curves and intrinsic time delays

While SEDs have been derived from the projection of the radiated flux $F_t(\nu_{\rm obs})$ on energy, light curves use the couterpart projection on time $F_{\nu_{\rm obs}}(t)$. Going from one form to the other can be done by integrating over energy or time. More specifically, the light curves flux over a

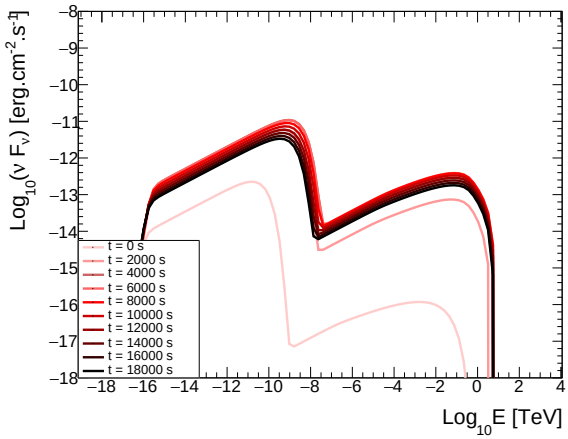

Figure 4.2: Evolution of observed spectral energy distributions with time, generated with the reference set of parameters listed in Table 4.2 (reads from light red to black curves).

given energy band is obtained with the following transformation:

$$F_{LC,\nu_{\rm obs}}(t) = \int_{\nu_{\rm min}}^{\nu_{\rm max}(t)} d\nu_{\rm obs}\, \frac{F(\nu_{\rm obs}, t)}{\nu_{\rm obs}}. \tag{4.23}$$

Light curves

The evolution of light curves over energy can be seen in Figure 4.3, where the curves have been normalised. As it was the case for lepton spectra and SEDs, temporal distributions are characterised by a strong acceleration phase with an increase in flux, before reaching a maximum where the cooling phase takes over leading to the flux decaying. Furthermore, as dictated by the lepton spectra evolving according to a decreasing broken power law, light curve flux decreases as energy increases. Above a certain energy threshold, the flux drops drastically (typically falling from 10^{-15} to 10^{-50} erg.cm^{-2}.s^{-1}) and becomes too small to be significant.The light curves on these energy bands are therefore excluded from the analysis and interpretations. Besides, from Figure 3.6, current generation of IACTs have a flux sensitivity over a 50h run reaching down to $\sim 10^{-12}$ erg.cm^{-2}.s^{-1}. The future observatory CTA will extend this threshold to $\sim 10^{-13}$ erg.cm^{-2}.s^{-1}. This cut is therefore approximately in accordance with contemporary instrument performances.

Delays estimation

Each light curve can be characterised by a typical arrival time of photons, chosen to be the time at which the light curve flux is peaking. The evolution over energy of light curves thus gives access to the evolution over energy of the arrival times. To estimate temporal delays as per energy band centered on $E = h\nu_{\rm obs}$, we need a reference arrival time we will write as $t_{\rm ref}$. The time delays are then given by

$$\Delta t_E = t_E - t_{\rm ref}. \tag{4.24}$$

- $\Delta t_E < 0$ when the light curve centered on E starts to decay *before* the reference light curve;

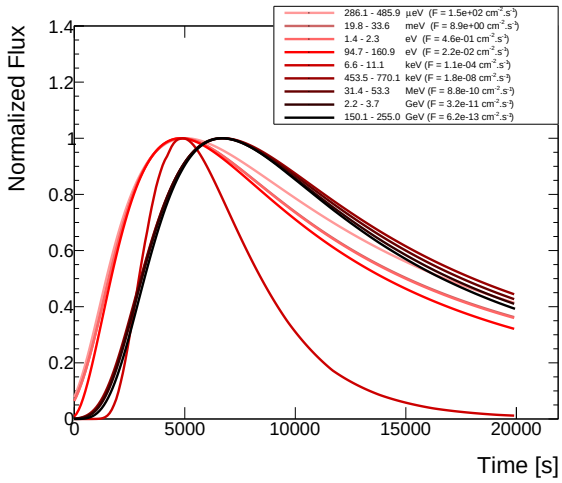

Figure 4.3: Normalised light curves generated with the reference set of parameters listed in Table 4.2 (reads from light red to black curves).

- $\Delta t_E > 0$ when the light curve centered on E starts to decay *after* the reference light curve.

In the specific case shown in Figure 4.4 where $t_{\text{ref}} = t_{E=1\text{MeV}}$ and the delays are flat, the photons tend to arrive at the same time as the chosen reference arrival time. Note that since all light curves start at $t = 0$, peaks necessarily occur at $t_E > 0$ and the positiveness or negativeness of the delays are solely dependent on the chosen reference time. We are primarily interested in the time delay evolution with respect to energy.

Since we compute all observables over energy and time bands, light curves in particular are binned such that the precision on the typical arrival time is defined by the chosen time step. In theory we could greatly increase the precision by computing light curves over a very fine time step. However, the smaller the time step in a given time window, the larger the number of bins in that window and the longer the computational time. To obtain finer precision as well as reasonable computational time, we introduced a new feature to the existing code which performs a fitting of the light curves peak. Since light curve distributions can get complex forms and the region of interest is only a small fraction of the curves, we chose to only focus on a very small time window around the peak which can be fitted with a parabola function. A comparison between these two extraction methods shows the fitting method provides better precision to delay estimation than the binning method for equal or smaller time steps as can be seen in Figure 4.4. The vertical and horizontal error bars correspond to respectively the width of time and energy bins. Since the fitting method brings infinitesimal precision to the time estimation, we deemed reasonable to remove the vertical error bars.

4.2 Properties of intrinsic time delays

Intrinsic delays navigate between two types of regimes in the SSC scenario. The notion of positiveness or negativeness of Δt_E is no longer relevent when considering sets of delays as it solely depends on the chosen reference time. Instead, we consider the trends where delays are either increasing or decreasing.

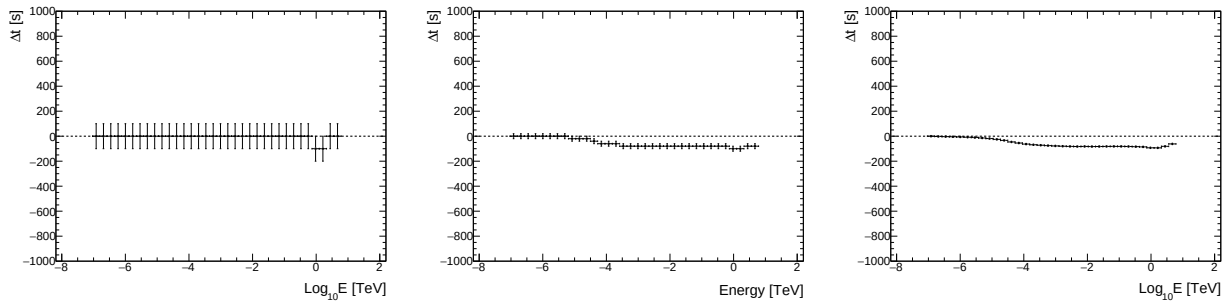

(a) Binning method, 100 s time step.

(b) Binning method, 20 s time step.

(c) Fitting method, 100 s time step.

Figure 4.4: Comparison between two extraction methods of time delays generated with the reference set of parameters listed in Table 4.2. Delays obtained by extracting the mean abscisse value (time) from the bin with maximum value (flux) for both 100 s (a) and 20 s (b) time steps in the light curves; and by fitting a parabola over a small time window around the light curve peak (c) for 100 s time steps in the light curves.

4.2.1 Regimes in the SSC scenario

These two trends arise from an inbalance between the acceleration and the cooling processes. Leptons start to emit photons as soon as they get accelerated such that both processes take effect simultaneously but with different strength or "efficiency", leading to one process dominating the other. To explain the mechanisms at play, we make use of the time $t_{\max}$ at which the most energetic leptons stop being accelerated (their energy losses start to dominate over their energy gains) and compare it to the times t_E at which light curves reach their maximum and start to decay.

Increasing trend - slow acceleration regime

Increasing delays are associated with leptons reaching their $\gamma_{\max}$ after light curves start to decay: $t_{\max} > t_E$. The acceleration appears to be relatively slow *respective to* the decay processes. Leptons take much longer to be accelerated and high energy photons are emitted later than low energy ones. Light curves decay is then mostly induced by the magnetic field decay. Low energy light curves peak while leptons are still accelerating towards the highest energies, hence before high energy ones.

Decreasing trend - fast acceleration regime

Decreasing delays are associated with leptons reaching their $\gamma_{\max}$ before light curves start to decay: $t_{\max} < t_E$. The acceleration appears to be relatively fast *respective to* the decay processes and the most energetic leptons soon stop accelerating. The decaying of the flare is then mostly due to the radiative cooling. As the radiated power given in Equations 2.14 and 2.32 show a proportionality to γ^2, high energy leptons tend to lose their energy faster than low energy ones, and cooling processes sooner take over acceleration ones. As a consequence, light curves at high energy peak before low energy ones resulting in decreasing delays.

4.2.2 Impact of model parameters on intrinsic delays

A third trend can arise from the combination and overall balance between the two others. Delays do not evolve and seem to cancel out leading to a flat curve showing no variation. The set of reference parameters has been chosen to reproduce this special case. We justify this choice with two arguments: no significant time delay has been detected yet, with the exception of one case (c.f. Section 4.2.3 or 6.2.1) such that flat trends are closest to observations. It brings a new approach to the parameter study that was previously performed allowing us to extract further information on intrinsic time delays. This state is found to be fairly unstable such that slight variations in parameters can easily send delays along one trend or the other.

4.2.2.1 SSC scenario

We present here the new approach to this study where only parameters that have a significant impact on regimes are discussed. All the evolution plots have been regenerated and shown in Figure 4.5 (visible at the chapter). Parameters are being varied about their chosen reference value (see Table 4.2) represented by the neutral black distribution within the validity domain of parameters. Blue distributions correspond to lower values of the studied parameter, while red distributions correspond to larger values.

Low energy domain - $E \lesssim 100$ MeV

The evolution in the lower energy domain is almost entirely determined by the minimum Lorentz factor γ_{min} as can be seen in Figure 4.5h. This energy domain was never properly explored in previous studies as it is of little interest for LIV studies.

At low values (here $\gamma_{\text{min}} \sim 1$) there is no visible effect on the delays and the trend is flat. At intermediate values (here $2 \leq \gamma_{min} \leq 200$) only the $\Delta t_{E \lesssim 100\text{MeV}}$ are affected while $\Delta t_{E>100\text{MeV}}$ are still plateauing. This is easily explained in terms of acceleration time scales. Indeed, a large γ_{min} means leptons start with intermediate energies (no acceleration needed up to this energy), hence greatly reducing or canceling the acceleration time scales at low energies. We then place ourselves in the fast acceleration regime where delays are decreasing. As γ_{min} gets larger, higher energy leptons start to become affected, and the fast acceleration regime extends towards higher energy domains of intrinsic delays.

High energy domain - $E > 100$ MeV

Contrary to the γ_{min} parameter, the vast majority of parameters only affect high energy domains of intrisic delays.

- The **acceleration** is the only contributor to energy gain for leptons, hence one of the parameters with the most important impact on regime determination.

  - **Acceleration strength A_0.** At low values, the acceleration is weak and leptons take longer to reach high energies, hence evolving in the slow acceleration regime where delays are increasing. For large values, leptons quickly reach high energies, thus evolving in the fast acceleration regime where delays are decreasing (see Figure 4.5a).

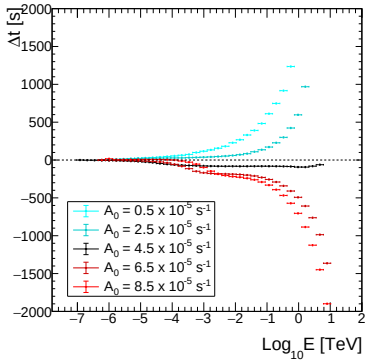

(a) Initial acceleration A_0.

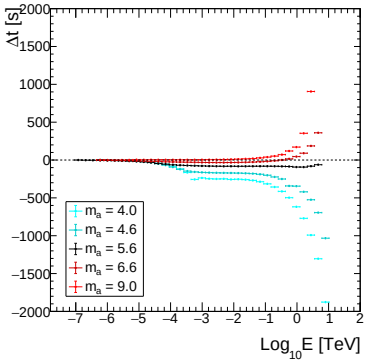

(b) Acceleration evolution rate m_a.

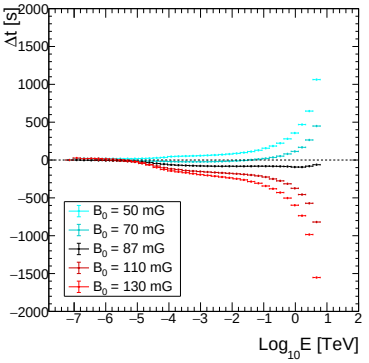

(c) Initial acceleration B_0.

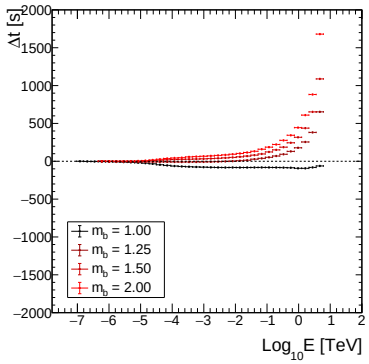

(d) Acceleration evolution rate m_b.

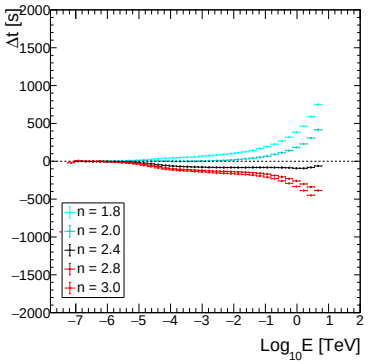

(e) Power law index n.

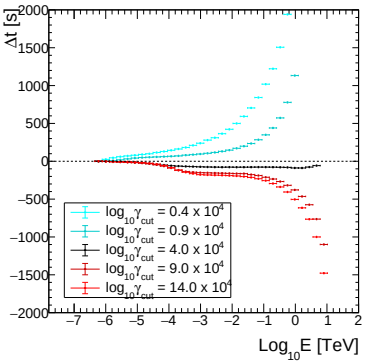

(f) Lorentz factor cut-off $\gamma_{\rm cut}$.

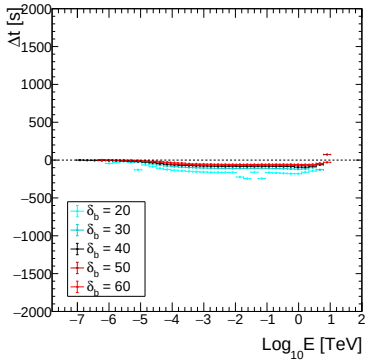

(g) Doppler factor δ_b.

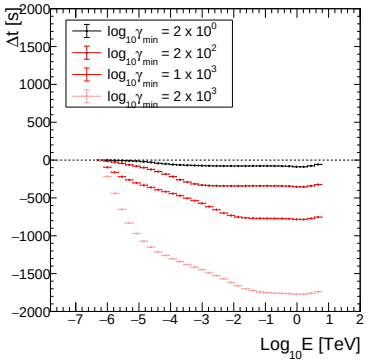

(h) Minimum Lorentz factor cut-off $\gamma_{\rm min}$.

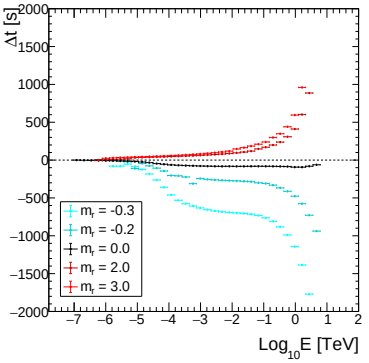

(i) Evolution rate of the bulk's radius m_r.

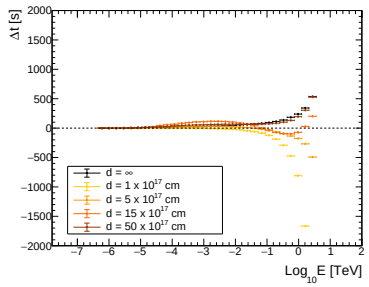

(j) Bulk-disc distance d.

Figure 4.5: Time delays evolution with respect to various model parameters.

  - **Acceleration evolution rate m_a.** In order to properly intiate the flare at a given time, this parameter has been defined such that the acceleration can only decay with time. At low values, the acceleration decays slowly, thus staying efficient over a long time scale. Leptons reach the highest energies before the acceleration starts to become relatively inefficient, hence evolving in the fast acceleration regime where delays are decreasing. At large values, the acceleration decays quickly and stays efficient over a short time scale. Leptons need more time to reach the highest energies, hence evolving in the slow acceleration regime where delays are increasing (see Figure 4.5b).

- The **magnetic field** being the prime contributor to radiative cooling, it is also one of the parameters with the most important impact on regime determination. A parallel can be done between A_0 and B_0 as well as between m_a and m_b with inverse contributions.

  - **Magnetic field strength B_0.** At low values, the magnetic field is weak and radiative cooling is not efficient. The light curves decay is then induced by the magnetic field decay, thus placing ourselves in the slow acceleration regime where delays are increasing. At large values, the magnetic field is strong and the light curve decay is induced by radiative cooling thus switching to the fast acceleration regime resulting in decreasing delays (see Figure 4.5c).

  - **Magnetic field evolution rate m_b.** It has also been defined such that the magnetic field decays with time. Remembering we need $m_b \geq 1$ and the reference value is set to 1, we can only test larger values. As m_b increases, the magnetic field decays faster and radiative cooling effects quickly lose in efficiency. The light curves decay is then induced by the magnetic field decay, thus placing ourselves in the slow acceleration regime where delays are increasing (see Figure 4.5d).

- **Lepton spectrum parameters** have no impact on energy gains or losses over time and do not change the balance between lepton acceleration and cooling effects. However they govern the initial lepton distribution which can either establish a stepping stone or drag down the acceleration process.

  - **Power law index n.** It imposes the initial ratio between low and high energy leptons such that the smaller n gets, the larger the population of leptons at high energy at t_0. However it has little to no effect on $\gamma_{\max}$ and $t_{\max}$, but it does change the duration of the flare. At small n, the lepton population is on average more energetic leading to shorter flares and time scales placing ourselves in the slow acceleration regime where delays are increasing. At large values, the lepton population is on average less energetic leading to longer flares and time scales placing ourselves in the fast acceleration regime where delays are decreasing (see Figure 4.5e).

  - **Energy cut-off γ_{cut}.** It defines the maximum energy leptons can reach at t_0. At small values, the gap between γ_{cut} and $\gamma_{\max}$ is large. Leptons need to be accelerated over a longer time scale, which is equivalent to a comparatively slow acceleration regime where delays are increasing. At large values, the gap between γ_{cut} and $\gamma_{\max}$ is small and leptons need to be accelerated over a shorter time scale. This is equivalent to a comparatively fast acceleration regime where delays are decreasing (see Figure 4.5f).

- Finally the **Transformation parameters** have no impact on the temporal evolution in the bulk's frame. However, the emission seen from and by the bulk is different from the one seen by the observer.

  - **Doppler boosting δ_b.** It applies a Lorentz boost leading to time contraction in the observer's frame, but also a variation in energy and flux. As a consequence of time contraction, time delays amplitude decreases as the Doppler factor increases while having no effect on the regime imposed by the rest of the parameter set. In the case of our set of parameters describing the balance between acceleration and cooling with no visible trend, it has no effect whatsoever (see Figure 4.5g).

4.2.2.2 Extended scenario

A similar study is performed here taking into account the parameter validity domains introduced in Section 4.1.1.3.

Adiabatic processes

Adiabatic processes can either contribute to acceleration or cooling processes depending on the variation the bulk's radius will undergo, as can be seen in Figure 4.5i. When the bulk's volume decreases with time, its plasma gets more condensed and is heated up. This rise in energy translates into a gain in kinetic energy, and leptons are naturally accelerated placing delays in the fast acceleration regime with a decreasing trend. On the contrary, when the bulk expands with time, its plasma is diluted and leptons will diffuse their energy. This leads to additional cooling effect placing delays in the slow acceleration regime with an increasing trend.

External inverse Compton processes

Due to the validity conditions that are specific to our description (c.f. Section 4.1.1.3), we cannot have an external field without adiabatic expansion, and more precisely we need $m_r > 1$, we choose to keep the reference set while only modifying the radius evolution rate such that $m_r = 1.001$ now placing intrinsic delays in the slow acceleration regime. The black curve now represents this new reference set where the external photon field is absent (see Figure 4.5j).

At small distances, the external photon field is condensed which has for effect to increase the frequency of inverse Compton interactions and boost the radiating power, placing delays in the fast acceleration regime with a decreasing trend. As the distance increases, the external photon field gets diluted such that the inverse Compton interaction frequency diminishes until they can no longer significantly contribute and only SSC processes are accountable for delays, hence going back to the reference case represented by the black curve.

At intermediate distances, a strange behaviour appears with delays increasing at $E < 1$ GeV, decreasing betweeen $E = 1$ GeV and $E = 1$ TeV, and increasing again at $E > 1$ TeV. We can use two arguments to explain this peculiar behaviour. The external inverse Compton processes are not dependent on synchrotron processes, as opposed to SSC processes which cannot exist without a synchrotron field. Furthermore, the external photon field gets diluted as we go further from the photon source - the accretion disc in this case.

In the SSC scenario, the synchrotron photon field takes some time to build up resulting in the acceleration dominating over cooling processes at early times. As a consequence, we systematically considered the acceleration to be comparatively fast respective to SSC cooling processes at low energies ($E < 100$ MeV). However, the external photon field being static, the frequency of inverse Compton interactions is constant over time and EIC processes compete with the acceleration from the very beginning. The EIC then changes this approach and the acceleration time scale is now comparatively slow compared to cooling ones resulting in increasing delays.

At intermediate energies for such distances, the external photon field is still dense enough to contribute to the cooling processes and boosts cooling effects leading to decreasing delays.

For the highest energies ($E > 1$ TeV), the external photons are too diluted to significantly contribute to the high energy light curves. Therefore, only SSC processes are accountable for the delay behaviour, thus switching once again towards an increasing trend.

4.2.3 Observability of non-zero intrinsic delays

From the above study, intrinsic delays appear to rise quite effortlessly from the variation of sources' physical quantities and properties. However, only one occurrence of significant time delay (4 ± 1 min over $\Delta E \sim 1$ TeV) has been detected so far [79]. This contradiction is usually explained by a lack of precision of the measurements: the uncertainty on measurements are too high and delays are systematically compatible with zero value. A typical uncertainty on measured time delays (equivalent to a 1σ confidence level) for Mkn 501 is ~ 200 s/TeV (see Chapter 7 for a full derivation), the ~ 240 s/TeV measured delay then being too small to be significant.

Time delays arising in AGN emission can only be precisely measured from a flaring episode, as opposed to their quiescent state where no point of reference can be found. Going from one state to the other necessarily involves a variation of physical parameter. Starting from a state where delays are suppressed (reference parameters set), we have shown that intrinsic delays' magnitude increases as parameters move away from their reference values. A natural question arises from this statement: what would be the amount of variation in parameters needed to reach significant detected delays?

As the reference case was built based on the source Mkn 501, a 1σ confidence level can be reached when delays magnitude go beyond $\Delta t \sim 200$ s/TeV. Although this level of significance is not enough to have a proper detection of time delays with current detectors, this may be possible with future instruments. Table 4.3 summarises the results obtained for this study, showing an approached value of each individual parameter needed to generate intrinsic delays of $\Delta t \sim 200$ s/TeV at high energy. The time difference is taken between arrival times of photons at $E = 1$ TeV and $E = 2$ TeV for simplicity. We exclude three parameters from this study: $\gamma_{\min}$ which does not impact high energy delays; δ_b which does not generate intrinsic time delays but only amplifies them; and the EIC with the parameter d which does not have a flat reference curve but also shows a complex behaviour at TeV energies preventing from defining a clear detectability threshold.

A number of parameters such as the magnetic field or the spectral index are well constrained by theory and observations. In addition, extra constraints have been imposed on the reference set of parameters to generate little to none intrinsic delays. In this specific case, reference parameters need to be multiplied or divided by a factor of approximately 1.5 for delays to reach ± 200

s/TeV, hence a variation of 50% in either direction. Other sources may need much larger variations in the parameters to achieve detectability. The need for such a variation can explain why all flares do not provide detectable intrinsic time delays as it may induce quite a dramatic change.

A 50% increase in one or several parameters is still realistic and compatible with observations. For instance, a modeling of the 2006 intense flaring state of the BL Lac PKS 2155-304 suggested a variation by a factor 8 in the magnetic field strength B_0, 1.7 for the Doppler factor δ and 6 for the particle density N_0 [80]. The above study only considered the impact of individual parameters. However, a flaring state should induce variations in many parameters that could lead subsequent intrinsic time delays to be amplified or even cancelled out. This more realistic scenario could also explain the lack of time delay detection in actual observations. A natural extent of this study would then focus on the effect brought on intrinsic delays by combined parameters.

SSC parameters	Δt_{ref}	$\Delta t \gtrsim +200$ s/TeV		$\Delta t \lesssim -200$ s/TeV		Unit
		scale	value	scale	value	
A_0	4.5×10^{-5}	0.78	$< 3.5 \times 10^{-5}$	1.67	$> 7.5 \times 10^{-5}$	s^{-1}
m_a	5.6	1.43	> 8	0.71	< 4	-
B_0	87	0.46	< 40	1.38	> 120	mG
m_b	1	1.5	$> 1.5.0$	-	-	-
γ_{cut}	4×10^4	0.63	$< 2.5 \times 10^4$	5.00	$> 20 \times 10^4$	-
n	2.4	0.63	< 1.5	1.33	> 3.2	-
m_r	0	-	> 1	-	< -0.25	-

Table 4.3: Approximate threshold values for which intrinsic delays become significantly detectable, as compared to their reference value (Mkn 501 case).

Chapter 5

Discrimination between intrinsic and LIV-induced time delays

Contents

We have established the existence and significance of intrinsic delays in blazars in the previous chapter. The need to disentangle between intrinsic and LIV induced time delays is thus getting more pressing in the eventuality of future time delay detection. The reader may have noticed we performed intrinsic time delay studies over a limited energy range, covering in fact only half of the energy range SEDs spread over (on the inverse Compton bump). We motivated this limitation by the LIV framework which effects can only become significant at very high energies, and thus we overlooked the lowest energy ranges (the synchrotron bump). However, time delays can also arise from the synchrotron emission as discussed for instance by Lewis et al. [73].

By choosing to work within the SSC scenario, we *de facto* imposed the inverse Compton emission to be dependent on the synchrotron one. We can then expect SED bumps to evolve together, in a similar fashion. This similarity between energy bands would then also appear in light curves and more importantly in intrinsic time delays. Since LIV effects would only appear in the high energy domain, finding a relationship between sets of intrinsic delays arising in low and high energy domains may allow us to discriminate between intrinsic and LIV-induced time delays. However, this could be hindered by the EBL and Klein-Nishina effects (c.f. Sections 1.3.2 and 2.2.2.2) that tend to suppress the highest energies and introduce an asymmetry between the two domains.

In this chapter, we will present tools developed for the new version of the simulation code we call AGNES, making it a one-of-a-kind software specialising on time delays study and able to treat both intrinsic and LIV effects simultaneously. Lastly, we will discuss the impact of the EBL on this study and complement with observational perspectives. The tools and results introduced in this chapter have been presented at the International Cosmic Ray Conference (ICRC, 2021). A paper covering the content of this chapter is currently in preparation.

5.1 Multi-frequency study: gamma-rays vs. X-rays

Taking once again the reference set of parameters, we extend the previously derived intrinsic delays to X-ray and infrared energies. Note that a standard EBL model (Kneiske et al. [77, 78]) has been taken into account for all the previous results, but also for the results that will follow. To better identify and separate both energy domains, a special care is given to the choice of the reference arrival time $t_{\rm ref} = t_{E_{\rm ref}}$ corresponding to a specific energy $E_{\rm ref}$. We use the energy coordinate of SEDs crevice (low flux region) between the two bumps to specify this quantity. Since the location of the crevice varies between all the generated SEDs, we choose to only consider the one with the highest flux value νF_ν as reference. The energy $E_{\rm ref}$ is then taken as the crevice energy coordinate for that specific SED. $E_{\rm ref}$ ususally varies between 0.01 and 1 MeV.

To highlight the relationship between the two energy domains, we vary one parameter to send delays into one or the other regime. The resulting distributions are shown in Figure 5.1. A clear similarity between the two energy domains (synchrotron and inverse Compton) appears. Let us insist on this strong similarity being a systematic one. Both sets of delays always follow the same trend whichever set of parameters is used to generate them. To fully exploit this potential we want to better estimate and even quantify the degree of similarity, which we attempt with a euclidian distance study. We will further extend this opportunity to SEDs with a study on hysteresis patterns arising in hardness-intensity diagrams.

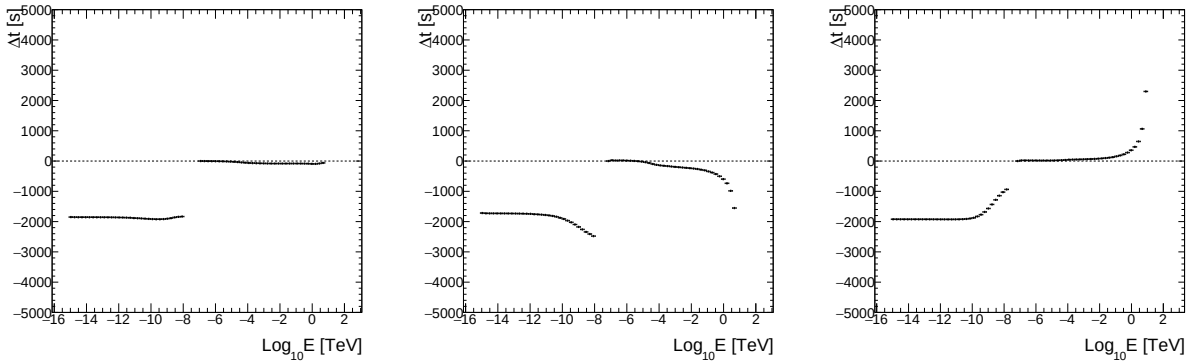

(a) Flat regime. (b) Decreasing regime. (c) Increasing regime.

Figure 5.1: Intrinsic delays extended to low energy spectrum. The synchrotron (low energy) and inverse Compton (high energy) domains behave in a very similar fashion and conserve the time delay trends.

Finally, the introduction of an external photon field would weaken the symmetry between synchrotron and inverse Compton domains as we no longer place ourselves within the pure SSC scenario. The inverse Compton emission would gain a component independent from the synchrotron emission resulting in both domains interdependency being blurred out.

5.1.1 Euclidian distance study

Several methods can be used to estimate the degree of similarity between two distinct sets of data. Although techniques such as cross-correlation, χ^2 minimisation or likelihood maximisation are commonly used for this type of analysis, we chose to work with a euclidian distance method to treat this problem for its simplicity and straightforwardness. The LIV time-of-flight studies which will be discussed at length in the next chapters need a similar treatment for which several methods have been tested (more details in Sections 6.1 and 7.1).

5.1.1.1 Building a powerful tool

The euclidian distance between two data sets $A[i]_{(1\leqslant i\leqslant n)}$ and $B[i]_{(1\leqslant i\leqslant n)}$ containing n points is simply written as:

$$d_E = \frac{\sqrt{\sum_i \left(A[i]-B[i]\right)^2}}{\sqrt{\sum_i \left(A[i]+B[i]\right)^2}}, \tag{5.1}$$

where the denominator is a normalisation term we introduce for a better graphical representation and readability. The scalar d_E possesses two identities we define as follows:

- $d_E = 0$ is the minimum indicating a perfect match between the two data sets, i.e. $A = B$;
- $d_E = 1$ indicates that for all i we have $A[i] = 0$ or $B[i] = 0$.

For this multi-frequency study, we create two data sets: one that contains synchrotron delays (with inverse Compton delays set to zero), and the other containing inverse Compton delays

(with synchrotron delays set to zero). Both sets of delays are extended between $\log_{10} E = -16$ to $\log_{10} E = 2$ (expresssed in TeV), filling the areas where there is no information with zeros. To maximise the sensitivity yielded with Equation 5.1, we rescale all the data points with the first non-zero value Δt_{first}: $\Delta t \longrightarrow \Delta t - \Delta t_{\text{first}}$. This is a treatment inspired from signal processing zero-padding.

With such a configuration the two data sets non-zero values do not overlap and we would necessarily have $d_E = 1$. A solution is to shift one of the data sets over energy (i.e. horizontally) towards the other one to provoke the overlapping and find the optimal displacement that will minimise the euclidian distance d_E.

To estimate this optimal displacement, we introduce a modified version of Equation 5.1 where d_E now becomes a function of the displacement k:

$$d_E(k) = \frac{\sqrt{\sum_i \left(A[i-k] - B[i]\right)^2}}{\sqrt{\sum_i \left(A[i-k] + B[i]\right)^2}}, \tag{5.2}$$

A being the displaced data set. For our study, we compute the distance in logarithmic scale by displacing the synchrotron data set ($\equiv A$) over energy by a quantity $\epsilon = 10^k$ towards the inverse Compton set ($\equiv B$) such that $E_{new} = E \times 10^k$. Although our data sets are discrete, we treat the distributions of time delays as functions and retrieve values with linear interpolations between consecutive points such that k can take any value ($k \in \mathbb{R}$).

Behaviour at low redshift with $z = 0.03$

As a foreword, while the Klein-Nishina effect is inherent to quantum theory, the EBL effect is redhisft-dependent and can thus be minimised by studying sources with small redshift. As the reference set of parameters is inspired by the Markarian 501 blazar which sits at redshift $z = 0.03$, the following results illustrate cases for small redshift and little EBL absorption, leaving the highest energies fairly unaffected.

As was pointed out in Chapter 4, the inverse Compton domain can be separated into two sub-domains of low and high energies. We estimated this separation to occur at $E \sim 100$ GeV, where delays shown mismatched behaviours and distinctive responses to parameters variation. An equivalent seperation for the synchrotron domain seems to occur for $E \sim 0.1$ keV. This leads to the definition of four sub-domains:

- $E < 0.1$ keV: the low energy part of the synchrotron domain (optical-UV, at least 5 decades in energy);
- $E = 0.1 \sim 100$ keV: the high energy part of the synchrotron domain (X-rays, 3 decades in energy);
- $E = 0.1 \sim 100$ MeV: the low energy part of the inverse Compton domain (soft gamma-rays, 3 decades in energy);
- $E > 1$ GeV: the high energy part of the inverse Compton domain (hard gamma-rays, at least 4 decades in energy).

In the context of LIV studies, we are most interested in very high energies (hard gamma-rays) for which LIV effects start to become detectable. The synchrotron domain counterpart then correspond to X-ray energies.

The euclidian distance between the synchrotron and inverse Compton data sets obtained with the reference set of parameters is shown in Figure 5.2a. Let us dissect this curve:

- For $k < 3$, $d_E = 1$ meaning the non-zero values of the two sets of delays do not overlap.
- For $k = 3$ to 8.5, data sets non-zero values start to overlap leading to the distance gradually shifting away from one. Although we imposed a flat regime to the delays, there is a slight decreasing trend such that the distance significantly shifts away from 1 as k increases.
- At $k \sim 8.5$, the overlapping is maximised and the slope is modified.
- At $k \sim 9.2 \equiv k_{\text{min}}$, the euclidian distance reaches a minimum of ~ 0.42, i.e. we reached the optimal displacement for which the two data sets are best matched.
- For $k > 9.2$, we start to lose in similarity and, combined with a shortened overlapping area, the distance slowly tends towards $d_E = 1$.

Let us emphasise that since $d_{E,\text{min}}$ and the maximum overlapping are reached for different displacements k, the minimum is a true minimum and not an artefact due to the zero-padding. In addition, this is a very specific case with little to no variation in the delays, which tends to reduce the sensitivity on the euclidian distance. The distance functions for the two other regimes shown in Figures 5.2b and 5.2c reach lower values (0.25 and 0.20 respectively against 0.42 for the flat case). This is due to the amplified variation leading to a minimum in the distance function which is better defined.

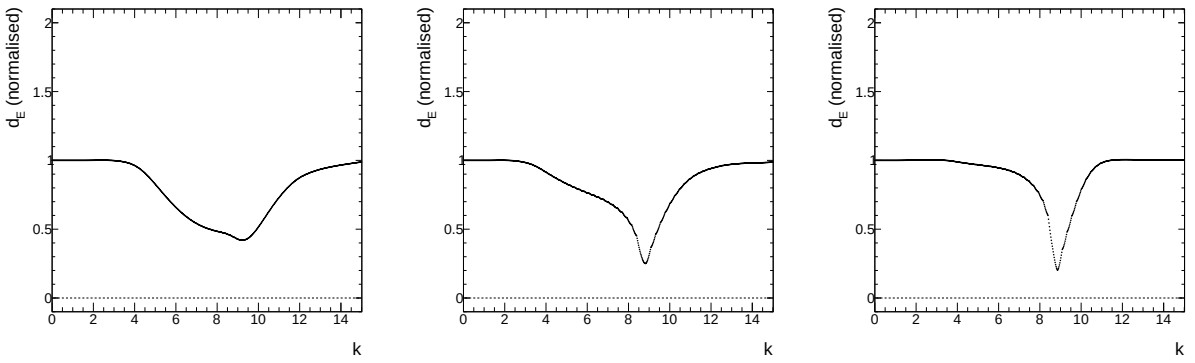

(a) Flat regime. (b) Decreasing regime. (c) Increasing regime.

Figure 5.2: Euclidian distance functions computed between delays from the synchrotron and inverse Compton domains. Each diagram shows a clear minimum defining the optimal displacement k_{min} for which we obtain the best match between the two sets of delays.

Behaviour at high redshift with $z = 1$

At high redshift, the EBL contribution is much stronger hence suppressing the very high energy photon emission. Moreover, a large redshift also means the observed flux is much fainter.

In order to be compatible with CTA sensitivity (c.f. Figure 3.6), only data sets with flux $F > 10^{-20}\text{erg.cm}^{-1}.\text{s}^{-1}$ are used in our analysis. In other words, a selection is made where a threshold is applied to the observable flux. As a consequence, modifying the redshift changes the selection on the data sets and leads *in fine* to slightly different time delay distributions.

These modifications mostly occur at high energies which are now almost completely suppressed by the EBL absorption, but it also modifies the lower energy domain. Such discrepancies can be seen in Figure 5.3 where the time delay distributions for the three illustration cases with redshift $z = 1$ (orange) are compared to the ones with the reference redshift $z = 0.03$ (black). While a large redshift simply eliminates information at VHE and thus removes the data points, the regime and shape of the distributions are conserved.

The corresponding euclidian distance functions are also shown in Figure 5.3 (same colour code) and better characterise these differences. The minimum is sensibly shifted with k_{min} tending towards lower values for large redshift. This is due to the missing data points at very high energies that change the variation amplitude combined with a larger zero-padding area and lead to euclidian distance curves rising at smaller k values. For large z the euclidian distance function requires observational data with high sensitivity at TeV energies to be relevant. The time delay distributions at low and high redshift behave in the same way and do not diverge much from one another. We can therefore use the information from data sets generated with a small redshift to extrapolate and recover time delays at very high energies for sources at large z. It is then also possible to reproduce inverse Compton time delays from synchrotron time delays for sources at large redshift with this circumventing method when sensitivity is lacking.

As was expected from the pure SSC scenario, a strong similarity arises between observables in the synchrotron and inverse Compton domains despite the EBL and Klein-Nishina effects that tend to suppress the highest energies. The closer to zero the value of $d_{E,\text{min}}$, the stronger the similarity between the two domains. Therefore, *this study of euclidian distance may help us build a predicting tool.* A tool allowing us to predict intrinsic delays in the gamma-ray energies from prior knowledge (e.g. observed data) on delays in the X-ray energies. It is however not possible to estimate an absolute degree of similarity based on this tool, but rather a relative one. Considering two data sets, labeled 1 and 2, that are characterised by euclidian distances such that $d^1_{E,\text{min}} < d^2_{E,\text{min}}$, this inequality indicates the domains in set 2 are more correlated than that of set 1. This relative notion will nonetheless allow us to establish a threshold on the euclidian distance and hint at the nature of the observed delays as will be discussed in Section 5.2.1.

5.1.1.2 Dependency on model parameters

The next step is to study the impact of the model parameters on distance functions. We already illustrated how they can modify the minimum euclidian distance $d_{E,\text{min}}$ as delays are amplified. We can imagine they could also shift the position k_{min} of this minimum. But first, let us comment on the transition gap between the synchrotron and inverse Compton domains.

Transition gap

We attempt to explain the transition gap appearing between the two domains of delays (see Figure 5.1) with a back-of-the-envelope calculation. The length of a flare is directly induced by the SED flux variation over time: the faster the variation in the SED, the shorter the flare.

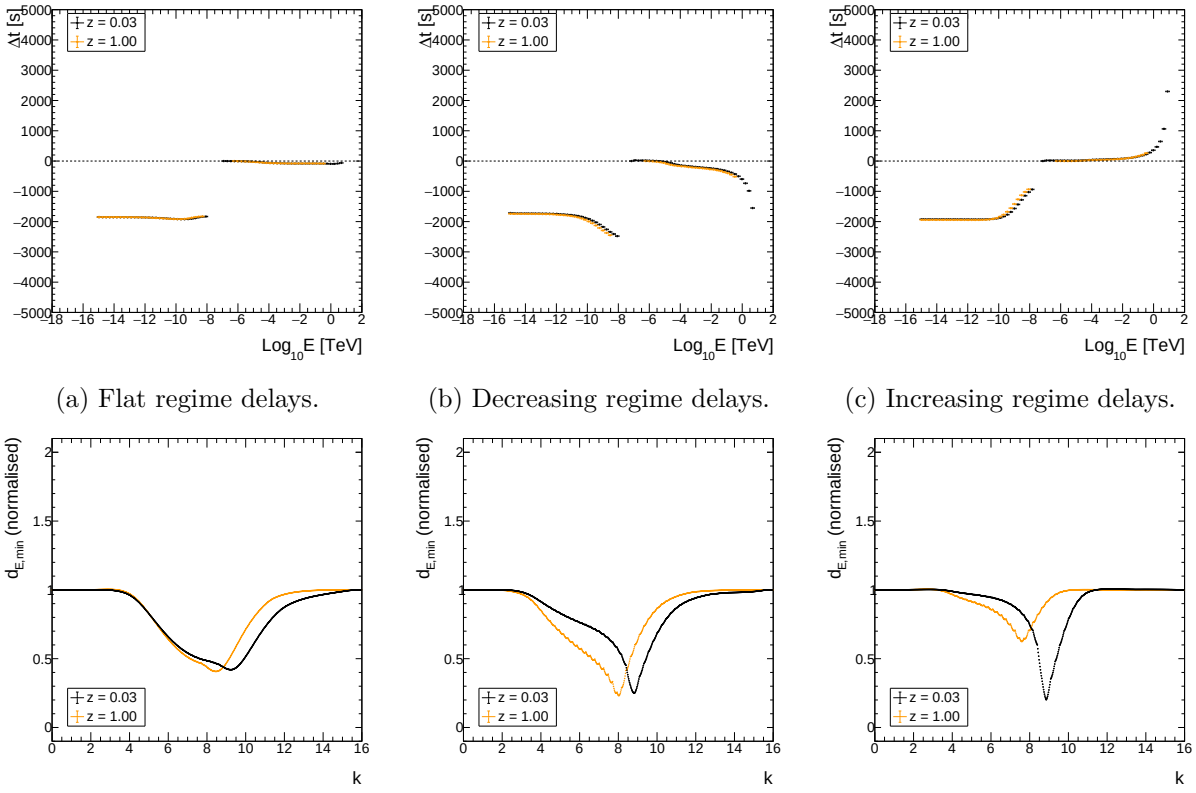

(a) Flat regime delays.

(b) Decreasing regime delays.

(c) Increasing regime delays.

(d) Flat regime euclidian distance.

(e) Decreasing regime euclidian distance.

(f) Increasing regime euclidian distance.

Figure 5.3: Time delays and corresponding euclidian distance functions between delays from the synchrotron and inverse Compton domains obtained for small ($z = 0.03$, reference, black) and large redshift ($z = 1$, orange) for the three illustrative cases. At large redshift, high energies are suppressed resulting in significantly modified euclidian distance function and minimum coordinates.

While the synchrotron emissivity given in Equation 2.15 involves a linear contribution from the lepton number density $N^*(t, \gamma)$, the inverse Compton emissitivity given in Equation 2.25 involves both the lepton number density and the synchrotron field (itself proportional to the lepton number density) leading to a quadratic contribution. The two SED bumps then evolve at different "speeds" and the variation in SEDs flux over time is linked to the lepton number density, thus to the bulk's radius evolution parameter m_r:

$$\Delta F_{sed,syn} \propto \Delta t^{-3m_r}, \tag{5.3}$$

$$\Delta F_{sed,IC} \propto \Delta t^{-6m_r}. \tag{5.4}$$

The evolution of the gap for various m_r values can be found in Figure 5.4. For $m_r \sim 1$ both bumps seem to vary at a similar pace such that light curves in the synchrotron and inverse Compton domains peak in the same time window. The gap between synchrotron and inverse Compton delays is then reduced to a minimum. As m_r value shifts away from 1, the variations

in SED synchrotron and inverse Compton fluxes become distinctive. For $m_r < 1$, ΔF_{sed} gets smaller resulting in longer flares. As the shift variation is more pronounced for the inverse Compton domain than the synchrotron one, the light curves in the inverse Compton domain will be the longest leading to larger Δt_E: $\Delta t_{syn} < \Delta t_{IC}$. Conversely, for $m_r > 1$, ΔF_{sed} gets larger resulting in shorter flares, the inverse Compton ones being shorter than the synchrotron ones for the same reasons finally leading to $\Delta t_{syn} > \Delta t_{IC}$.

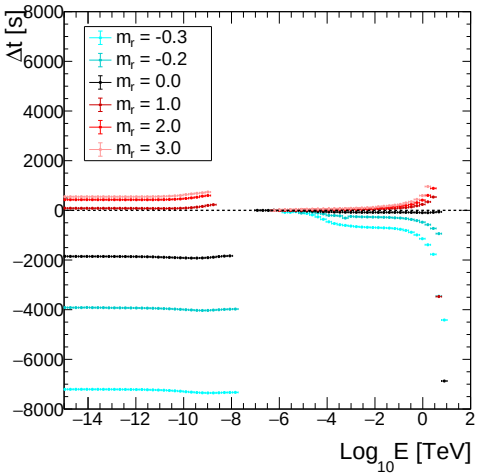

Figure 5.4: Evolution of the transition gap between synchrotron and inverse Compton domain time delays, governed by the bulk's radius time evolution.

Let us also comment on the difference in behaviour observed between the synchrotron and inverse Compton domains for cases with $m_r < 0$ (one is flat while the other is clearly decreasing). We defined the lepton number such that it stays constant throughout the bulk's evolution. Having $m_r \neq 0$ means only the lepton density is modified due to the change in volume of the bulk. However, the synchrotron emission is governed by the lepton number density such that varying m_r should not modify the synchrotron spectrum[1] and thus synchrotron time delays are unchanged. On the other hand, the inverse Compton emission strongly depends on the lepton density such that varying m_r deeply modifies the inverse Compton spectrum and affects the inverse Compton time delays, especially when it comes to adiabatic compression. It therefore appears that adiabatic processes, and in particular compression effects, tend to decorrelate intrinsic time delays, and we can no longer make the assumption of a pure SSC scenario.

The minimum of euclidian distance coordinates $d_{E,\min}$ and $k_{\min}$

To track the evolution of its minimum, we computed the enclidian distance for all sets of delays shown in Figure 4.5. The minimum coordinates $d_{E,\min}$ and $k_{\min}$ are plotted as a function of each one of the model parameters resulting in the diagrams shown in Figure 5.5. From this reprensentation we can assess the following:

- the optimal displacement is always such that $8 < k_{min} < 10$;

[1] In practice this in not entirely true. For instance, in the case where the magnetic field is frozen within the plasma, a variation in the bulk's radius will induce a variation in the magnetic field strenght and therefore modify the synchrotron spectrum. Such effects are however not taken into account in this model such that we can assume m_r does not modify the synchrotron spectrum.

- the minimum euclidian distance is always such that $d_{E,min} < 0.6$, and reaches this maximum when delays are following a flat trend.

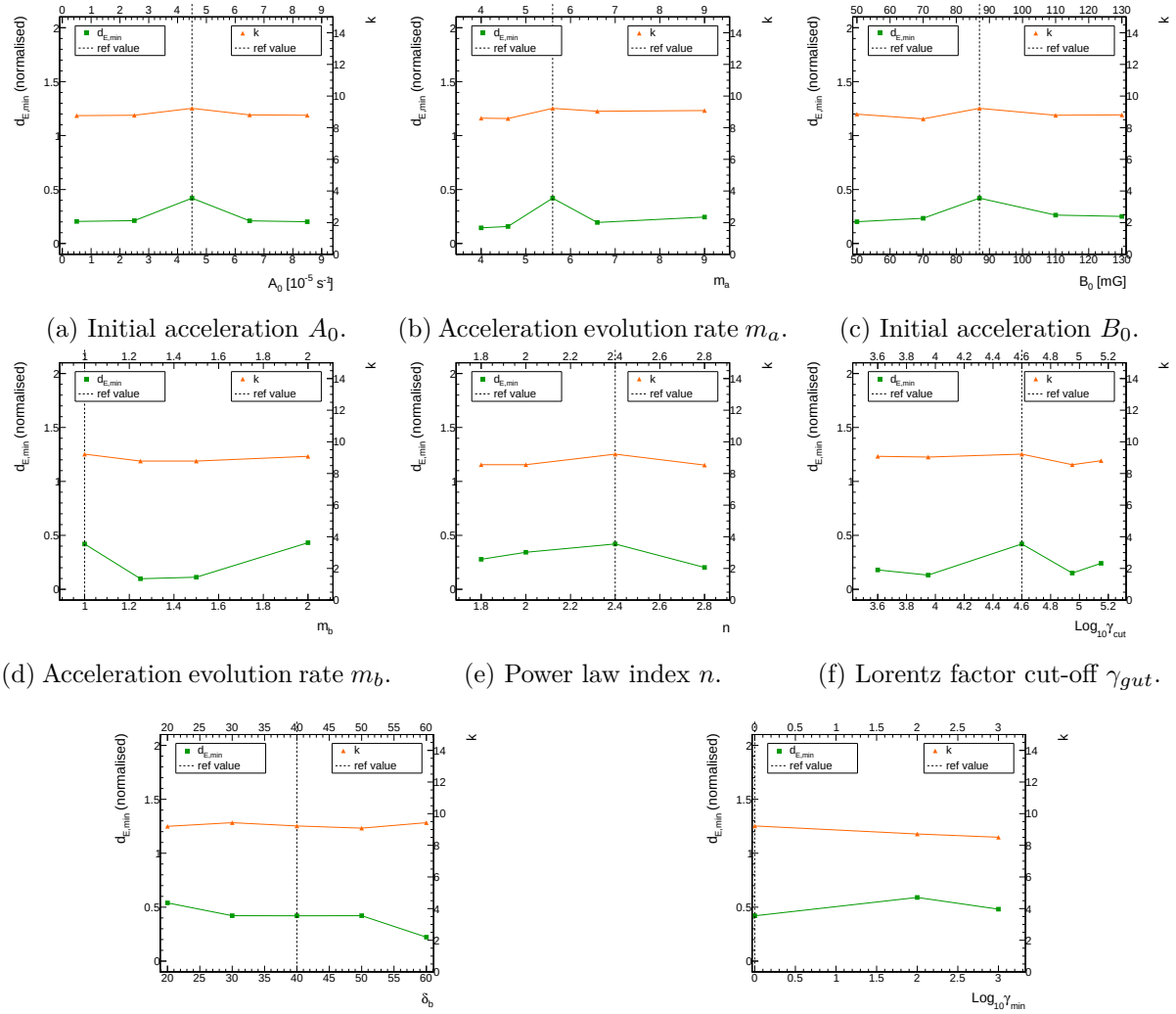

(a) Initial acceleration A_0. (b) Acceleration evolution rate m_a. (c) Initial acceleration B_0.

(d) Acceleration evolution rate m_b. (e) Power law index n. (f) Lorentz factor cut-off γ_{gut}.

(g) Doppler factor δ_b. (h) Minimum Lorentz factor cut-off γ_{min}.

Figure 5.5: Minimum euclidian distance $d_{E,\text{min}}$ and optimal displacement k_{min} evolution with respect to various model parameters. The dashed line indicates the parameter reference value (overlapping with the left vertical axis in Figure (h)). From these diagrams we get $8 < d_{E,\text{min}} < 10$ and $k_{\text{min}} < 0.6$.

5.1.2 Hysteresis study: a sensitive tool

So far we focused exclusively on time delays as this is the quantity of interest for our LIV framework. However, the similarity between synchrotron and inverse Compton domains can also be quantified directly from SEDs. Hardness-intensity diagrams (HID) showing the SED index (hardness) against the SED flux (intensity) can give rise to hysteresis patterns. Such patterns have been found in observed data (e.g. [81, 82, 83]) and simulated with AGN models (e.g. [84]),

and ultimately help to constrain emission scenarii.

To produce such diagrams, we compute the hardness over a small energy window in both synchrotron and inverse Compton bumps which needs to be the same for all SEDs. We want the inverse Compton window to be at energies as high as possible. The intensity plotted in the diagram is taken as the mean flux within the energy window. We want this window to be relatively small for the intensity to vary as little as possible. Finally, we want the window not to overlap with bumps' maxima to prevent a change of sign in spectral indices. We thus choose to define the inverse Compton window lower boundary as the position of the peak at highest energies (i.e. far right inverse Compton bump peak) and spread the window over 1 decade in energy to the right hand side. The synchrotron counterpart is chosen the same way. Ultimately, we focus here on narrow windows in the X-ray and gamma-ray energy domains.

The resulting hysteresis pattern for the three illustration cases with flat, decreasing and increasing regimes can be found in Figure 5.6. We can make several observations here.

- The X-ray domain hysteresis loop is much wider than the gamma-ray one. This is expected as the flux amplitude variation in the SED is more important in the synchrotron domain than in the inverse Compton one.
- Hysteresis patterns are the same for both domains: X-ray and gamma-ray hysteresis always follow the same loop orientation. This is again expected as the inverse Compton bump is closely related to the synchrotron bump.
- The loop orientation changes according to the delays regime:
  - flat regime $\Longleftrightarrow$ "flat" hysteresis;
  - decreasing regime $\Longleftrightarrow$ clockwise hysteresis;
  - increasing regime $\Longleftrightarrow$ counter-clockwise hysteresis.

  As both SEDs and lightcurves are closely related, we also expected hysteresis patterns and time delays to be related.

The detailed hysteresis pattern likely depends on the nature of the flare. Our approach, which involves a simple and standard flare generation, still appears to provide a general description of the dominant trends that could be observed. From the third item, observing non-flat hysteresis in data means there also should be non-zero intrinsic time delays in the pure SSC scenario. Adding to that the second item, one only needs to have information on the X-ray domain hysteresis to predict the existence or not of gamma-ray domain intrinsic time delays. In order to go further, we would need to develop a tool to quantify the relationship existing between hysteresis and intrinsic time delays. Ultimately, this tool can be used to resolve the existence of intrinsic time delays even though none is detected due to a lack of precision or because another phenomenon (such as LIV effects) contributes to cancelling them out.

5.2 LIV injection

Now that we have a much more detailed view on intrinsic time delays and built useful tools, we can introduce LIV effects and push this study to its final stage: find a way to discriminate

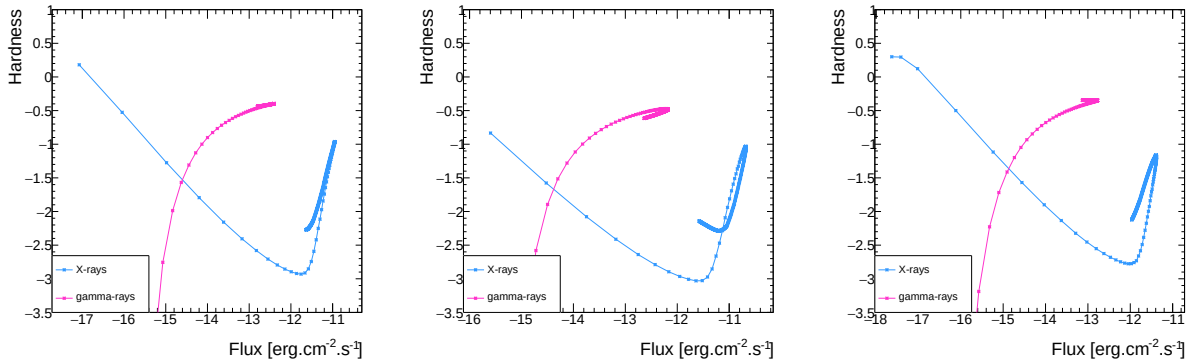

(a) Flat regime, no loop orientation ("flat" hysteresis).

(b) Decreasing regime, clockwise.

(c) Increasing regime, counterclockwise.

Figure 5.6: Hardness-intensity diagrams (HID) highlighting hysteresis patterns for X-ray (blue) and gamma-ray (magenta) domains.

between intrinsic and LIV-induced time delays. Besides fundamental physics, LIV effects are only dependent on the distance of the source, and not on its specific emission mechanisms. The simplest way to account for them is then to shift light curves by a quantity dependent on their energy. This quantity will then be specific to each light curve, shifting each point by a constant value:

$$F_{E_{LC}}(t) \longrightarrow F_{E_{LC}}(t + \tau_n E_{LC}^n), \tag{5.5}$$

where E_{LC} is the mean value of the energy band on which a light curve is defined, n is the LIV correction order and τ_n is the LIV term. τ_n is kept as a free parameter expressed in s/TeV^n and can take positive (subluminlal effect) or negative (superluminal effect) values. As a consequence, there is no peak deformation. For the sake of illustration, we will only consider cases for the linear case with $n = 1$. Considering the way it is incorporated to the existing light curves, the quadratic case with $n = 2$ would give similar results only with a different amplitude.

5.2.1 Impact on delays and euclidian distances

As time delays are extracted from light curves, they are now automatically accounting for both intrinsic and LIV effects simultaneously. As τ_n is a user defined free parameter, one simply needs to set $\tau_n = 0$ to revert back to previous sets of delays where only intrinsic effects were accounted for. Time delays and the corresponding distance functions for the three illustrative cases can be found in Figure 5.7. Intrinsic effects are shown in black, while intrinsic combined with LIV effects are shown in red for $\tau_n > 0$, and blue for $\tau_n < 0$. The τ_n values have been chosen based on the detectability study performed in Section 4.2.3 for the archetypal source Mkn 501 located at redshift $z = 0.03$.

As LIV contribution depends on energy, having $\tau_n > 0$ tends to send inverse Compton delays in the increasing regime while $\tau_n < 0$ send them in the decreasing one. Therefore, LIV either amplify time delays when both effects impose the same regime, or suppress time delays when the two effects impose opposite regimes. For τ_n big enough, LIV effects can even change the regime in the inverse Compton domain. In other words, LIV contribution tends to decorrelate synchrotron and inverse Compton sets of delays. As a consequence, the distance function minimum $d_{E,\min}$ shifts away from 0 as τ_n diverges from 0. As the method has a fairly poor sensitivity

when it comes to small changes in time delays, the introduction of LIV may leave the minimum distance unchanged. Nevertheless, as the introduction of LIV or any other external effect tends to decorrelate the time delays, it will always yield either equal or larger values of $d_{E,\min}$.

Contrary to cases with intrinsic effects only, we cannot use the euclidian distance to accurately reconstruct or even predict inverse Compton time delays from synchrotron ones when LIV effects are introduced. This is due to the poor correlation and lack of sensitivity. Furthermore, the optimal diplacement $k_{\min}$ can be modified as a consequence of highly decorrelated sets. Finally, for an intermediate value of τ_n where the competition between LIV and intrinsic effects result in delays both increasing and decreasing consecutively within a given energy domain, a second peak can appear (see for example the case for $\tau_1 = 200$ s/TeV in Figures 5.7c and 5.7f).

However as was pointed out earlier, the minimum normalised euclidian distance does not fall below $d_{E,th} = 0.6$. *If the minimum distance cannot fall below this threshold, it hints at another effect being at play and time delays can no longer be explained by intrinsic effects from the pure SSC model only.*

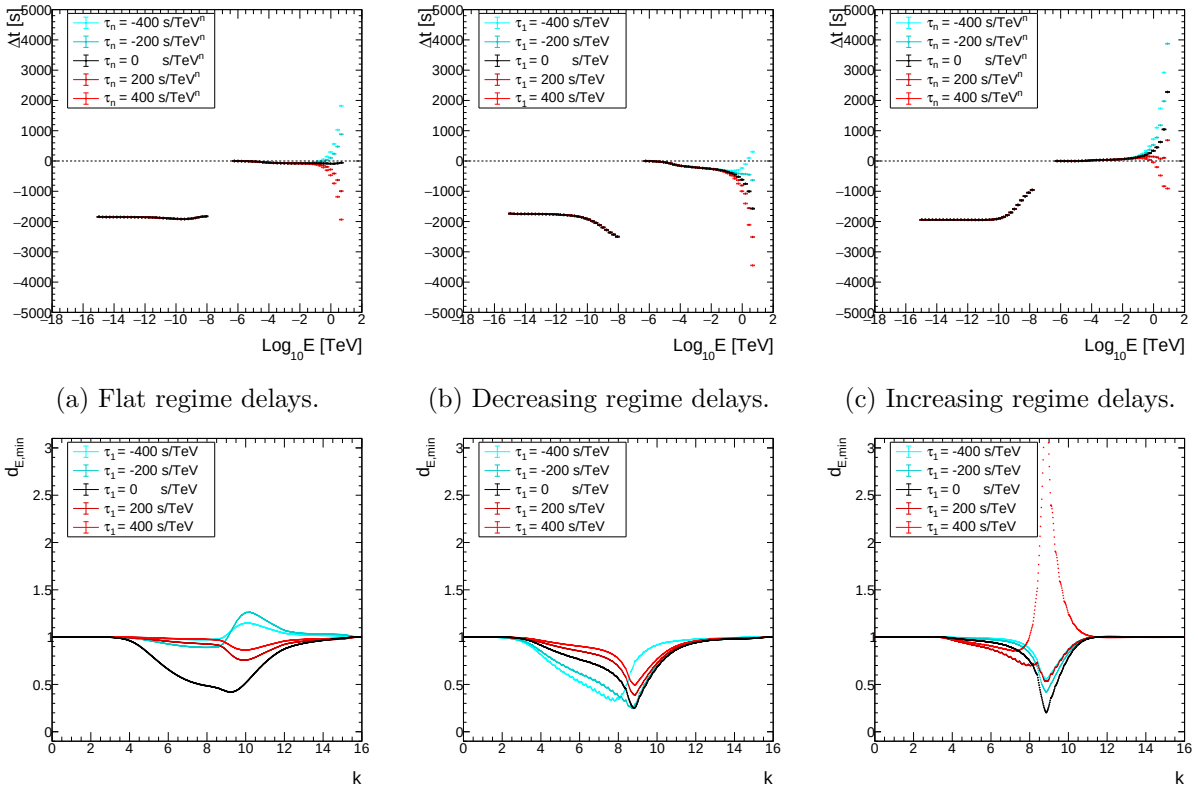

(a) Flat regime delays.

(b) Decreasing regime delays.

(c) Increasing regime delays.

(d) Flat regime euclidian distance.

(e) Decreasing regime euclidian distance.

(f) Increasing regime euclidian distance.

Figure 5.7: Time delays and euclidian distance function computed for the three illustrative cases with various LIV contributions. The minimum euclidian distance $d_{E,\min}$ is always reached by the curve with no LIV effect (black).

5.2.2 Impact on hysteresis

To build hardness-intensity diagrams accounting for LIV effects, we first need to rebuild SEDs from LIV-shifted light curves. This can be done by applying a transformation opposite to the one of Equation 4.23:

$$F_{SED}(\nu_{\rm obs}, t) = \int_{\nu_{\rm min}}^{\nu_{\rm max}} d\nu_{\rm obs}^{-1}\, F_{LC}(\nu_{\rm obs}, t)\nu_{\rm obs}. \tag{5.6}$$

Contrary to time delays, LIV contribution to SEDs is barely noticeable. However, as hysteresis patterns are very sensitive to any variation in SEDs, this modification can be highlighted through hardness-intensity diagrams. Figure 5.8 illustrates this statement with the evolution of the gamma-ray hysteresis pattern for the three regimes at various τ_n. At low flux the hardness is greatly affected leading to dramatically different values, and slowly converges as the flux increases where hysteresis patterns overlap. Now we want to resolve the pattern at high flux. The hysteresis for X-ray energies (blue) is unaffected by LIV as could have been expected. Remembering hysteresis in the X-rays and gamma-rays systematically loop in the same orientation when only intrinsic effects are considered, we can use the X-ray hysteresis as reference. Looking at gamma-ray hysteresis, we can make the following correspondence:

- $\tau_n > 0 \Longleftrightarrow$ clockwise orientation ($\Longleftrightarrow$ increasing delays);
- $\tau_n < 0 \Longleftrightarrow$ counter-clockwise orientation ($\Longleftrightarrow$ decreasing delays).

Note that $\tau_n > 0$ accounts for subluminal LIV effects and $\tau_n < 0$ for superluminal ones. Similarly to time delays, when τ_n is large enough, it can cause hysteresis to change orientation. As a consequence, *observing a difference of looping orientation between the X-ray and gamma-ray hysteresis patterns strongly hints at a contribution other than intrinsic effects being at play.*

5.3 LIV-modified EBL absorption: extreme scenarii

All the above results as well as the ones from Chapter 4 have been derived taking into account a standard model of EBL absorption. However, as was discussed in Section 1.3.2, LIV effects are predicted to modify the EBL absorption as shown in Figure 1.2 for redshift $z = 0$. Fairbairn et al. [85], provided an estimation of the arrival probability of photons emitted by a source at redshift $z = 0.5$ as well as the expected spectrum of Markarian 501 blazar ($z = 0.03$) for different values of the quantum gravity energy scale E_{QG} (noted M_{LV} in Figure 5.9). All these figures indicate the EBL becomes more transparent as E_{QG} gets smaller: LIV effects tend to cancel the EBL absorption.

While the extreme case where $E_{QG} = \infty$ corresponds to scenarii with the standard EBL we have studied before, the opposite extreme scenario where LIV effects completely cancel the EBL absorption can be approximated by ignoring the EBL contribution. We have previously discussed the impact of the EBL on intrinsic time delays: it eliminates high energy information while the distributions behaviour is preserved and almost unchanged. We expect to draw the same conclusions for time delays including LIV effects. A quantified variation between delays computed with and without EBL correction for the three regimes with various LIV contributions can be found in Figure 5.10. The variation amounts to less than 5% whichever the case such that time delays behaviour should not be significantly affected by a LIV-modified EBL absorption, even if it will certainly modify the threshold at which high energy can be observed. Note that

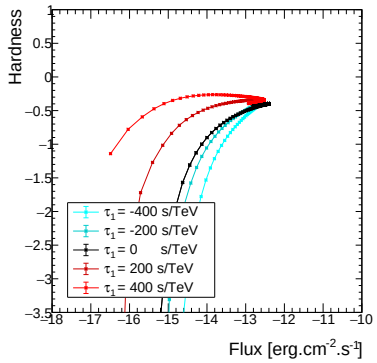

(a) Flat regime.

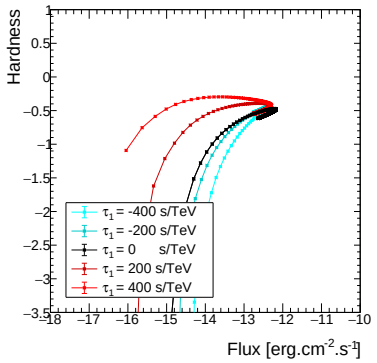

(b) Decreasing regime.

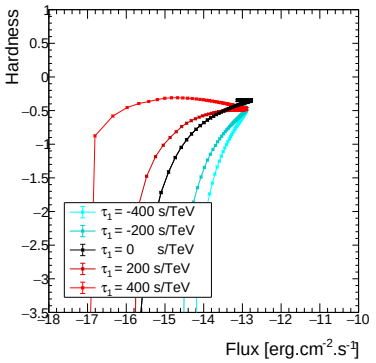

(c) Increasing regime.

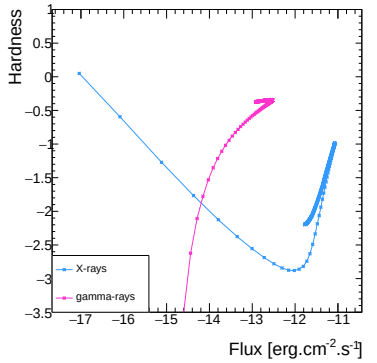

(d) Flat regime for $\tau_1 = 400$ s/TeV.

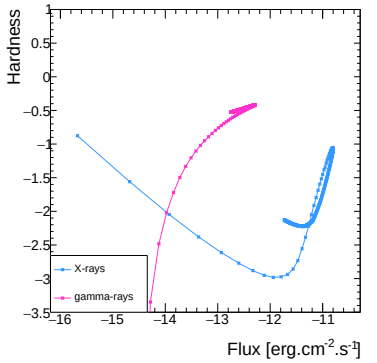

(e) Decreasing regime for $\tau_1 = 400$ s/TeV.

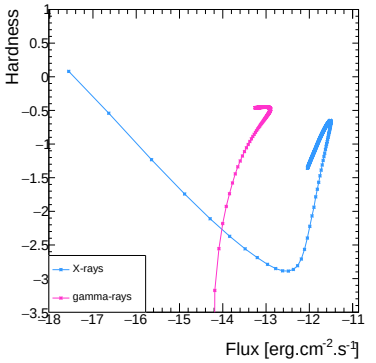

(f) Increasing regime for $\tau_1 = 400$ s/TeV.

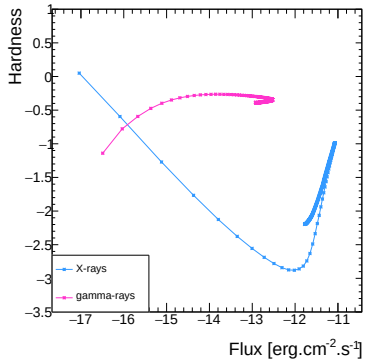

(g) Flat regime for $\tau_1 = -400$ s/TeV.

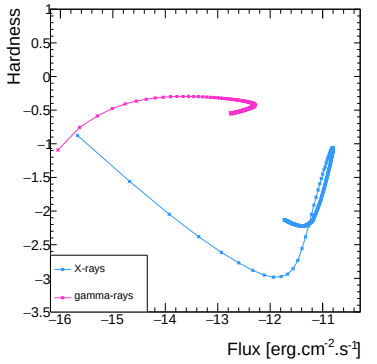

(h) Decreasing regime for $\tau_1 = -400$ s/TeV.

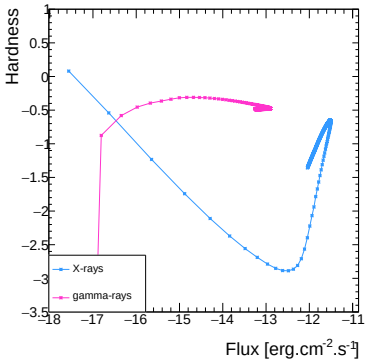

(i) Increasing regime for $\tau_1 = -400$ s/TeV.

Figure 5.8: Hardness-intensity diagrams evolution for the three illustrative cases with various LIV contribution showing LIV effects can cause a change in loop orientation in the gamma-ray domain. Figures (a) to (c) show the gamma-ray hysteresis pattern for various LIV contributions. Figures (d) to (i) compare X-ray and gamma-ray hysteresis patterns for positive and negative LIV contribution. While the X-ray hysteresis pattern is left unchanged, a rotation pattern appears in the gamma-ray one (either clockwise or counter-clockwise depending on τ_n sign).

this is an strong oversimplification, and this study would greatly benefit from properly taking into account the predicted EBL absorptions shown in Figure 5.9.

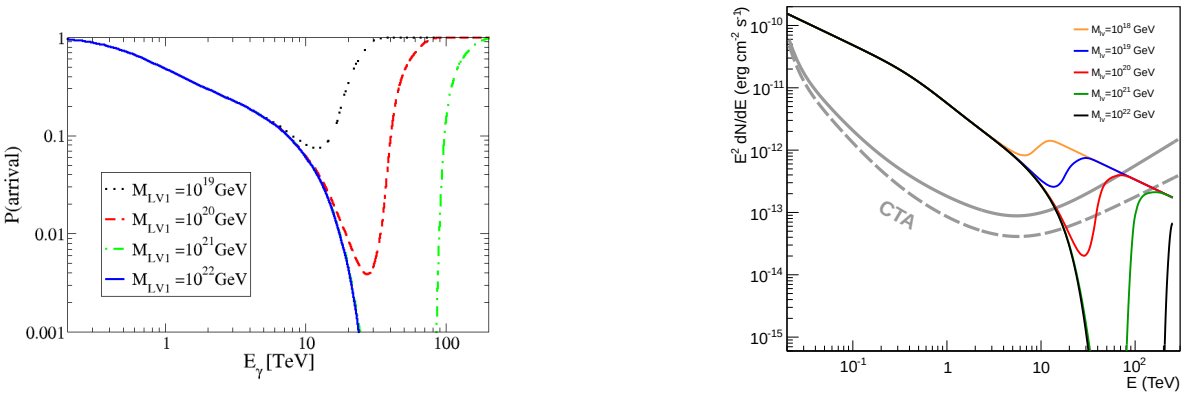

(a) Photons arrival probability for a source at $z = 0.5$.

(b) Expected spectra for Markarian 501 blazar.

Figure 5.9: Consequence of LIV-modified EBL for various $M_{LV}(= E_{QG})$ values (both plots are taken from Fairbairn et al. [85]).

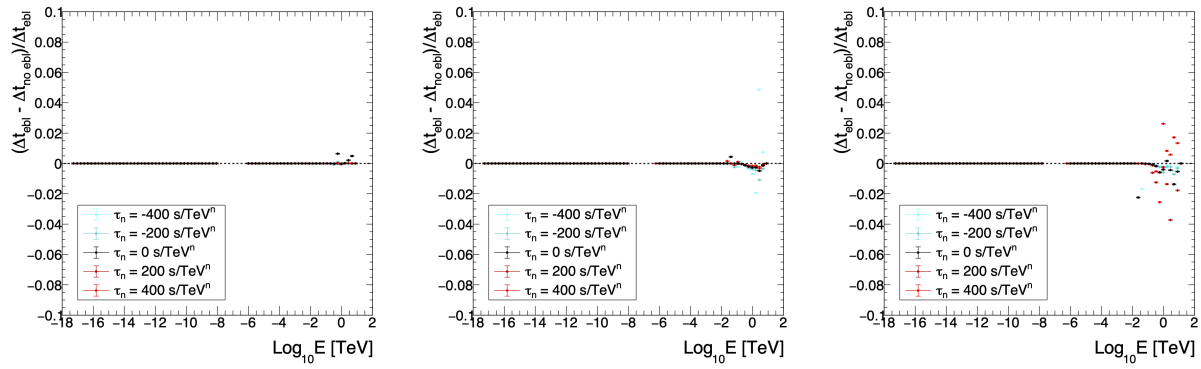

(a) Flat regime.

(b) Decreasing regime.

(c) Increasing regime.

Figure 5.10: Variation of time delays with extreme cases of EBL models (standard model or no EBL) for the three regimes and various LIV contributions. Time delays obtained with the two EBL models undergo a variation of maximum 5%.

5.4 Observational perspectives

From the results derived in this chapter we can draw several conclusions.

We have found that time delays arising from the synchrotron processes are strongly correlated to the ones arising from the inverse Compton processes when considering pure SSC models. When time delays present strong variations, the minimum of the euclidian distance function indicates the optimal displacement $k_{\min}$ to apply to one set of delays to reproduce the other set. The accuracy on the reproduction is then indicated by the minimal distance $d_{E,\min}$. As we generally lack information on the highest energies due to the EBL absorption and Klein-Nishina effects, this can be used as a tool to predict the intrinsic time delays in the gamma-ray domain with the knowledge we get from observing time delays in the X-ray domain. However, this is only true for the pure one-zone SSC scenario. Introducing external or adiabatic processes tends

to weaken this symmetry and hinders the reconstruction. When placed in the right conditions and assumptions, the presence of such a symmetry could help validate the pure one-zone SSC scenario.

We have further confirmed the break of symmetry between the synchrotron and inverse Compton domains when introducing LIV effects in our simulations. This asymmetry can however be used to our advantage. Indeed in the eventuality where the pure one-zone SSC scenario is validated with other observables, a break of this symmetry would hint that another effect is at play and contributes to modify the time delays. In particular, it becomes very useful when this effect contributes to only one or the other energy domain. In the case where instruments sensitivity allows it, this can also be further confirmed with the study of hysteresis where a similar break of symmetry should arise. As the EBL absorption (LIV-modified or not) and Klein-Nishina effects do not break such symmetry, we should be able to quantify the discrepancies and discriminate between intrinsic and LIV contributions to the observed time delays.

Let us add that a prediction of the detectability of time delays and hysteresis patterns with CTA instruments was deemed premature for the work presented in this manuscript, but it is indeed an important and planned perspective for the near future.

Part III

Preparation for population studies with VHE data

Chapter 6

Searches for Lorentz invariance violation signatures with time of flight studies

Contents

In this chapter we provide an overview of the current state of the art for LIV time-of-flight studies. We first present and compare the analysis methods developed and used so far, then summarise the main results obtained with these methods and assess their performances for LIV studies.

6.1 Analysis methods

Time of flight studies for LIV searches started in 1996 with the Whipple[1] and EGRET[2] experiments, and continued with next generation experiments including H.E.S.S., MAGIC, VERITAS and *Fermi*-LAT amongst others. During the past 25 years, many analyses methods have been developed to look for time delays arising in light curves of various types of sources. In this section, we review and briefly explain the underlying principle behind these methods. We distinguish two general approaches. One of them relies on finding the LIV term that best cancels the propagation effects and transforms back the observed data to a non time-shifted form. The other approach relies on comparing the approximated LIV-free emission with the observed LIV-modified data and estimate the time delay that separates the two of them. The former makes use of a single data set while the latter requires two distinct data sets.

6.1.1 Single data set transformation

The acronyms introduced in this section will be extensively used in the rest of this chapter, for the mthod comparison and the discussion on results.

Energy cost function (ECF)

The energy cost function uses the fact that a signal pulse propagating through a dispersive medium - the dispersion being caused by LIV effects - will be diluted [88]. As a consequence, its power, i.e. the total energy per unit time, decreases as photons propagate through the medium. The original power of the pulse can be recovered when applying a transformation that reproduces the undispersed signal - i.e. the signal that would have been detected if there was no LIV effect. The power of the pulse would then be maximised with this specific transformation.

The transformation is applied to a data sample representing the most active part of the flare - i.e. the part that differs the most from a uniform distribution. The data sample is therefore defined by a specific time window within the light curve, between time stamps noted t_1 and t_2. Each photon i in the sample is characterised by an arrival time t_i and an energy E_i. The transformation consists in applying a time shift $\Delta t = \pm\tau_n E^n$ to each photon where τ_n is the LIV modifying term at order n (either linear for $n=1$, or quadratic for $n=2$), that should cancel out the propagation effect. With such a transformation, some photons are bound to end up outside of the time window, while some others would enter it. The power of the signal is computed as the sum of the energies of all the photons within the time window divided by the duration of the time window:

$$P = \sum_i \frac{E_i}{t_2 - t_1}, \tag{6.1}$$

[1] In operation between 1968 and 2013, it was the first Earth-based instrument to detect TeV gamma-ray sources with the Crab Nebula [86] and the AGN Mkn 421 [87].

[2] In operation between 1991 and 2000.

for many values of τ_n. The energy cost function is then defined as the power P as function of τ_n, and the position of its maximum gives the value of τ_n that best recovers the undispersed signal.

Dispersion cancelation (DisCan) and sharpness maximisation method (SMM)

The dispersion cancelation [89] and sharpness maximisation [90] methods both make use of the dispersion of the signal pulse. They use cost functions to measure the sharpness of binned light curves which is expected to reduce as the pulse is diluted. The main difference between these two methods lies in the way the sharpness is measured, i.e. which cost function is used. Shannon, Renyi and Fisher information, but also the variance, total variation or self-entropy have been tested with the DisCan method [90]. The authors concluded Shannon information yielded the best results out of all the other cost functions. The SMM method makes use of another cost function similar to the Shannon information and describes the sharpness S as

$$S(\tau_n) = \sum_{i}^{N-\rho} \log\left[\frac{\rho}{(t_{i+\rho} - t_i)}\right], \tag{6.2}$$

with ρ a parameter used to avoid $t_{i+\rho} - t_i \ll 1$ for which the function would start to diverge. The τ_n that maximises the sharpness function then corresponds to the most probable LIV effect.

PairView (PV)

The PairView method computes the energy-dependent time delay

$$\tau_n \equiv \frac{t_i - t_j}{E_i^n - E_j^n} \tag{6.3}$$

between the arrival times t for each pair of photons $(i,j)_{i>j}$ with energies (E_i, E_j). The distribution of τ_n is then expected to peak for the most probable value of τ_n.

6.1.2 Comparison between data subsets

The methods listed here rely on the comparison between two sets of data. Since we look for delays between arrival times of photons with different energies, the observed data set is separated in two photon lists, one gathering the low energy photons while the other gathers the high energy ones. Two distributions are then created from these two subsets. In some cases the reduced data needs to be compared with the intrinsic (i.e. LIV-free) emission. Although the source emission mechanisms have been described and modeled with increasing accuracy, there is no consensus yet and intrinsic emissions cannot be reconstructed or simulated with a high enough precision as of now. The low energy light curve where LIV effects are supposed to be small is then used to approach a LIV-free template needed for some methods.

Band comparison (BC)

The band comparison which was introduced by the Whipple collaboration is a fairly simple approach where the low and high energy lightcurves are subdivided into time bins. A likelihood-ratio test[3] is used to compare the contents of the time bins in the two light curves [91]. This technique allows to estimate the probability of observing concurrent peaks in the two light curves

[3] Not to be confused with the maximum likelihood method we introduce later on.

and the time delay Δt separating them. The precision of the method largely relies on the choice of the binning, and loses sensitivity for small Δt.

Peak Comparison (PC)

The peak comparison method simply consists in comparing the peak position between the low and high energy light curves and estimating the time delay Δt separating them [92]. The main difference with the above method is that PC focuses on peaks while BC compares bins information regardless of the presence or not of a peak. For such a method to be efficient, an immense precision on the light curve is required so it is usually applied to millisecond pulsars data only. Thanks to the stability of their emission, pulsars can be observed over long periods of time and the data can be cumulated. As a consequence, the data sets have great statistics and the light curve shapes are especially well-defined. The precision on detected time delays is then directly dependent on the duration of observation of pulsars.

Modified cross-correlation function (MCCF)

The cross correlation function is widely used in signal processing for the measurement of similarity and pattern recognition between two time series. The correlation coefficient is computed as a function of the displacement Δt of one series relative to the other. The two series best match when this coefficient is maximised, the position of the CCF maximum giving the delay Δt separating the two time series. The LIV effect is then estimated by using $\Delta t = \pm\tau_n E^n$. However this method only works under certain requirements such as uniformly sampled data (binned with a constant δt) or having the same number of data points. For the method to be sensitive enough to LIV studies, the light curve resolution (i.e. the bin width δt) needs to be smaller than the timescale Δt under study, yet another requirement which is not necessarily fulfilled. Modified cross-correlation functions (MCCF) have been created to bypass one or more of these constrains. The MCCF presented in [93] - originally developed for a timescale analysis of spectral lags - makes possible the search for time delays shorter than the light curve temporal binning by introducing standard deviation terms in the CCF formula.

Wavelet transform (WT)

The wavelet transform [94] relies on the definition of wavelets which are wave-like oscillation localised in time and defined by their scale (stretch) and location (position in time). A wavelet transform is used to decompose a function into a set of wavelets, much like it is done with a Fourier transform. It gives partial information on both the temporal extent and the frequency spectrum of the signal based on the uncertainty principle of signal processing

$$\Delta t \Delta\omega \geq 1/2, \tag{6.4}$$

where t represents the time and $\omega = 2\pi\nu$ the angular frequency. Wavelet transforms thus allow to estimate that the initial function includes a signal of an approximate frequency that happened in a given time window. The higher the resolution on one component, the lower the resolution on the other component.

A wavelet transform can either be discrete (DWT) or continuous (CWT). While the former is usually used for noise reduction as it removes fluctuations, the latter is used to localise extrema in the signal. Wavelets are used to pin point the flare or peaked emission, as opposed to the

source quiescent state or surrounding emission. A CWT is applied to both low and high energy light curves which are then identified by a set of extrema. The low energy extrema are coupled with the high energy ones to form pairs. The separation between the two extrema in each pair i then provides a set of time delays Δt_i, used to estimate the mean lag Δt separating the low and high energy light curves [95]. The LIV study is then performed separately.

Maximum likelihood (ML)

The maximum likelihood method roughly corresponds to an unbinned version of the band comparison method. For this technique we want to compare the observed data with the unaltered (LIV-free) emission intrinsic to the source which is approximated with the low energy light curve [96]. From the fitting of the low energy data set, parameterisations of the temporal and energy distributions are created leading to a set of parameters θ. A transformation using the LIV corrective term τ_n is applied to the approached LIV-free intrinsic emission in order to recover the high energy data sets. The likelihood is maximised for the τ_n that best recovers the low energy distributions.

The ML method makes use of a profile likelihood test $L_p(\tau_n) = \sup_{\tau_n} \mathcal{L}(\tau_n, \vec{\theta})$ where τ_n is the parameter of interest, and $\vec{\theta}$ is a vector of nuisance parameters. L_p is obtained with the values of θ that maximise the likelihood $\mathcal{L}$ for a given τ_n. $\mathcal{L}$ can be built with a probability density function (PDF) that describes the probability P to detect a gamma-ray i with a given measured energy E_i at a given time t_i such that

$$\mathcal{L}(\tau_n, \vec{\theta}) = \prod_i \frac{dP}{dE_i dt_i}. \tag{6.5}$$

In its simplest form, this probability is a function of time and energy obtained from the normalised convolution between the transformed light curve $C(t_i - \tau_n E_i^n)$ and energy spectrum $\Gamma(E_i)$ parameterisations. The need for a fit introduces approximations which constitute the main drawback of this method and its primary source of uncertainty. A better understanding and modeling of the source intrinsic emission could however solve this issue.

6.1.3 Strengths and limitations

Although we have distinguished the methods by having to rely on either a unique data set or compare two subsets, we could have arranged them in other categories: binned and unbinned methods. While we expect binned methods to be faster and easier to process, there is an unavoidable loss of information in the process. Indeed, the precision achievable in these cases is heavily dependent on the way the observables are binned. A careful optimisation needs to be performed in order to bring out the most out of these methods. Furthermore, they are not well adapted to low statistics data sets as it requires a coarser binning and deteriorates the results precision. As a consequence, unbinned methods tend to be superior to binned ones. They are however more technical and less straightforward such that only three methods out of all the ones listed above - namely the ECF, PV and ML methods - work on individual photons.

The methods relying on single set transformation require data sets with a well-defined isolated peaked light curve. They are therefore especially fitting for the study of LIV with pulsars data. Indeed, even though most of the detected photons are background events, the periodicity of the signal allows for a compilation of observations resulting in data sets with exceptionnally

high statistics and clear-cut light curves. Transient objects on the other hand may show very low statistics but also several overlapping peaks in the light curve which greatly hinders the performance of such methods.

Meanwhile, the methods comparing two subsets of the data can treat all types of sources and light curve pattern more equally. Their performance is then highly dependent on the way the original set is separated. Ideally, the data sets should spread over a wide energy range in order to have a significantly different impact of LIV effects in the two subsets. This is especially true for the ML method which requires the low energy subset to approximate a LIV-free template light curve. The separation in subsets means light curves are built with only a fraction of an already low number of photons, and thus lose in definition or require a coarser binning than intended. Although the ML method is unbinned, the problem remains. As the LIV-free template is a function fitted on the low energy light curve, the low energy subset needs to have sufficient statistics for the light curve to be well-defined. Still, the ML method was created with the intent to be performant with low statstic data sets and yield reliable results regardless.

6.2 State of the art

6.2.1 Up-to-date limits

In the past decades, only a handful number of data sets detected by IACTs from GRBs, AGNs and pulsars alike could be used to test LIV models with time of flight studies. In contrast, satellite-embarked instruments could only resolve GRBs' variability but managed to gather several dozens of usable data sets. In this section, we briefly review the main milestones for time-of-flight LIV searches with both types of instruments.

The first test was performed on the AGN Mkn 421 data observed by the Whipple experiment using the BC method. It led to the first upper limit on the QG energy scale at linear correction $E_{QG,1} > 4 \times 10^{16}$ GeV [91]. Soon after, in 1999, the EGRET collaboration suggested for the first time to extend the study to pulsars. It was applied to the Crab pulsar which led to $E_{QG,1} > 0.18 \times 10^{16}$ GeV [97] which is significantly less constraining than the upper limit set by Whipple.

Nearly a decade later in 2005, two consecutive flaring episodes of the AGN Mkn 501 were detected by the MAGIC experiment, and analysed with the ECF method leading to upper limits for both linear and quadratic corrections: $E_{QG,1} > 0.21 \times 10^{18}$ GeV and $E_{QG,2} > 2.6 \times 10^{10}$ GeV [88]. This analysis uncovered the one and only significant time delay detected up to now with $\Delta t = 4 \pm 1$ min which was attributed to intrinsic effects by the authors [79]. Although Mkn 421 and Mkn 501 have a similar redshift ($z_{\text{Mkn421}} = 0.034$ and $z_{\text{Mkn501}} = 0.031$), the MAGIC analysis led to a limit on linear correction five times stronger than the one set by Whipple. However this difference could also be explained by the difference in energy range (up to $E_{\text{Mkn421}} = 2$ TeV and $E_{\text{Mkn501}} = 10$ TeV) or the number of signal events detected ($N_{\text{Mkn421}} \sim 170$ and $N_{\text{Mkn501}} \sim 1800$ events) such that comparing the efficiency of the two methods here is irrelevant.

Soon after, in 2006, a flaring episode of the AGN PKS 2155-304 was detected by the H.E.S.S. experiment and is still today the most variable flare ever detected at gamma-ray energies [98]. The data was analysed with the MCCF and WT methods which led respectively to $E_{QG,1} > 0.72 \times 10^{18}$ GeV and $E_{QG,1} > 0.52 \times 10^{18}$ GeV for the linear correction, and

$E_{QG,2} > 0.14 \times 10^{10}$ GeV for the quadratic correction obtained with the MCCF method only. Here the two methods are compared on the same data sets and provided consistent results such that they appeared to be equally performant.

The ML method [96] was introduced three years later in 2009 and was used to re-analyse both Mkn 501 and PKS 2155-304 data sets. This second analysis led to $E_{QG,1} > 0.30 \times 10^{18}$ GeV and $E_{QG,2} > 5.7 \times 10^{10}$ GeV for Mkn 501, which are consistent with the limits yielded by the ECF method. On the other hand, the second analysis for PKS 2155-304 led to $E_{QG,1} > 2.1 \times 10^{18}$ GeV and $E_{QG,2} > 6.4 \times 10^{10}$ GeV [99], which are this time significantly stronger than the ones provided by the MCCF and WT methods, indicating the effectiveness of the ML method.

A few years later, the VERITAS experiment performed an analysis on the Crab pulsar data collected between 2007 and 2011. For this analysis, both DisCan and PC methods were used which led to respectively $E_{QG,1} > 0.30 \times 10^{18}$ GeV and $E_{QG,1} > 0.19 \times 10^{18}$ GeV for the linear correction, and $E_{QG,2} > 0.70 \times 10^{10}$ GeV and $E_{QG,2} > 0.17 \times 10^{10}$ GeV for the quadratic ones [92]. For this DisCan method, the cost function was changed to a Fourier series estimator using the first m harmonics of the pulsar periodic signal. Both methods yielded consistent results with limits being significantly less constraining than the ones obtained with AGN data, similarly to the Whipple and EGRET analyses.

The ML technique quickly became the standard analysis method thanks to its precision and sensitivity. Although the ECF shows a similar performance, it requires to identify well-isolated flares. The DisCan method which should compare to the ECF is set aside for the same reasons. In contrast the ML is an unbinned method which can be applied to low statistic data sets and complex lightcurves harboring several overlapping flares. Later on, all the data sets coming from new detections were analysed with the ML method. This includes two flaring AGNs (PG 1553+113 in 2012 [100] and Mkn 501 in 2014 [101]) and a compilation of the Vela pulsar data from 2013 to 2014 [102] recorded by H.E.S.S. It also includes a compilation of the Crab pulsar data collected over several years by MAGIC [103], and the data from the first GRB ever to be detected with an IACT - GRB 190114C observed by MAGIC in 2019 [104]. The limits obtained from these analyses are reported in Table 6.1 together with the ones discussed above.

Regarding satellite-embarked instruments, LIV searches were exclusively performed with GRB data. A notable analysis using WT was performed in 2006 on a combination of 35 GRB data sets observed by BATSE, HETE-2 and *Swift*. This led to a linear correction $E_{QG,1} > 1.4 \times 10^{16}$ GeV [105]. This multi-source treatment which accounted for intrinsic effects led to a comparatively weaker limit due to this additional constraint. A similar analysis was performed in 2019 on a sample of 8 GRB data sets detected by *Fermi* and yielded $E_{QG,1} > 2.1 \times 10^{17}$ GeV [22], consistent with the other combined analysis. For this analysis, a DisCan method was used where the cost function was taken as the irregularity, kurtosis and skewness estimation of the pulse. Another analysis on *Fermi* data, this time focusing on the specific burst GRB 090510 in 2013, yielded $E_{QG,1} > 9.3 \times 10^{19}$ GeV and $E_{QG,2} > 4.0 \times 10^{10}$ GeV with the PV, SMM and ML methods [90]. As of today, this is the strongest limit on linear correction ever obtained which largely surpasses the Planck scale $E_P = 1.22 \times 10^{19}$ GeV and which is now used as a benchmark result. The results listed in this paragraph are also reported in Table 6.1.

Source	Type	Method	$E_{QG,1}$[GeV]	$E_{QG,2}$[GeV]	Instrument	Year†	Ref.
Mkn 421	AGN	BC	0.4×10^{17}	-	Whipple	1998	[91]
Mkn 501	AGN	ECF	2.1×10^{17}	2.6×10^{10}	MAGIC	2008	[88]
Mkn 501	AGN	ML	3.0×10^{17}	5.7×10^{10}	MAGIC	2009	[96]
Mkn 501	AGN	ML	3.6×10^{17}	8.5×10^{10}	H.E.S.S.	2019	[101]
PKS 2155-304	AGN	MCCF	7.2×10^{17}	1.4×10^{10}	H.E.S.S.	2008	[98]
		WT	5.2×10^{17}	-			
PKS 2155-304	AGN	ML	2.1×10^{18}	6.4×10^{10}	H.E.S.S.	2011	[99]
PG 1553+113	AGN	ML	4.1×10^{17}	2.1×10^{10}	H.E.S.S.	2015	[100]
Crab	PSR	BC	1.8×10^{15}	-	EGRET	1999	[97]
Crab	PSR	PC	3.0×10^{17}	0.7×10^{10}	VERITAS	2011	[92]
		DisCan	1.9×10^{17}	-			
Crab	PSR	PC	1.1×10^{17}	1.4×10^{10}	MAGIC	2017	[103]
		ML	5.5×10^{17}	5.9×10^{10}			
Crab	PSR	ML	4.0×10^{15}	-	H.E.S.S.	2015	[102]
35 GRB	GRB	WT	0.14×10^{17}	-	BATSE,HETE-2,*Swift*	2006	[105]
8 GRB	GRB	DisCan	0.21×10^{17}	-	*Fermi* LAT	2019	[22]
GRB 090510	GRB	PV,SMM,ML	2.2×10^{19}	4.0×10^{10}	*Fermi* LAT	2013	[90]
GRB 190114C	GRB	ML	0.58×10^{19}	6.3×10^{10}	MAGIC	2020	[104]

† Year of publication.

Table 6.1: Summary on up-to-date limits on $E_{QG,n}$ with additional information. Only subluminal limits are reported here.

6.2.2 Future prospects

In addition to provide strong constraints on the QG energy scale, the studies we reported here also discuss their limitations and propose solutions for improvement. We present here some of the suggested ideas.

Fiducial cuts

The current approach of IACTs to discriminate signal from background events relies on the measurement of ON and OFF regions in the sky (see Section 3.2.4.2). The OFF region is a calibration measurement used to define a fiducial cut that will then be applied to the ON set of events in order to remove background events. Although the cut is defined to discard a maximum of background events while minimising the loss of signal events, a fraction of signal events is necessarily lost with this technique. It then reduces the sensitivity for LIV studies, especially when it comes to pulsar data sets where the background photons coming from the surrounding nebula usually make up for more than 90% of the ON region events. Another approach to the background rejection was suggested in [106] where only ON region events are considered without applying any cut. This technique relies on the bayesian approach to attribute a weight to events based on the likelihood of being signal or background. This would avoid the loss of signal events and should increase the sensitivity to LIV studies.

Combine LIV effects

Although we focus solely on time-of-flight studies in this chapter, LIV can manifest under other deterministic forms such as a modified EBL absorption (see Section 1.3.2), but also a foamy nature of vacuum. Such aspects have been tested separately so far, but it is reasonable to expect more than one manifestation to affect gamma-rays propagation. A study combining simultaneous effects of LIV could shed new light on LIV searches and lead to more accurate limits on the energy scale. This combination of effects may also blur intrinsic effects arising from sources emission mechanisms as they are generated from independent processes.

Population study and inter-experiment collaboration

As discussed in Part II, the source intrinsic energy-dependent photon emission is far from negligible and can be misleading when interpreting observed time delays. Since intrinsic effects are not directly affected by the source distance - contrary to LIV ones which are propagation effects - a combination of sources at different redshifts would blur intrinsic effects. Additionally, by combining sources of different types - and thus having different emission processes - intrinsic effects would manifest under different forms while the LIV effect would be a common factor modulo the source distance. Lastly, combining sources necessarily implies a larger pool of data and would thus increase the analysis sensitivity and lead to improved limits on the energy scale.

Considering the small number of usable data sets available for each experiment (see e.g. Table 6.1), an inter-experiment collaboration would provide a larger pool of data sets diversifying the source types, distance scales and energy ranges. A consortium between H.E.S.S., MAGIC and VERITAS has been formed to explore this opportunity (more in Chapter 7) and could ideally be extended to other experiments. In particular, having a *Fermi* group join the effort would provide GRB data at lower energy and higher redshift.

The main difficulty for such a project resides in the technical aspect of the analysis, especially when it comes to combination strategies or instrument response treatment for harmonised data sets as we will discuss in the next chapter.

Chapter 7

Method development and validation for future population studies

Contents

This chapter presents the method developed in preparation of future population studies. As mentionned in the previous chapter, LIV studies benefit from large samples for a diversification of source types and distance scales. While population studies have been carried out with samples of GRBs detected by space observatories, they have never been performed with IACT data. It is therefore important to remedy this shortcoming, especially with the upcoming CTA operations. For this purpose, an open-source software called *LIVelihood* has been developed to provide a standardised analysis method for LIV time-of-flight studies. The maximum likelihood method was chosen for its superior performances. Moreover, this method provides a simple and straightforward way to combine data sets. In addition, two lag-distance models have been implemented allowing, for the first time, to perform a direct comparison of their influence on the results, but also to check their consistency. Note that intrinsic effects are excluded from this analysis as they are not sufficiently well-known.

The goal is to use this software on existing data sets from as many sources as possible. To this end, an inter-experiment working group has been formed between the three major IACT experiments: H.E.S.S., MAGIC and VERITAS. The work presented in this chapter is therefore a collaborative one in which I had a significant contribution. More specifically, I managed the instrument response and background treatment, as well as tests and calibration of the method. I was also in charge to produce all the results and actively contributed to their interpretation. The source simulations and uncertainty treatment that are presented in this chapter were managed by Sami Caroff with whom I closely collaborated. The method and results obtained with this software were presented at the TeV Particle Astrophysics conference (TeVPA, 2019) and International Cosmic Ray Conference (ICRC, 2021). They are also reported in a paper that will soon be published.

7.1 The maximum likelihood method

7.1.1 Building a probability density function

Let us go back to the likelihood $\mathcal{L}(\tau_n, \vec{\theta})$ given in Equation 6.5, with $\tau_n \propto \kappa_n(z)$ the parameter of interest. In its current form, τ_n quantifies LIV effects for a source sitting at a specific distance $\kappa_n(z)$. In order to perform combinations between multiple sources, the parameter of interest should be applicable to any source, whatever their redshift are. We thus introduce a new parameter noted λ_n defining a "distance-independent" equivalent of the τ_n parameter:

$$\lambda_n = \frac{\tau_n}{\kappa_n(z)} = \frac{\Delta t}{\Delta E_n \kappa_n(z)} = \pm \frac{n+1}{2H_0 E_{QG}^n}, \tag{7.1}$$

with $\Delta E_n \equiv |E_i^n - E_j^n|$, and λ_n being expressed in the same unit as τ_n (s/TeV^n). The profile likelihood then reads:

$$\mathcal{L}(\lambda_n) = \sup_{\vec{\theta}} \mathcal{L}(\lambda_n, \vec{\theta}) = \prod_i \frac{dP(E_{i,m}, t_i; \lambda_n)}{dE_{i,m} dt_i}, \tag{7.2}$$

with P the probability to detect a gamma-ray i with a given measured energy $E_{i,m}$ at a given time t_i. In its simplest form with only signal events and instruments taken as perfect - i.e. the measured energy is taken as the true photon energy $E_{i,m} \equiv E_{i,t}$ - the PDF P_s describing

gamma-rays after their propagation is given by:

$$P_s(E_{i,m}, t_i; \lambda_n) = \frac{\Gamma_s(E_{i,m}) C_s(t_i - \lambda_n \kappa_n(z) E_{i,m}^n)}{N_s}, \tag{7.3}$$

with $C_s(t_i - \lambda_n \kappa_n(z) E_{i,m}^n)$ the LIV-transformed light curve for signal events defined between $t_{\min}$ and $t_{\max}$, $\Gamma_S(E_{i,m}) = E_{i,m}^{-\alpha}$ the energy spectrum of index α for signal events defined between $E_{\min}$ and $E_{\max}$, and N_s the normalisation term given by

$$N_s = \int_{t_{\min}}^{t_{\max}} \int_{E_{\min}}^{E_{\max}} \Gamma_s(E_m) C_s\left(t - \lambda_n \kappa_n(z) E_m^n\right) dE_m dt. \tag{7.4}$$

7.1.2 The special case of pulsars

Contrary to AGNs and GRBs, PSRs are pulsating sources with light curves repeating periodically. Rather than a light curve, we consider a subset of the phasogram defined between $\phi_{\min} \geq 0$ and $\phi_{\max} < 1$ so that it is centered on the main peak of the repeating temporal pattern. In the PDF, the time t is then changed for a phase ϕ such that

$$t \longrightarrow \phi = \frac{t}{r_p}, \tag{7.5}$$

with r_p the source rotation period. Similarly, the LIV parameter λ_n given in Equation 7.1 is modified as follows:

$$\lambda_n \longrightarrow \eta_n = \frac{\lambda_n}{r_p}. \tag{7.6}$$

The light curve functions adapt accordingly as follows:

$$C_s(t_i - \lambda_n \kappa_n(z) E_t^n) \longrightarrow C_s(\phi_i - \eta_n \kappa_n(z) E_\phi^n). \tag{7.7}$$

This new expression now requires $\phi \in [0,1[$. However, there may exist a η_n for which $\phi_i - \eta_n \kappa_n(z) E_\phi^n$ leaks out of the period interval $[0,1[$. This issue is either solved by keeping η_n within the interval $\left[\frac{\phi-1}{\kappa_n E_\phi^n}, \frac{\phi}{\kappa_n E_\phi^n}\right]$, or by taking the decimal part of $\phi_i - \eta_n \kappa_n(z) E_\phi^n$.

Considering the $E_{QG,n}$ limits are computed with $\eta_n = 0$ (resp. $\lambda_n = 0$ for other source types), this leakage does not affect LIV results and we therefore opted for the reduced interval. The solutions used for cases with an injecting lag $\eta_n \neq 0$ are discussed in Section 7.4.2.

For simplicity and unless specified otherwise, we will keep the conventional notation with time t and parameter λ_n with an implicit transformation to phase when considering pulsars.

7.1.3 Background treatment

A more realistic PDF should contain a term describing the detection probability of background events, however small that probability is. When it comes to IACTs, the background events are associated to either hadrons mis-reconstructed as gamma-ray events, or baseline events.

Hadron events

Hadron events are usually cosmic rays which generate an EAS similar to that of the gamma-rays and which are mis-reconstructed as signal events. As their flux is relatively constant over time, their temporal distribution can be modelled with a uniform law. The energy distribution on the other hand follows a power law with spectral index $\alpha_{CR} \simeq -2.7$ up to $E = 3 \times 10^3$ TeV.

Baseline events

Contrary to hadron events, baseline events are photons from the continuous emission of the source under study or from its close surroundings. For AGNs, the baseline emission corresponds to the source quiescent state - as opposed to the flaring state - such that the stronger the flare, the more negligible the baseline emission becomes. For pulsars, the baseline corresponds to the surrounding nebula emission which usually almost completely overshadows the pulsar itself. Lastly, GRBs are extremely powerful explosion events which naturally overshadow the surrounding continuous emission such that the baseline emission is usually negligible.

Treatment

In any of these cases, the continuous emission can be modeled with a uniform temporal distribution insensitive to the LIV transformation $D(E_{i,m}, z, \lambda_n) = \lambda_n \kappa_n(z) E_{i,m}^n$, and an energy distribution following a power law with a given spectral index α_b. The PDF P_b describing background events can then be written as

$$P_b(E_{i,m}, t_i; \lambda_n) = \sum_k P_{b,k}(E_{i,m}, t_i; \lambda_n) = \frac{\Gamma_{b,k}(E_{i,m}) C_{b,k}(t_i)}{N_{b,k}}, \tag{7.8}$$

with $k = \{had, base\}$ the background types and

$$N_{b,k} = \int_{t_{\min}}^{t_{\max}} \int_{E_{\min}}^{E_{\max}} \Gamma_{b,k}(E_m) C_{b,k}(t) dE_m dt. \tag{7.9}$$

7.1.4 IRF treatment

To further improve the realisticness of the detection probability, the instrument responses should be taken into account. While the temporal response of IACTs allows for a very accurate estimation of arrival times, the energy component is usually biased by the instrument performances. This error can be corrected with instrument response functions (IRF) leading to an estimation of the instrument's acceptance and energy resolution.

7.1.4.1 Acceptance

The acceptance is the probability for an event of a given type and energy to trigger the instrument detection system and pass the event selection cuts. In addition to the reconstruction method, the acceptance largely depends on the observation conditions such as the atmospheric transparency, the source zenith angle, the position of the shower image in the camera or the instrument status. As a consequence, the acceptance is unique to each observation. The probability distribution is estimated via Monte-Carlo simulations of atmospheric showers and their measurement by the detector. This gives access to the ratio between the known total number of

events simulated and the number of reconstructed events in each energy and zenith angle bins. Such distributions are generated for signal gamma-ray photons and both types of background events, for the atmospheric and instrument conditions specific to each observation run, as well as for various zenith angles.

For simplicity, the acceptance is usually accounted for with the effective area $A_{\text{eff}}(E_t, \vec{\epsilon})$ of the telescope - i.e. the area that is sensitive to showers. It is given as a function of the incident simulated photons true energy E_t and a set of vectors $\vec{\epsilon}$ encoding the various observation conditions. It is given by

$$A_{\text{eff}}(E_t, \vec{\epsilon}) = \pi R^2 \Omega \frac{N_{\text{selec}}(E_t)}{N_{\text{MC}}(E_t)} \tag{7.10}$$

with N_{MC} the number of simulated events, N_{selec} the number of detected and selected events, R and Ω the radius and the solid angle surrounding the telescopes over which the showers were simulated. This alternative representation is particularly useful when considering data sets detected by an array of at least two telescopes as it allows to treat them as a single entity. An example of such a distribution can be found in Figure 7.1a, showing the effective area A_{eff} of H.E.S.S. for PKS 2155-304 simulation given in m^2 as a function of the simulated true energy E_t.

7.1.4.2 Energy resolution

The energy resolution quantifies the ability of the detector to accurately determine the energy of the incoming photons. It can be estimated with the probability of reconstructing an event with energy E_m given its one true incident energy E_t. The corresponding probability distribution follows a Gaussian law in natural logarithm of E_m. Its standard deviation corresponds to the energy resolution while its mean provides an estimation of a general energy bias. The migration matrix $M(E_t, E_m)$ is the two-dimensional version of this distribution which provides the probability to reconstruct an energy E_m for any incident true energy E_t and reads

$$M(E_t, E_m) = \exp\left(\frac{[E_t - E_m - b(E_m)]^2}{2r(E_m)^2}\right), \tag{7.11}$$

with $b(E_m) \equiv \Delta E_t / E_t$ the energy bias (mean) and $r(E_m)$ the energy resolution (standard deviation). An example of such a distribution can be seen in Figure 7.1b. The bias is usually negligible especially at high energy, and the energy resolution is usually of the order $\Delta E_t / E_t \sim 10\%$.

7.1.4.3 Multi-era treatment

Observation campaigns are usually separated in observation runs of several minutes (typically ~ 30 min), and each observation run is characterised by a given set of IRFs. In the case where a source flare is detected over several observation runs, the overall data set is then associated to multiple IRF files.

For AGNs and GRBs, each file characterises the data over a given time window which is defined such that there is no gap nor overlap with another time window. Therefore, there is necessarily an IRF file, and only one, that can be associated with an event i happening at a given time t_i. Since the profile likelihood function is computed for each and every event in the Monte-Carlo simulation, the PDF $P(E_{i,m}, t_i; \lambda_n)$ is computed with the specific IRF file associated to the time t_i.

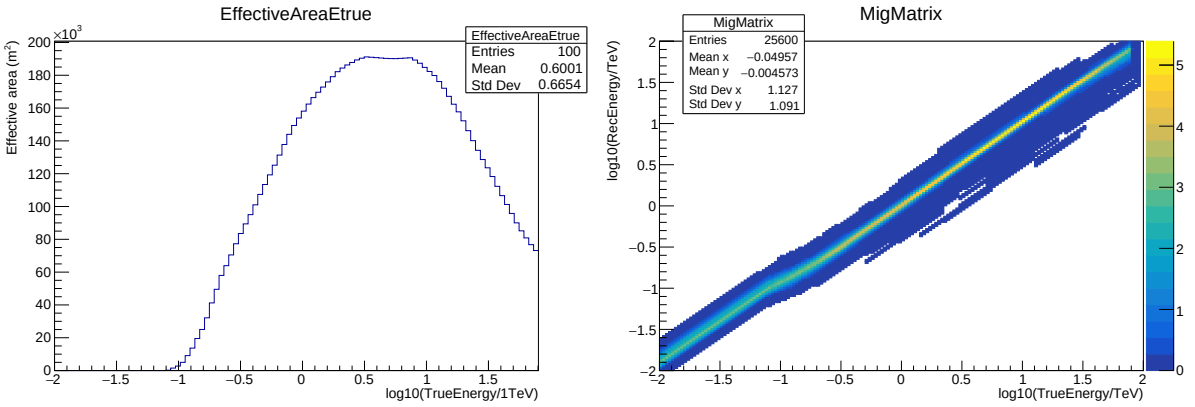

(a) Effective area A_{eff}.

(b) Migration matrix M.

Figure 7.1: Instrument response functions (IRF) of the source PKS 2155-304 for the big flare observed by H.E.S.S. in 2006.

For pulsars, the separation between era needs to be approached differently due to the periodicity of the signal. As the data sets are a compilation of observation runs - usually tens or hundreds of them taken over several years - they are associated to a similar amount of IRF files which is not manageable for this analysis. Instead of considering the exact IRF file corresponding to each and every event, a small number of mean IRF files are used to characterise a given percentage of the total number of events, regardless of their phase ϕ_i or other properties.

7.1.4.4 Optimising the computational time

In order to account for IRFs, the PDF functions for signal given in Equation 7.3 need to be modified as follows:

$$P_s(E_{i,m}, t_i; \lambda_n) = \frac{\int_0^\infty \Gamma_s(E_t) C_s(t_i - \lambda_n \kappa_n(z) E_t^n) \times A_{\text{eff}}(E_t, \vec{\epsilon}) M(E_t, E_m) dE_t}{N_s}, \tag{7.12}$$

with

$$N_s = \int_{t_{\min}}^{t_{\max}} \int_{E_{\min}}^{E_{\max}} \int_0^\infty \Gamma_s(E_t) C_s\left(t - \lambda_n \kappa_n(z) E_t^n\right) \times A_{\text{eff}}(E_t, \vec{\epsilon}) M(E_t, E_m) dE_t dE_m dt. \tag{7.13}$$

Similarly, Equation 7.8 describing background events now becomes:

$$P_b(E_{i,m}, t_i; \lambda_n) = \sum_k P_{b,k}(E_{i,m}, t_i; \lambda_n) = \frac{\Gamma_{b,k}(E_{i,m}) C_{b,k}(t_i) \times A_{\text{eff}}(E_t, \vec{\epsilon}) M(E_t, E_m) dE_t}{N_{b,k}}, \tag{7.14}$$

where

$$N_{b,k} = \int_{t_{\min}}^{t_{\max}} \int_{E_{\min}}^{E_{\max}} \int_0^\infty \Gamma_{b,k}(E_t) C_{b,k}(t) \times A_{\text{eff}}(E_t, \vec{\epsilon}) M(E_t, E_m) dE_t dE_m dt, \tag{7.15}$$

with E_t the photons true energy and E_m the photons measured energy.

The PDF functions given in Equations 7.12 and 7.14 provide a more realistic description of actual observations. However, given the IRFs are distributions (and not functions), it is not

possible to numerically differentiate the PDF to find its maximum. The only viable option is to perform a scan over the PDF for all values of λ_n. In other words, the profile likelihood given in Equations 7.2 will be computed for all the events in each Monte-Carlo simulation, and this will be done multiple times until its maximum is found.

For the analysis to be viable, one set of data should usually amount to at least several hundreds of events. Additionally, the calibration of this method will require to work with several hundreds of Monte-Carlo simulations. However, the normalisation terms are complex functions which require triple integrations. A single of these computations can be easily done with an appropriate software within approximately 1 second. However, in our case several thousands of such computations are needed which now add up to several weeks of computational run time, which is exceedingly unreasonable.

To avoid such preposterous run times, we instead use a strategy relying on tabulation. The PDF numerator and denominator are computed separately for each type of event (signal gamma-ray, hadron and baseline photon) and all IRF files, for given sampled values of the relevant variables (time t, measured energy E_m and LIV parameter λ_n). The PDF values are stored in 3-dimensional histograms as a function of the sampled variables noted t^*, E_m^* and λ_n^*. The value of the PDF for given non-sampled values t, E_m and λ_n is then retrieved with a 3D-interpolation on the corresponding histogram, and is used to compute the profile likelihood $\mathcal{L}(\lambda_n)$. This strategy allows to reduce the computational time down to minutes or hours, and this calculation now needs to be performed only once for each source. This results in the production of tables specific to each data set which can then be re-used as many times as necessary.

The variables are sampled between characteristic values on which the observables are defined: $t_{\min} \leq t^* \leq t_{\max}$, $E_{\min} \leq E_m^* \leq E_{\max}$ and $\lambda_{n,\min} \leq \lambda_n^* \leq \lambda_{n,\max}$. The true energy E_t is also sampled but it is not possible to do so on its defining interval $[0,\infty[$. Instead, new boundaries are defined and taken as large as possible while maintaining a reasonable energy step between each sampled value E_t^*: after several tests, $E_{t,\min} = 0.5$ and $E_{t,\max} = 2E_{\max}$ were chosen. As the number of values used for each variable and the λ_n interval boundaries directly impact the efficiency of the method and precision on the results, they take part in the optimisation of the method which we discuss in Section 7.4.

As a final point, when IRF files are not accounted for, the PDF function falls back to a simple expression where $E_m \equiv E_t$, removing the integration on true energy from the equation. With only double integrations, the computational time is drastically reduced. It is then equivalent to launch the analysis with or without using the tables. This situation allows us to check the consistency of the reconstructed lag distributions between the two methods (i.e. with and without tables).

7.1.5 Combination

As we mentionned earlier, combining the profile likelihood functions is easy and straightforward. It is simply done by taking the product of all the profile likelihood functions. For an even simpler expression, one can use the profile log-likelihood functions which helps get rid of

unnecessary prefactors. From Equation 7.2 we get the profile log-likelihood for source S:

$$L_S(\lambda_n) \equiv \sum_i 2\log \mathcal{L}_S(\lambda_n) = \sum_i 2\log\left(\frac{dP_S(E_{i,m}, t_i; \lambda_n)}{dE_{i,m}dt_i}\right), \tag{7.16}$$

and

$$L_{\text{comb}}(\lambda_n) = \sum_{\text{all sources}} L_S(\lambda_n). \tag{7.17}$$

7.1.6 Confidence intervals

In order for the analysis to provide reliable outputs, we need to make sure the correction term λ_n is correctly reconstructed by the method. To do so, we perform controled tests by generating 1000 randomised simulated data sets for each source where a fixed and known value of λ_n is injected, noted λ_n^{inj} in the following. This allows us to perfectly control the input and check the method depending on the output i.e. the distribution of 1000 reconstructed λ_n, noted λ_n^{rec}. This distribution usually follows a Gaussian law. A Gaussian function is thus fitted on the distribution of λ_n^{rec} and provides an estimation of the most likely λ_n value and statistical uncertainty on the reconstruction from its mean μ and standard deviation σ respectively. In the case of asymmetric light curves, the distribution of reconstructed λ_n is also asymmetric. Such a distribution is therefore fitted with an asymmetric Gaussian function with different left and right-hand side standard deviations, noted respectively σ_l and σ_r. To have a consistent approach for all sources and data sets, we will systematically use the asymmetric gaussian function regardless of the light curve and λ_n^{rec} distribution shapes.

Rather than the standard deviations, an equivalent way of estimating the statistical upper and lower limits at 1σ confidence level relies on finding the values $\lambda_{n,LL}$ and $\lambda_{n,UL}$ for which the likelihood function from Equation 7.16 yields $-L(\lambda_n) = 1$. An example of a likelihood function computed for one realisation (i.e. one Monte-Carlo out of the 1000) and its corresponding λ_n^{rec}, $\lambda_{n,LL}$ and $\lambda_{n,UL}$ can be found in Figure 7.2. As we will see later on, the systematic uncertainties are propagated to the likelihood. This second method therefore allows to take both statistical and systematic uncertainties at once and is thus the preferred estimation method. Just like it is done for λ_n^{rec}, we build the distribution of $\lambda_{n,LL}$ (resp. $\lambda_{n,UL}$), to which we fit an asymmetric Gaussian function and associate the mean μ to the most likely $\lambda_{n,LL}$ (resp. $\lambda_{n,UL}$) value. An example of the three distributions can be seen in Figure 7.3, with $\lambda_{n,LL}$, λ_n^{rec} and $\lambda_{n,UL}$ in the left, central and right panels respectively. They were obtained for GRB 190114C at linear order and for the J&P approach with $\lambda_n^{\text{inj}} = 0$. In this case, systematics are taken into account such that $\sigma_l \neq \lambda_{n,LL}$ and $\sigma_r \neq \lambda_{n,UL}$.

7.2 Lag distance models

We still need to specify the lag-distance function $\kappa_n(z)$ which has been left undefined so far. It is important to recall the modified dispersion relation that is being tested does not arise from a specific quantum gravity model or fully formulated universal theory. Therefore, there is no exact prediction on the lag-distance model, but rather simplified speculative approaches. Two of these approaches - the J&P and DSR models - have been presented in Section 1.3.1. We now use this study as an opportunity to confront them for the first time.

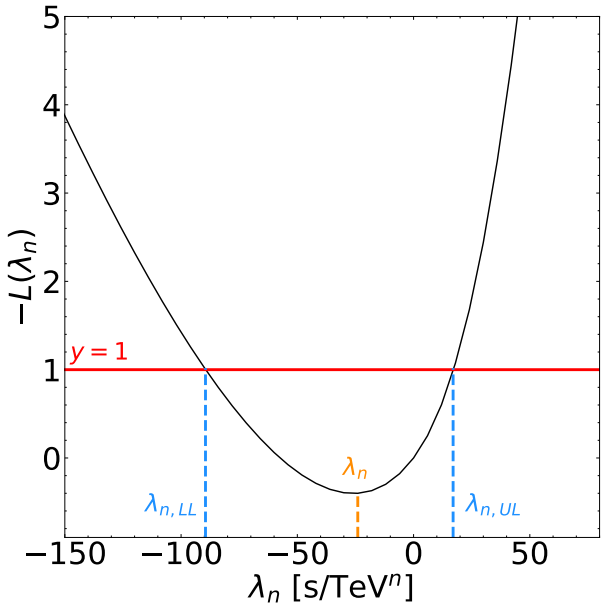

Figure 7.2: Example of a likelihood function and the corresponding $\lambda_n^{\rm rec}$, $\lambda_{n,LL}$ and $\lambda_{n,UL}$. This distribution is one realisation obtained for the GRB 190114C at linear order ($n = 1$) and J&P approach with $\lambda_n^{\rm inj} = 0$.

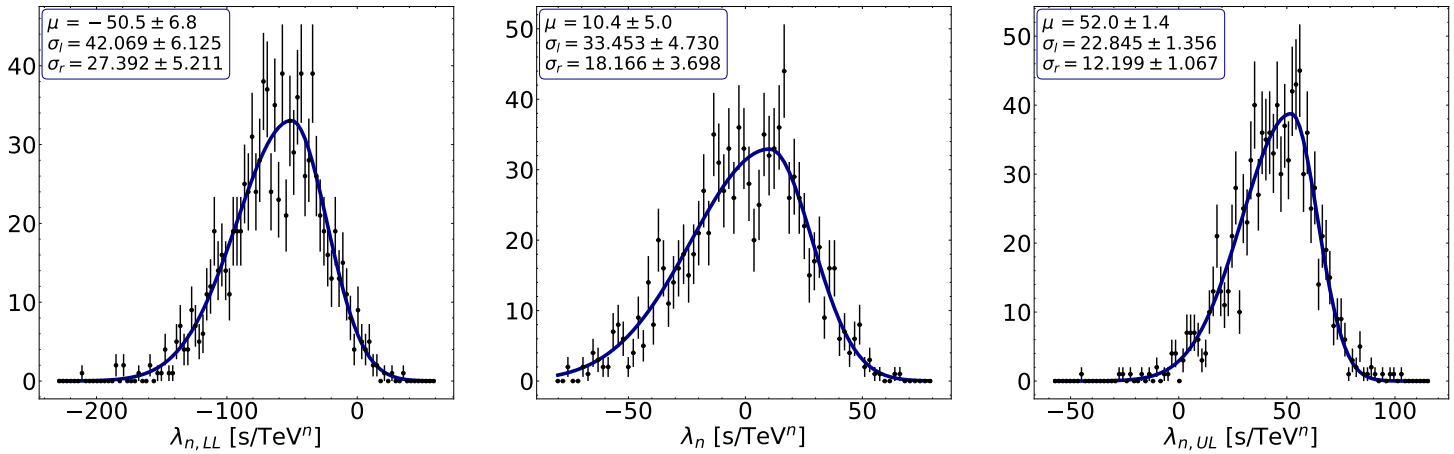

Figure 7.3: Distributions of the reconstructed λ_n (central panel), the 1σ CL lower limits $\lambda_{n,LL}$ (left panel) and upper limits $\lambda_{n,UL}$ (right panel), all fitted with asymmetric Gaussian functions (blue solid line). The fit results including the mean μ, left standard deviation σ_l and right standard deviation σ_r are shown in the upper left corner of each panel. These distributions were obtained for the GRB 190114C at linear order ($n = 1$) and J&P approach with $\lambda_n^{\rm inj} = 0$. Systematics are taken into account such that $\sigma_l \neq \lambda_{n,LL}$ and $\sigma_r \neq \lambda_{n,UL}$.

Figure 7.4 shows the two distributions $\kappa_n^{J\&P}$ and κ_n^{DSR} as a function of the redshift z for the linear $n=1$ and quadratic $n=2$ correction orders. The difference between the two models gets more and more prominent as z increases. From this plot, we can already forecast large redshift sources to provide more constraining limits under the J&P model than the DSR one. Furthermore, as mentionned in Section 1.3.1, LIV scenarii lead to a more sensible modification of the dispersion relation than DSR ones, leading to phenomenological effects expected to be larger in LIV than DSR. This is indeed what is observed in Figure 7.4 with $\kappa_n^{J\&P}$ reaching larger values than κ_n^{DSR} for a given redshift z. It is also interesting to notice a given limit on the quantum gravity energy scale could be lower than the Planck energy when computed with the DSR model, but surpass it with the J&P model. The choice of the model is therefore of great importance when it comes to the interpretation of the results.

For small z, the two models appear to be consistent, the ratio $\kappa_n^{J\&P}/\kappa_n^{DSR}$ approaching unity as z tends towards 0. Furthermore, both functions are consistent with the euclidian approximation at low redshift $\kappa_n(z) = dH_0/c$, where d is the euclidian distance to the source. As a consequence, nearby sources such as pulsars yield the same results and constraints on $E_{QG,n}$ regardless of the used lag-distance model, therefore becoming references for comparison. Since both models yield the same results for pulsars, they will only be treated for the J&P case in the rest of this chapter.

7.3 Selected sources and simulation parameters

Let us now discuss the choice of the data sets that will be used to test and calibrate the analysis tool. To expect a thorough and panoramic testing, the data sample should be a representative one where all types of sources and all distances are present. Furthermore, the sources should harbour different characteristics that would either increase or hinder the sensitivity of the method. We choose to use previously analysed data sets as reference for our test sample. On the one hand, such a sample resembles a realistic one, with realistic sources characteristics. On the other hand, since these data sets have already been analysed, we know the results we should be obtaining for individual sources at least, which provides a reference benchmark to compare the results obtained with this software and will help spot issues faster and more efficiently.

The sources used for the calibration of the method gather three flaring AGNs, two pulsars and one GRB. We briefly summarise the sources characteristics in Table 7.1.

GRB 190114C [104], sitting at redshift $z = 0.4245$, was observed by MAGIC in 2019 over a time window of 19 minutes only covering the afterglow emission. The detection sums up to 726 events detected between 300 GeV and 2 TeV with 0.055% of hadronic background events. The light curve is fitted with a curved power of index $\beta = 1.51 \pm 0.04$ (with EBL absorption). This parameterisation is a peaked function, the peak being outside of the temporal interval on which the GRB has been detected, and can be reintroduced with the help of a positive lag. The energy spectrum follows a power law of index $\alpha = 5.43 \pm 0.22$.

Mrk 501 [96] is a BL Lac object sitting at redshift $z = 0.03364$. The flare of 2005 was detected by MAGIC for a total of ~ 1800 recorded events with energy ranging from 0.15 to 10 TeV and amongst which 39% are hadronic and baseline background events. The light curve is described by a Gaussian function and the energy spectrum has an index $\alpha = 2.2$ for both signal and background.

PKS 2155-304 [99] is another BL Lac object at higher redshift $z = 0.116$. The flare of 2006 detected by H.E.S.S. is one of the brightest recorded so far with a signal to noise ratio exceeding

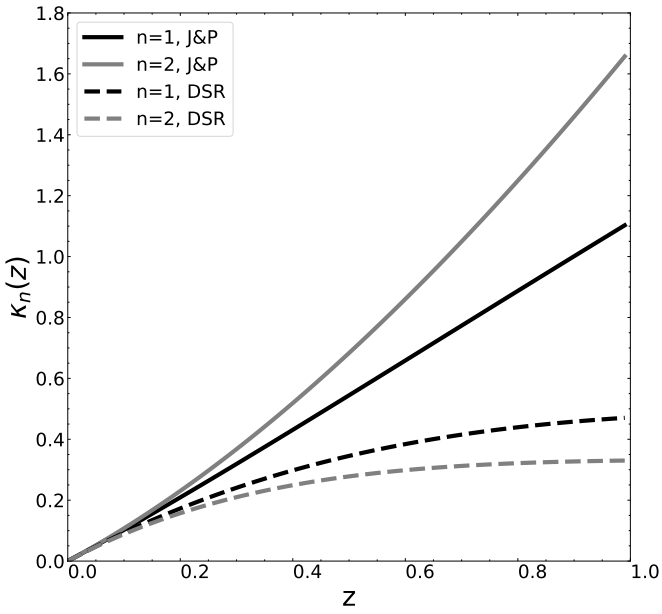

Figure 7.4: Comparison between the two lag-distance models J&P (solid line) and DSR (dashed line) through the κ_n function for both linear $n = 1$ (black) and quadratic $n = 2$ (gray) correction orders.

300. The lightcurve that spans over 4000 seconds is parameterised by the sum of five asymmetric Gaussian functions for 3526 events including 2% of background. The energy distribution that ranges between 0.25 and 4 TeV is described by a power law of index $\alpha = 3.46$, while the quiescent state (baseline events) are parameterised by $\alpha_b \sim 3.32$.

PG 1553+113 [100], yet another BL Lac object, is the furthest source of this sample with redshift $z = 0.49$. The flare of 2012 was detected by H.E.S.S. with 154 recorded events including 44% of background events. The light curve was parameterised with two Gaussian functions over 8000 seconds. The energy distribution spreads between 0.3 and 0.8 TeV and follows a power law of index $\alpha = \alpha_b = 4.8$ for signal and baseline events.

The Vela Pulsar (PSR B0833-45) [102], sitting at 0.294 kpc, rotates with a periodicity of 89 ms. The data is gathered as a compilation of observations made by H.E.S.S. between 2013 and 2014[1] for a total of 330 820 pulsed events, amongst which 98.8% are baseline background events emitted by the surrounding nebula. The phasogram defined between $\phi = 0.4$ and 0.7 is described with an asymmetric Lorentzian, while the energy distributions are parameterised by power law indices of $\alpha = 3.9$ for signal events and $\alpha_b = 1.75$ for background events.

The Crab Pulsar (PSR B0531+21) [103] has a 33.7 ms period and sits at 2.0 ± 0.5 kpc. One of the data sets used, referred as "Crab M" hereafter, is a compilation of observations made by MAGIC from 2005 to 2017. 14 896 events from the P2 region of the phase were recorded, resulting in a phase distribution described with a Gaussian function spreading between $\phi = 0.36$ and 0.45. Background generated by the surrounding nebula (baseline) make up for 96% of the

[1] We limit this data set to 2013-2014 to reproduce the one that was used for a previous LIV analysis.

events. The energy spectra are parameterised by power law indices $\alpha = 2.81$ for signal and $\alpha_b = 2.21$ for baseline events.

The other data set noted "Crab V" [92], is a compilation of high quality data recorded by VERITAS between 2007 and 2011, summing up 22 764 pulsed events from the P2 region. The background accounts for 96.4% of the events with again only baseline photons. The phase distribution was also described with a Gaussian spreading between $\phi = 0.37$ and 0.43, while the energy spectra are parameterised with $\alpha = 3.25$ for signal and $\alpha_b = 2.467$ for baseline events.

We motivate here the choice for these sources:

- **Time scale:** while the AGN and GRB light curves spread over a time window of the order of an hour, the pulsar main pulses are not lasting longer than a few milliseconds. While the former are short transients and unique occurrences, the latter are periodic phenomena such that the data is a compilation of observations taken over several years.

- **Light curve:** most of the sources harbour different light curve shapes going from a very simple Gaussian distribution (Crab pulsar) to five overlapping asymmetric gaussian distributions (PKS 2155-304), or even a power law with no defined peak (GRB 190114C afterglow).

- **Energy:** each data set is defined over a specific energy range that goes up to different maximum energies. The GRB and two AGNs (PKS 2155-304 and Mkn 501) go up to a few TeV while the third AGN (PG 1553+113) stays within the hundred GeV range. Pulsars on the other hand reach up to higher energies closing in to ten TeV.

- **Signal to noise ratio:** all scenarii are represented, going from an almost pure signal with PKS 2155-304 and its 2% background, to pulsars which are completely dominated by the surrounding nebula leading to a background reaching up to 99.8% for Vela. PG 1553+113 on the other hand shows an approximately fifty-fifty ratio.

- **Distances:** here again, all scenarii are represented going from pulsars which are local sources sitting within the Galaxy, to very distant cosmological sources such as PG 1553+113 sitting at redshift $z = 0.49$. Since pulsars are so close, it is more suitable to refer to their euclidian distance given in kpc rather than their redshift, which is exceedingly small compared to AGNs and GRBs.

- **Instruments:** all sources have been detected with three different experiments and under different conditions such that all data sets are unique. In particular, the Crab pulsar is represented twice from the detections made by MAGIC and VERITAS. Although its characteristics do not change, the conditions under which it has been observed are drastically different such that the two data sets could very well represent two different sources. Furthermore, the multiplicity of instruments reproduces a set-up similar to that of the future CTA observatory.

Source	Energy [TeV]	Time/Phase	Spectral index α	α_b	Lightcurve shape	Events	Background prop. had.	base.	Distance	Ref.
GRB 190114C	0.3 - 2	60 - 1200 s	5.43	-	Curved power law	726	0.055	0.	$z = 0.4245$	[104]
PG 1553+113	0.4 - 0.8	0. - 8000 s	4.8	4.8	Double Gauss	72	0.29	0.15	$z = 0.49$	[100]
Mkn 501	0.25 - 11	0. - 1531 s	2.2	2.2	Single Gauss	1800	0.39	0.	$z = 0.03364$	[96]
PKS 2155-304	0.28 - 4	0. - 4000 s	3.46	3.32	5 Asymmetric Gauss	2965	0.	0.02	$z = 0.116$	[99]
Crab pulsar (M)	0.4 - 7	0.36 - 0.45	2.8	2.47	Single Gauss + Baseline	14869	0.	0.961	2 kpc	[103]
Crab pulsar (V)	0.2 - 10	0.37 - 0.43	3.25	2.47	Single Gauss + Baseline	22764	0.	0.964	2 kpc	[92]
Vela pulsar	0.06 - 0.15	0.40 - 0.70	3.9	1.75	Asymetric Lorentzian	3956	0.	0.998	0.294 kpc	[102]

Table 7.1: Simulated sources. For pulsars, the time range is given in phase. Abreviations used: had - hadrons; base - baseline.

7.4 Tests and calibration

A number of factors can induce a difference between the injected and reconstructed λ_n. In this section we will review some of the main sources of such discrepancies as well as the tests used to bring them to a minimum. We will make the distinction between two types of errors found in the reconstructed λ_n that is parameterised by $\lambda_n^{\text{rec}} = a\lambda_n^{\text{inj}} + b$. Considering a perfect reconstruction would yield $a = 1$ and $b = 0$, we define the following errors:

- **The offset (on *b*)** which is a fixed error that will shift the reconstructed value regardless of the injected one. This error appears most clearly with an injected lag $\lambda_n^{\text{inj}} = 0$.
- **The bias (on *a*)** which is a relative error that will shift the reconstructed value depending on the injected one, usually getting bigger as the injected λ_n^{inj} gets large.

7.4.1 At $\lambda_n = 0$: tabulation settings

The tabulation strategy introduced in Section 7.1.4.4 is used to drastically reduce the computational time and ressources. It however requires a careful optimisation since the values of the PDF and its normalisation are binned. The precision on the said values therefore depends on the binning applied to the variables (time, measured energy and lag) as well as the range on which they are defined.

The range on parameter λ_n

Since each data set of a given source has its own characteristics - number of events, light curve shape, spectral index, signal to background ratio, source distance, instrument response, etc. - the λ_n^{rec} distribution is expected to be unique, and in particular the statistical uncertainty should vary from one set to another. This uncertainty on λ_n^{rec} can be as small as a few s/TeV^n for GRBs, or as large as millions of s/TeV^n for pulsars. Although all characteristics listed above take a part in this discrepancy, it is generally dominated by the source distance. This discrepancy could be avoided by using the scaled LIV parameter τ_n, but the combination of sources requires the use of the distance-independent parameter λ_n. This implies each source to have different sensitivity to the λ_n parameter. Generally speaking, we have that:

- GRBs scale between $\lambda_n \sim 10^0 - 10^2$ s/TeV^n;
- AGNs scale between $\lambda_n \sim 10^1 - 10^4$ s/TeV^n;
- PSRs scale between $\lambda_n \sim 10^3 - 10^6$ s/TeV^n.

Each data set should then be given a specific range $[\lambda_{n,\min}, \lambda_{n,\max}]$ on which λ_n should be tabulated. We define it with respect to the standard deviations (statistical uncertainty only) found at $\lambda_n^{\text{inj}} = 0$ when all IRFs are accounted for such that $\lambda_{n,\min} = -10 \times \max(\sigma_l, \sigma_r)$ and $\lambda_{n,\max} = +10 \times \max(\sigma_l, \sigma_r)$. Note that both boundaries are given the same value for simplicity and retaining a symmetry around zero. This range is built for each individual source at each correction order n and each lag-distance model. Table 7.2 summarises all the intervals defined for this work. For practical reasons, the algorithm maximising the likelihood is set to search and test values of λ_n on the same intervals.

Source	$n=1$		$n=2$	
	J&P [s/TeV]	DSR [s/TeV]	J&P [s/TeV^2]	DSR [s/TeV^2]
GRB 190114C	300	460	430	630
Mkn 501	2300	2500	400	430
PKS 2155-304	910	1000	620	740
PG 1553+113	13×10^3	20×10^3	20×10^3	43×10^3
Crab (M)	4500	-	4600	-
Crab (V)	7×10^3	-	25×10^3	-
Vela	3×10^5	-	40×10^5	-

Table 7.2: Boundaries defining the λ_n intervals for each source at each correction order n and each lag-distance model.

Tables binning and convergence plots

The sampling required by the tabulation method introduces a source of inaccuracy on the PDF function. The level of precision achieved with this method then greatly depends on the sampling of each variable and the interpolation method that is used to retrieve intermediate values of the PDF. It has been decided to work with a linear interpolation algorithm[2] for simplicity. Therefore, the variable sampling is the only leverage left to twick the precision reachable with this method.

The simplest way to increase this precision is to tightly sample the variables, i.e. get as many bins as possible. However, since the computation is performed for each binned value of the variables, having too many bins would yield exceedingly long computational times and defeat the purpose of the tabulation method. On the contrary, having too small a number of bins can lead to errors on λ_n^{rec} and the introduction of unwanted offsets. We thus want to find a compromise between precision and computational time with the minimum number of bins that ensures an unbiased reconstruction. An advanced sampling method would require to check all inter-dependencies of the three variables (time, measured energy and lag) to find the optimal bin number for each of them, given the data set under study. A simpler and more cost-effective method we decided to use consists in systematically assigning the same number of bins to the three variables.

We perform a scan on tables generated with various number of bins and check the reconstructed λ_n^{rec}. We can then build so-called "convergence plots" showing the difference $\lambda_n^{\text{rec}} - \lambda_n^{\text{inj}}$ between reconstructed and injected λ_n as a function of the number of bins. An example of such plot can be found in Figure 7.5, obtained for GRB 190114C at linear order ($n=1$) for the J&P case. The convergences obtained for all other sources at each order and for each lag-distance model can be found in Annex B (c.f. Figure B.1). The grey envelope corresponds to the quadratic sum between the 1σ statistical uncertainty on the reconstruction (standard deviation), and the difference between the mean value of the reconstructed λ_n obtained from the fit and the distribution itself noted $\delta\lambda_n = |\lambda_n^{histo} - \lambda_n^{fit}|$. Although it is treated a bit differently, this difference will be accounted for as a systematic uncertainty in the following. Note that these plots were produced without accounting for IRFs as they do not modify the convergence

[2]The ROOT framework `https://root.cern.ch` provides predefined functions including a 3-dimensional linear interpolation algorithm.

trend. Furthermore, IRFs tend to increase the error on the reconstruction - i.e. thicken the grey envelope - the convergence point becoming more difficult to spot.

The binning should be chosen as the minimum number of bins required to yield a value of $\lambda_n^{\rm rec} - \lambda_n^{\rm inj}$ compatible with zero within 1σ error. We however adopted a conservative approach and actually chose a larger number of bins than the strictly optimal one when the plot fully converges. It appears there is no generic rule on when such plots should start to converge as it greatly depends on the range of λ_n, complexity of the light curve and its definition (linked to statistics), and many other parameters. The chosen bin numbers are listed in Table 7.3 for all sources at each correction order and for both lag-distance models.

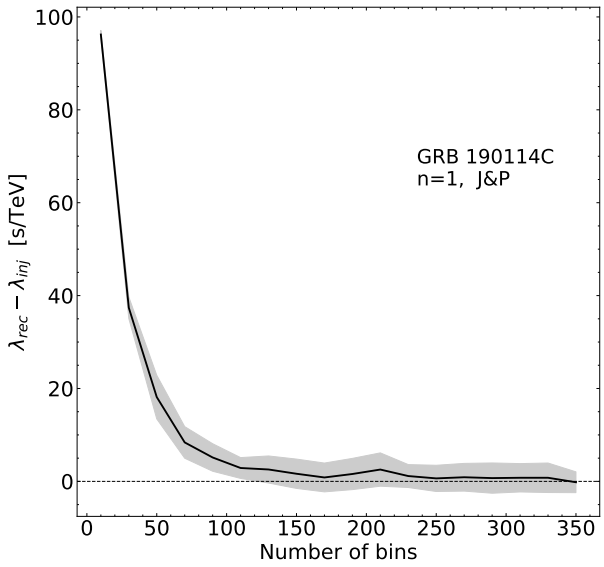

Figure 7.5: Example of a convergence plot obtained for GRB 190114C at linear order ($n = 1$) for the J&P case.

Source	$n = 1$		$n = 2$	
	J&P	DSR	J&P	DSR
	[s/TeV]	[s/TeV]	[s/TeV^2]	[s/TeV^2]
GRB 190114C	200	200	150	150
Mkn 501	50	50	50	50
PKS 2155-304	130	130	130	130
PG 1553+113	50	50	50	50
Crab (M)	200	-	200	-
Crab (V)	70	-	70	-
Vela	150	-	150	-

Table 7.3: Choice of the bin numbers to be used in tables for each source, at each correction order n and for each lag-distance model.

7.4.2 For $\lambda_n \neq 0$: calibration

Range for the injected lags

We have optimised our method such that zero lag is yielded when none has been injected. We now move on to cases with non-zero injected lag with $\lambda_n^{\text{inj}} \neq 0$ and check for biases. To do so, we perform yet another scan but this time on λ_n^{inj} values. Since the tables are defined on the intervals listed in Table 7.2 and the minimiser is set to test values within the same intervals, we chose to set a boundary on the injected lag such that

$$\lambda_{n,\text{bound}}^{\text{inj}}| = 5 \times \max(\sigma_l, \sigma_r), \tag{7.18}$$

i.e. no more than half of the interval on which λ_n is defined. The only exception to this rule of thumb concerns the pulsars. Indeed, as we have mentionned in Section 7.1.2, the solution to prevent event leakage consists in only considering η_n that ensure $\phi_i - \eta_n \kappa_n(z) E_t^n \in [0,1[$ which may be in contradiction with the previous condition. From Equations 7.1 and 7.6, we get that in order for all events to stay within the period interval, we need:

$$\eta_{n,\text{bound}}^{\text{inj}} < \left(\frac{\Delta\phi_{\max} r_p}{\kappa_n(z) E_{\max}^n}\Big|_{\Delta\phi_{\max}=1} = \frac{r_p}{\kappa_n(z) E_{\max}^n} \right). \tag{7.19}$$

If $\eta_{n,\text{bound}}^{\text{inj}} \geq \lambda_{n,\text{bound}}^{\text{inj}}/r_p$, then the same boundary condition as other sources is used and $|\eta_{n,\text{bound}}^{\text{inj}}| = 5 \times \max(\sigma_l, \sigma_r)$.

The only cases for which the condition in Equation 7.19 is not met is for the data sets of the Crab pulsar at quadratic correction order. The modified $\eta_{n,\text{bound}}^{\text{inj}}$ obtained in these cases were still big enough for most events to leak from the period interval on which the phasogram is defined (see Table 7.1). However it was not viable to further reduce $\eta_{n,\text{bound}}^{\text{inj}}$ as the interval would become too small, and the reconstruction would be completely dominated by the particularly large reconstruction uncertainty. As a selection based on the time, measured energy and η_n ranges is applied to the shifted events, any event leaking out of these ranges are not taken into account in the analysis and thus simply lost. We thus decided to apply a cut on the maximum energy of the range and lose very high energy photons (which would have been lost either way). The energies are then reduced to $E_{\max} = 3.6$ TeV and $E_{\max} = 3$ TeV for the MAGIC and VERITAS data sets respectively.

Calibration plots and the method performance

Calibration plots show the reconstructed lag λ_n^{rec} as a function of the injected one λ_n^{inj}. Examples for one individual source (GRB 190114C) and all the sources combined at linear order for the J&P case can be found in Figure 7.6. The calibrations for all individual sources and combinations for all orders and lag-distance models can be found in Annex B (c.f. Figures B.2 and B.3). The combinations tested here are:

- **Crab M + V** combines the two Crab pulsar data sets from MAGIC (M) and VERITAS (V);
- **PSR** combines the three pulsars (Crab MAGIC, Crab VERITAS and Vela);
- **AGN** combines the three AGNs (PKS 2155-304, PG 1553+113 and Mkn 501);

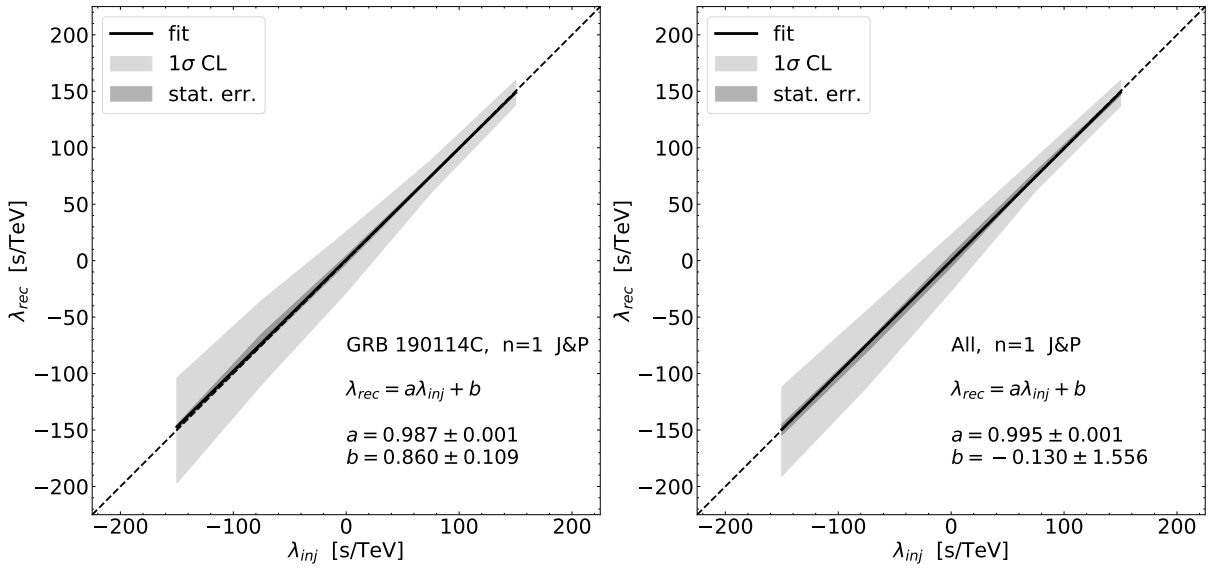

(a) GRB 190114C, $n = 1$, J&P.

(b) All sources, $n = 1$, J&P.

Figure 7.6: Example of calibration plots for an individual source (a) and a combination (b).

- **AGN+PSR** combines six data sets with all the pulsars and all the AGNs;
- **GRB+PSR** combines four data sets with all the pulsars and the GRB;
- **GRB+AGN** combines four data sets with all the AGNs and the GRB;
- **All** combines all the seven data sets with (three pulsars, three AGNs and the GRB).

For this work, we produced calibration plots with five points sitted at $\lambda_n^{\text{inj}} = \{-5, -2.5, 0, 2.5, 5\} \times \max(\sigma_l, \sigma_r)$, with the exception of Crab data sets for $n = 2$ for the reasons discussed in the above paragraph. The grey envelope corresponds to the 1σ error accounting for statistical uncertainties only, as systematics need to be estimated separately. A linear function defined by $\lambda_n^{\text{rec}} = a \times \lambda_n^{\text{inj}} + b$ is then fitted to the plot, with expected values $a = 1$ and $b = 0$ for a perfect reconstruction. Having $b \neq 0$ indicates the presence of an offset while $a \neq 1$ indicates the method is biased. This sanity check allowed us to spot and fix many issues within the code.

These plots ultimately provide an estimation on the performance of the method on various scenarii. Several observations can be made here:

- All the calibration plots have a symmetric envelope except for the ones featuring the GRB 190114C. This is most likely due to the highly asymmetric shape of this source light curve (afterglow defined by a curved power law). When applying $\lambda_n^{\text{inj}} \leq 0$, the light curve is monotonous and no peak can be used as reference points. Instead, the index of the power law is used to estimate the lag λ_n. On the other hand, for $\lambda_n^{\text{inj}} \gg 0$ the peak starts to move into the time window on which the light curve is defined and drastically improves the performance of the lag estimation, thus yielding a lesser statistical uncertainty and thinner uncertainty envelope.
- The $n = 2$ plots appear more unstable and further from the ideal linear function $\lambda_n^{\text{rec}} = \lambda_n^{\text{inj}}$. This is explained by the leakage of events (i.e. $\lambda_n E^n \kappa_n(z) < t_{\min}$ or $\lambda_n E^n \kappa_n(z) >$

$t_{\max}$) which is emphasised for the quadratic correction order. The bigger the maximum energy $E_{\max}$, the more events are susceptible to leak and provoke a bias. Although in most cases this leakage is negligible or even nonexistent, it is accentuated by the energy migration induced by IRFs. For data sets with migration matrices particularly unprecise, the leakage can start to become sensible. This was actually the biggest issue faced for GRB 190114C and PG 1553+113 analysis. From the combination of their especially steep energy spectral indices (resp. $\alpha = 5.43$ and $\alpha = 4.8$) with their unprecise migration matrices and acceptance, a large fraction of events was lost after the transformation. To solve this problem, some migration matrices have been re-simulated and fitted with a higher precision which helped reduce the overall bias.

- The calibration plots for pulsars are especially coarse as compared to other sources. This is again due to the leakage of events and the small injected lags. Indeed, as the injected lag is small, the uncertainty starts to become comparatively large. It is equivalent to zooming on a portion of the plot. As a consequence, the variations will become more prominent and give a feeling of coarseness to the plots.

- The combination plots appear to be smoother than the individual ones. This can be explained by the increased statistics which tends to smooth out or blur the irregularities brought by each source.

- The combination plots also appear to be dominated by the most stringent source (i.e. the one with the smallest uncertainty envelope), which in turn explains why combinations featuring the GRB retain the specific asymmetry of that source. Generally speaking, we have that GRBs are more constraining than AGNs, themselves more constraining than PSRs.

Except for the Crab and Vela pulsar in the quadratic cases which revealed to be especially challenging cases, all the calibration plots show a reconstruction with a maximum error of 10%, i.e. the bias parameter is such that $0.9 < a < 1.1$. The offset parameter b is on the other hand usually compatible with zero within its uncertainty. In most cases, the bias is reduced to less than 5%. It is then safe to assume the method shows first-rate performance and should provide reliable results when applied to actual data.

7.5 Statistical and systematic uncertainties

One of the sources of systematic uncertainties is the template model that is built to approximate a LIV-free emission (light curve shape and spectral index). Some of the other sources of uncertainties arise from the detection itself with instrument performances, event reconstruction and selection cuts. In particular, we need to account for the energy scale of the instrument and the ratio between signal and background events. The combination of various instruments and a proper treatment of IRF is however expected to decrease such uncertainties. A last source of error can be found in the fit applied to the λ_n^{rec} distribution introduced in the previous section as $\delta\lambda_n$.

Except for $\delta\lambda_n$, the uncertainties listed above are propagated as nuisance parameters with profile likelihoods. As this operation tends to make the likelihood computation much heavier, the systematic uncertainties are studied without accounting for IRFs. The log-likelihoods are

thus written as:

$$L(\lambda_n, \vec{\theta}) = L_S(\lambda_n, \vec{\theta}) + \sum_{\vec{\theta}_\mathrm{x}} L_{\vec{\theta}_\mathrm{x}}(\vec{\theta}_\mathrm{x}). \tag{7.20}$$

$\vec{\theta_\mathrm{x}}$ is a sub-vector of $\vec{\theta}$ which includes:

- $\vec{\theta_T}$ the light curve template parameters;
- θ_α the spectral index for the signal energy distribution;
- θ_{SBR} the signal to background ratio;
- θ_{ES} the energy scale;
- θ_z the source distance or redshift.

It is possible to make a simple and viable assumption where $\mathcal{L}_{\vec{\theta}_\mathrm{x}}(\vec{\theta}_\mathrm{x}) = \exp\left[L_{\vec{\theta}_\mathrm{x}}(\vec{\theta}_\mathrm{x})\right]$ follows a normal distribution, leading to the log-likelihood following a χ^2 distribution:

$$L_{\vec{\theta}_\mathrm{x}}(\vec{\theta}_\mathrm{x}) = \frac{\left[\theta_{\mathrm{x},i} - \bar{\theta}_{\mathrm{x},i}\right]^2}{2\sigma_{\theta_{\mathrm{x},i}}}. \tag{7.21}$$

This assumption is made for all nuisance parameters except for the template parameters $\vec{\theta_T}$ which requires a different treatment. One can either account for uncertainties on each parameter in $\vec{\theta_T}$ as nuisance parameters in the $L_S(\lambda_n, \vec{\theta})$ log-likelihood leading to $L_{\vec{\theta_T}}(\vec{\theta_T}) = 0$. Alternatively, one can evaluate errors directly from the template function. Using the template light curve function for signal $C_s(t_i, \vec{\theta_T}) \equiv C_s(t_i - \lambda_n \kappa_n(z) E_t^n)\Big|_{\lambda_n = 0}$, and considering the template temporal function $C_s(t_i, \vec{\theta_T})$ at t_i can be assimilated to a one-event likelihood function, we have:

$$L_{\vec{\theta_T}}(\vec{\theta_T}) = \sum_{i=0}^{N_T} \log\left[\frac{C_s(t_i, \vec{\theta_T})}{N_{C_s}}\right] \tag{7.22}$$

with N_T the number of events in the template light curve and N_{C_s} the normalisation function of C_s. The second option was preferred for this work.

In order to study the impact of each nuisance parameter, Equation 7.21 is computed for a single parameter such that $L_{\vec{\theta}_\mathrm{x}}(\vec{\theta}_\mathrm{x}) = 0$ except for the one nuisance parameter that is tested. Finding the λ_n for which we have $L(\lambda_n, \vec{\theta}) = 1$ provides the statistical and systematic uncertainties on the reconstruction for a given nuisance parameter. The total uncertainty is then computed as the quadratic sum of each individual systematic and statistical uncertainty. They are presented in Table 7.4 for the J&P case and Table 7.5 for the DSR case, for each source and each combination.

It appears that the main uncertainty at linear correction order for individual sources is the statistical uncertainty on the light curve template. This confirms the lack of knowledge and precision on the source itself and its primary emission to be the main drawback of the maximum likelihood method. For the quadratic correction order, the inaccuracy on the energy distributions prevails in some cases with the energy scale or error on the power law index now dominating the systematic uncertainties. This is again reasonnable as the LIV effect is coupled with the square of the energy E^2 and could overshadow the light curve template uncertainty. The dominant

systematic uncertainty for combinations of sources is then given by the most stringent source in the sample.

7.6 Results and discussion on the QG energy scale

From Equation 7.1, the quantum gravity energy scale writes:

$$E_{QG,n} = \left[\frac{2}{n+1} \left(\lambda_n + \sqrt{\delta_{stat}^2 + \sigma^2 \delta_{syst}^2} \right) H_0 \right]^{\frac{1}{n}}. \tag{7.23}$$

δ_{stat} is the statistical error taken as the standard deviation (σ_r for subluminal and σ_l for superluminal cases) of the asymmetric Gaussian fitted on the λ_n^{rec} distribution. δ_{syst} is the total systematic error (see Tables 7.4 and 7.5) computed for a confidence level of 68%. Lastly, σ is a real number allowing to set the confidence level[3]. This expression becomes an upper limit when no energy-dependent time delay can be found. All the results reported below are taken as upper limits. As limits obtained for pulsars are the same with the J&P and DSR models, only J&P limits are reported. Tables 7.6 and 7.7 summarise all the upper limits obtained for the subluminal and superluminal cases respectively, both with and without systematic uncertainties accounted for. The results are commented in the following sections.

7.6.1 Individual sources and combinations

In accordance with previously published results (c.f. Table 6.1), GRB 190114C yields the most constraining limits on $E_{QG,n}$ thanks to its high redshift, large statistics, and wide energy range, even though only the afterglow has been detected. Similarly to what has been observed in calibration plots, the combinations are dominated by the most constraining source in the sample. Therefore, GRB 190114C dominates and sets the trend to any combination it is included in. Although only one GRB was tested in this work, we expect any other GRB would yield similar results and dominate combinations. Note that the detection of a GRB prompt emission should yield even much stronger constraints.

When the GRB is not included in combination samples, AGNs start to dominate. In particular, a competition between PKS 2155-304 and Mrk 501 appears. The former tends to dominate at the linear order thanks to its high redshift ($z^{\text{PKS}} \sim 5 z^{\text{Mkn}}$) and event statistics, while the latter tends to dominate at the quadratic order thanks to its energy range reaching higher energies than PKS 2155-304 with $E_{\text{max}}^{\text{Mkn}} \sim 2 E_{\text{max}}^{\text{PKS}}$. Even though its redshift is the highest of all the sources included in this work, PG 1553+113 is left out of this competition due to its smaller number of events, lower signal to background ratio and limited energy range.

When only PSRs are included in a sample, the combination appears to be dominated by the Crab pulsar since its signal to background ratio, energy range and distance are outclassing the Vela pulsar ones. Still, pulsars appear to have a marginal impact on the overall combination due to their closeness. Although a very large redshift does not ensure the dominance of a source, a very low distance tends to become a great handicap and yield marginal impact to the limits. However, as the limits provided by pulsars are independent of any lag-distance approach, they provide model free constraints and set a reference for comparison with other sources.

[3]Setting $\sigma = 1$ leaves the CL at 68%, $\sigma = 2$ brings the CL up to 95%, $\sigma = 3$ brings it up to 99.7%, etc.

Source	Correction order	Template statistics [s/TeV^n]	Energy scale [s/TeV^n]	Background normalization [s/TeV^n]	Uncertainty on power law index [s/TeV^n]	Distance/redshift uncertainty [s/TeV^n]	Reconstruction uncertainty [s/TeV^n]	All syst. combined [s/TeV^n]
GRB 190114C	$n=1$	17.8	6.9	8.0	9.4	<7.7	3.0	25.6
	$n=2$	9.4	12.4	1.7	15.4	<9	4.2	24.1
PKS 2155-304	$n=1$	101	11.7	<20	<22	17.8	<3.3	107
	$n=2$	21.8	19.3	0.7	8.1	12.0	<2.2	37.4
Mrk 501	$n=1$	155	56	<51	49	1.	<8.5	197
	$n=2$	11.2	18.3	<10.3	9.3	0.19	<1.6	28.8
PG1553+113	$n=1$	631	150	324	<361	112	<64	727
	$n=2$	916	638	537	<552	338	<112	1282
Crab V	$n=1$	897	137	<73	142	145	<25	1135
	$n=2$	1141	410	<264	694	265	<174	1820
Crab M	$n=1$	371	66	7	23	74	<11	416
	$n=2$	167	64.5	61	24	48	<72	190
Vela	$n=1$	1.36×10^4	1.03×10^4	0.46×10^4	$<1.3\times10^4$	1.30×10^3	$<5.87\times10^3$	2.28×10^4
	$n=2$	1.0×10^5	2.05×10^5	0.48×10^5	$<1.5\times10^5$	1.57×10^5	$<0.95\times10^5$	3.05×10^5
Crab (M+V)	$n=1$	357	49	<56	32	61	<32	398
	$n=2$	161	59	45	59	38	<83	197
PSR	$n=1$	355	52	<58	38	58	<11	394
	$n=2$	90	71	49	24	62	<55	138
AGN	$n=1$	89.5	12	<15	3.7	15.8	<2.9	94.9
	$n=2$	10.1	11.1	<6	6.2	3.4	<1.3	19.7
AGN+PSR	$n=1$	85	11	<18	5	15	<2.9	91
	$n=2$	9.6	10.9	<8	5.9	4.5	<1.1	17.8
GRB+AGN	$n=1$	17.8	5.8	6.8	8.3	1.4	3.3	24.5
	$n=2$	6.8	7.8	<6.6	9.0	1.7	1.4	16.2
GRB+PSR	$n=1$	17.5	6.7	7.9	9.1	1.0	3.2	24.9
	$n=2$	8.1	11.3	1.6	12.7	2.8	<1.1	19.4
All	$n=1$	18.0	5.8	6.7	8.2	1.5	4.1	24.8
	$n=2$	7.5	7.7	<6.2	8.2	2.4	4.8	16.4

Table 7.4: Summary of systematic uncertainties given for all sources and combinations simulated for the J&P case. The dominating uncertainties are shown in orange.

Source	Correction order	Template statistics [s/TeV^n]	Energy scale [s/TeV^n]	Background normalization [s/TeV^n]	Uncertainty on power law index [s/TeV^n]	Distance/redshift uncertainty [s/TeV^n]	Reconstruction uncertainty [s/TeV^n]	All syst. combined [s/TeV^n]
GRB 190114C	$n=1$	26.2	10.2	11.9	13.9	<11.2	5.5	38.0
	$n=2$	18.0	25.5	3.8	30.0	6.2	10.6	47.8
PKS 2155-304	$n=1$	113	12.7	<22.5	<24.2	17.3	<3.6	119
	$n=2$	25.8	23.7	3.4	7.0	14.8	<2.9	45.6
Mrk 501	$n=1$	160	58	<53	51	1.	<8.0	204
	$n=2$	12.0	19.6	<11	10.0	0.2	<1.8	30.9
PG1553+113	$n=1$	968	311	545	<555	<522	<104	1131
	$n=2$	2200	1545	1259	<1377	295	<250	2965
AGN	$n=1$	98.4	12.9	<17	4.2	14.8	<3.2	103
	$n=2$	11.1	13.0	<6.6	7.3	2.1	<1.5	22.5
AGN+PSR	$n=1$	94	12	<19	4.3	15	<3.0	99
	$n=2$	9.1	11.9	<8.2	6.1	3.9	<1.2	19.1
GRB+AGN	$n=1$	26.2	7.7	9.1	11.2	2.4	1.7	34.7
	$n=2$	10.1	11.2	<8.5	9.8	1.7	4.3	21.7
GRB+PSR	$n=1$	26.0	9.7	11.3	13.3	1.8	3.9	37.4
	$n=2$	8.0	18.0	<15.4	18.5	6.5	<2.5	28.7
All	$n=1$	27.0	7.7	8.7	10.9	2.8	<4.5	35.6
	$n=2$	10.1	11.0	<0.96	8.3	3.2	<4.2	19.8

Table 7.5: Summary of systematic uncertainties for all sources and combinations simulated for the DSR case. The dominating uncertainties are shown in orange.

Source	$E_{QG,1}$				$E_{QG,2}$			
	J&P (10^{18} GeV)		DSR (10^{18} GeV)		J&P (10^{10} GeV)		DSR (10^{10} GeV)	
	w/o syst.	w/ syst.	w/o syst.	w/ syst.	w/o syst.	w/ syst.	w/o syst.	w/ syst.
GRB 190114C	9.2	4.0	6.5	2.7	14.2	8.3	9.5	5.8
PKS 2155-304	2.8	1.0	2.6	0.9	8.2	6.2	7.2	5.5
Mrk 501	1.1	0.5	1.1	0.5	9.6	7.1	9.3	6.9
PG 1553+113	0.17	0.11	0.10	0.07	1.3	1.0	0.87	0.68
Crab (M)	0.80	0.65	-	-	3.0	2.5	-	-
Crab (V)	0.48	0.10	-	-	1.5	0.94	-	-
Vela	5.1×10^{-3}	3.5×10^{-3}	-	-	5.6×10^{-2}	5.5×10^{-2}	-	-
Crab (M+V)	1.0	0.28	-	-	3.3	2.6	-	-
PSR	1.0	0.28	-	-	3.3	2.8	-	-
AGN	3.0	1.1	2.8	1.0	10.8	8.3	10.5	7.9
AGN+PSR	3.3	1.2	3.0	1.1	10.6	8.5	10.1	8.3
GRB+PSR	9.2	4.1	6.6	2.8	14.3	9.2	9.1	7.0
GRB+AGN	9.5	4.1	6.9	3.0	14.5	9.7	11.4	8.2
All combined	9.5	4.1	7.0	2.9	14.4	9.7	11.1	8.4

Table 7.6: 95% CL limits obtained for individual objects and combinations for the subluminal case.

Source	$E_{QG,1}$				$E_{QG,2}$			
	J&P (10^{18} GeV)		DSR (10^{18} GeV)		J&P (10^{10} GeV)		DSR (10^{10} GeV)	
	w/o syst.	w/ syst.	w/o syst.	w/ syst.	w/o syst.	w/ syst.	w/o syst.	w/ syst.
GRB 190114C	8.4	3.9	5.0	2.6	10.0	7.7	6.7	5.3
PKS 2155-304	2.8	1.0	2.5	0.9	7.8	6.0	7.1	5.5
Mrk 501	1.1	0.5	1.1	0.5	9.5	7.1	9.2	6.8
PG 1553+113	0.16	0.11	0.10	0.07	1.2	1.0	0.80	0.66
Crab (M)	0.77	0.65	-	-	3.0	2.5	-	-
Crab (V)	0.43	0.10	-	-	1.4	0.94	-	-
Vela	5.1×10^{-3}	3.5×10^{-3}	-	-	10.0×10^{-2}	5.7×10^{-2}	-	-
Crab (M+V)	0.9	0.28	-	-	3.3	2.6	-	-
PSR	0.9	0.28	-	-	3.2	2.8	-	-
AGN	3.0	1.1	2.7	1.0	10.6	8.3	10.1	7.8
AGN+PSR	3.1	1.2	2.8	1.1	10.4	8.5	9.9	8.1
GRB+PSR	8.3	4.0	5.0	2.6	9.6	8.1	6.4	5.8
GRB+AGN	8.7	4.1	5.6	2.8	12.2	9.3	10.7	8.0
All combined	8.7	4.0	5.7	2.8	12.0	9.2	10.3	8.2

Table 7.7: 95% CL limits obtained for individual objects and combinations for the superluminal case.

7.6.2 Subluminal vs. superluminal

A notable difference between the subluminal and superluminal limits is expected when the λ_n^{rec} distribution is highly asymmetric, which is in turn provoked by a highly asymmetric light curve. For most sources, the light curve distribution is not asymmetric enough for the two limits to be sensibly different. Figure 7.7 gives a representation of the ratio between the two limits $E_{QG,n}^{\text{sub}}/E_{QG,n}^{\text{super}}$ for all possible cases. The difference between the limits tends to be much higher when systematic uncertainties are not accounted for. Therefore, propagating them to the profile log-likelihood tends to symmetrise the reconstructed λ_n distribution and blur the difference between the two cases.

Looking at results without systematic uncertainties (blue data), it appears GRB 190114C is the source that yields the most noteworthy difference in the results for both cases. While other sources may show a difference of usually less than 10% and should fall within the uncertainty on the limit, a 10 to 50% decrease is necessary to go from the subluminal to the superluminal limits yielded by GRB 190114C or combinations including this source. Even though this difference is suppressed by the introduction of systematic uncertainties, the ratio $E_{QG,n}^{\text{sub}}/E_{QG,n}^{\text{super}}$ stays the largest when the GRB is part of the studied sample.

A recent publication from the large high altitude air shower observatory[4] (LHAASO) collaboration [107] has possibly excluded the possibility of superluminal effects. Indeed they were able to estimate the quantum gravity energy scale at linear order ($n = 1$) for the superluminal effect to be larger than $E_{QG,1} = 1.42 \times 10^{24}$ GeV, that is to say 5 orders of magnitude larger than the Planck energy. We however thought it to be interesting to point out the differences between the two effects.

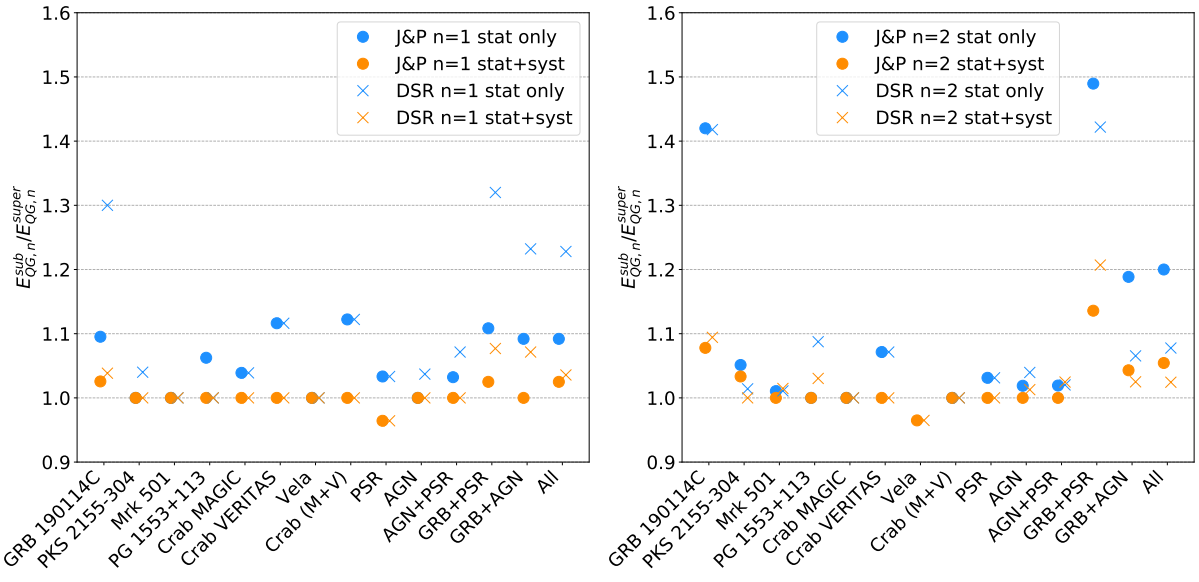

(a) J&P approach.

(b) DSR approach.

Figure 7.7: Limits on $E_{QG,n}$: comparison between subluminal and superluminal cases with and without systematics.

[4] Observatory based in China and in operation since 2019. The detection relies on water pools rather than telescopes.

7.6.3 Systematic uncertainties

Continuing with systematics, Figure 7.8 shows a representation of the subluminal limits obtained with and without systematic uncertainties for all the different cases. In most cases, accounting for systematic uncertainties brings down the upper limit such that $E^{\text{Syst}}_{QG,n}/E^{\text{NoSyst}}_{QG,n} \sim 2$. The same behaviour is observed in the superluminal case. Furthermore, much like it was discussed for lag-distance models, we sometimes do observe $E^{\text{Syst}}_{QG,n} < E_P$ while $E^{\text{NoSyst}}_{QG,n} > E_P$. It is therefore of great importance to perform a thorough treatment of systematics in order to provide a correct interpretation of the results.

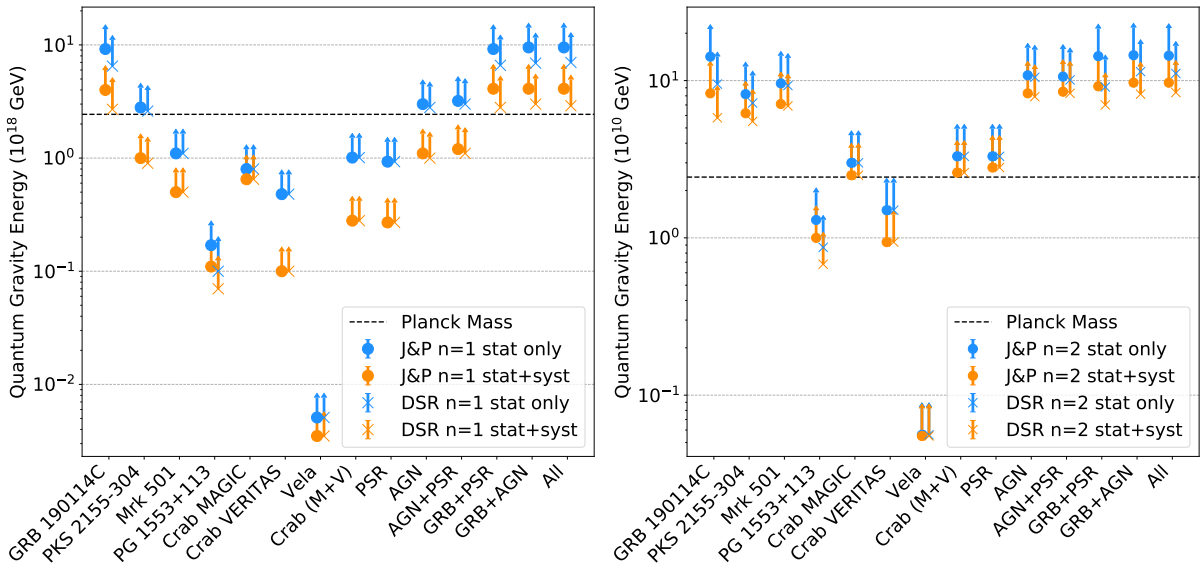

(a) Linear order $n = 1$

(b) Quadratic order $n = 2$

Figure 7.8: Limits on $E_{QG,n}$: comparison with and without systematic uncertainties for the two lag-distance formalisms (subluminal only).

7.6.4 Lag-distance models

Regarding the lag-distance formalisms, yet another representation of the limits presenting them as function of the redshift is given in Figure 7.9 at linear and quadratic orders for the two models. In accordance with what can be observed in Figure 7.4, differences in the limits get larger as the redshift of test sources increases. Since $\kappa_n^{J\&P}(z)$ grows faster than $\kappa_n^{DSR}(z)$, the J&P model tends to emphasise the impact of large redshift sources. Combinations therefore yield similar limits to individual sources analyses as can be verified in Tables 7.6 and 7.7. Conversely, the DSR model tends to balance all sources contribution such that combinations yield significantly higher limits on $E_{QG,n}$.

7.6.5 Comparison with older published limits (subluminal)

The limits obtained in this work together with the ones found in older publications are shown in Figure 7.10. Overall, there appears to be a good agreement between the results found with our simulations and the ones obtained in previous analyses with actual data. We can therefore safely assume the simulated data sets are consistent with the actual data and correctly reproduce them.

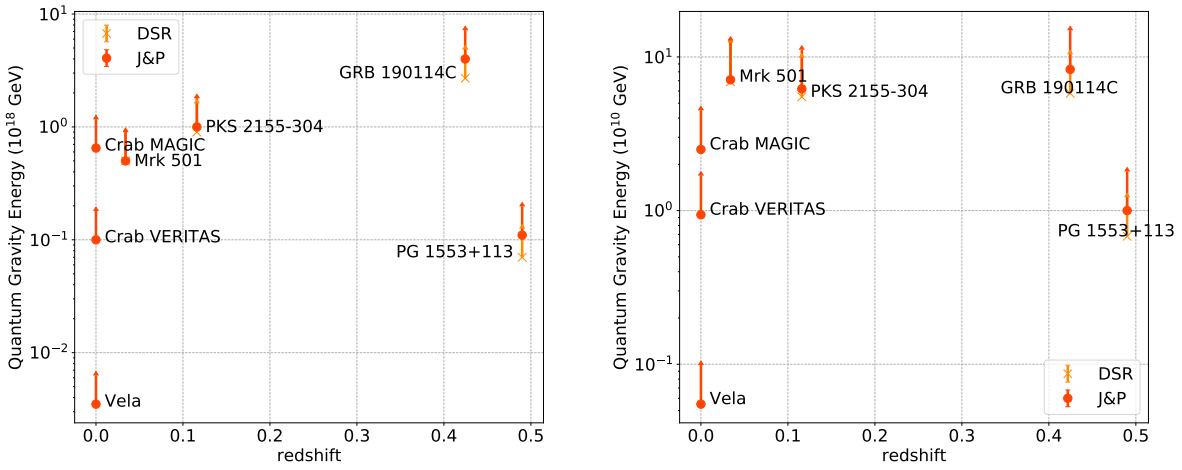

(a) Linear order $n = 1$

(b) Quadratic order $n = 2$

Figure 7.9: Limits on $E_{QG,n}$: comparison between the J&P and DSR formalisms for the two correction orders (subluminal only).

The observed differences can then be explained by various factors. Amongst them, we have that the reconstructed λ_n^{rec} is built as the mean of a distribution containing a thousand points (from the thousand Monte-Carlo simulations) while previous studies had only one measured light curve and one reconstructed λ_n^{rec}. The difference can also be explained by the evaluation methods of systematic uncertainties which vary from one analysis to the other, but also of the IRFs which are fully taken into account in this work while they were often approximated as a constant of energy in previous analyses for a simpler treatment[5].

7.7 Summary and perspective

We have presented a newly developed standard method aimed at paving the way for future multi-instrument population studies for LIV time-of-flight searches. We have introduced the underlying technique, the maximum likelihood method, and how it was adapted to a multi-source analysis with the combination strategy. A particular care has been given to the background, instrument response and uncertainty treatment. Moreover, two distinct lag-distance approaches, J&P and DSR, have been tested and confronted for the first time in this work. The method has been tested and calibrated with a representative selection of seven sources - one GRB, three AGNs and three pulsars - that were previously analysed. Upper limits on the quantum gravity energy scale E_{QG} have been derived for all individual sources and a relevant set of combinations. Several aspects have been tested:

- The limits obtained for individual sources are comparable to the ones obtained in previous publications suggesting a correct calibration of the method.

[5]This approximation was justified by the fact the effective area was mostly constant on the considered energy range.

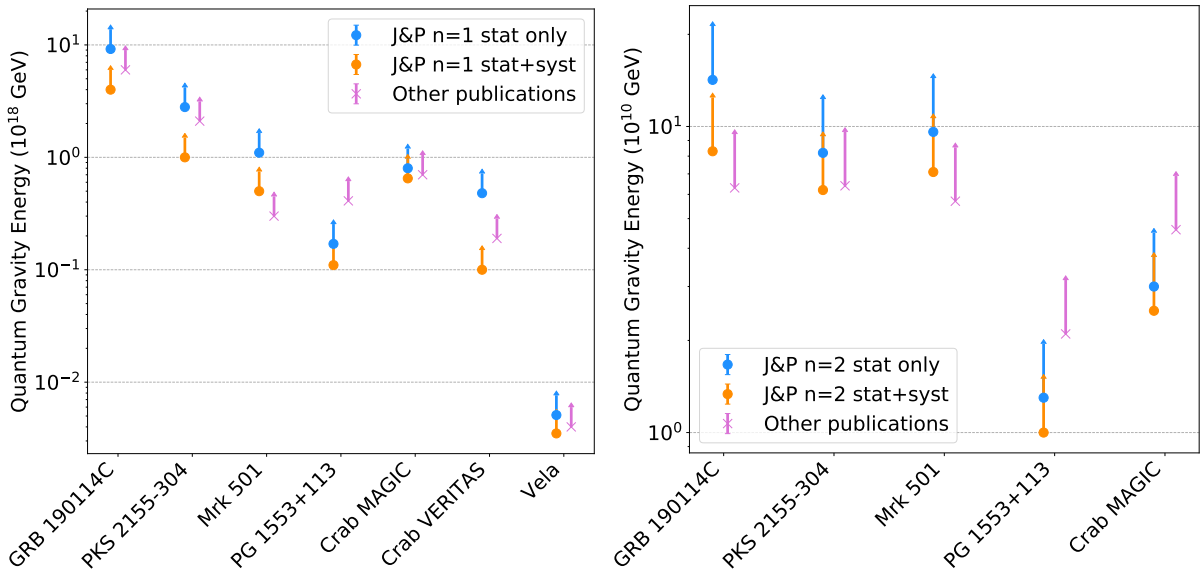

(a) Linear order $n = 1$

(b) Quadratic order $n = 2$

Figure 7.10: Limits on $E_{QG,n}$: comparison with limits yielded in previous analyses for the two correction orders. No limits at the quadratic order were provided in the Crab (VERITAS) and Vela pulsars publications, hence the missing data points in plot (b).

- Combinations appear to be dominated by the most stringent individual source in the tested sample, but still improve the limit obtained on E_{QG}.
- The lag-distance models impose different "power relationships" between sources, either emphasising or balancing sources contributions. The former leads to combinations that yield similar limits than individual sources, while the latter leads combinations to yield limits significantly improved as compared to individual sources.
- Systematic uncertainties bring down the limits by a factor two and tend to harmonise the limits between the superluminal and subluminal scenarii, hence the importance of accurately treating them for a proper interpretation of the results.

The next step will be to adapt the software to the actual data format used by experiments. This will allow to apply this method on all usable data (previously analysed or not) from H.E.S.S., MAGIC, VERITAS, and possibly Fermi to yield much stronger upper limits on the quantum gravity energy scale E_{QG}. The software could also be easily adapted to test other lag-distance models provided by different theoretical approaches. Similarly to what has been attempted in Chapter 5, the software could be extended to test the modifications of the EBL absorption of gamma-rays induced by LIV effects. Finally, although it was not performed in this study, it would be very interesting to test models of intrinsic delays and estimate their impact on limits obtained from combinations.

Conclusion

The work presented in this manuscript is centered on energy-dependent time delays, arising as one of the most explored signatures of Lorentz invariance violation (LIV). Intrinsic time delays generated by sources radiative processes interfere with these studies and need to be properly disentangled. It is indeed necessary to accurately discriminate and gauge each contribution to the detected time delays to provide a legitimate constraint on the energy scale E_{QG}, and thus a proper interpretation on the tested quantum gravity models. We have discussed two generic and complementary approaches for discrimination purposes: source modeling and population study.

The first approach is adressed with a time dependent modeling of blazars relying on a standard scenario involving one zone of leptonic plasma governed by synchrotron-self-Compton processes. Energy-dependent time delays appear to be easily generated from such a model. A study on individual model parameters revealed that distributions of time delays as function of energy follow three specific regimes related to the high energy leptonic population evolution. These regimes are associated to trends - increasing, decreasing, flat - that can be explained from the competition between acceleration and radiative processes. The scenario was then extended to adiabatic and external processes. The associated time delay distributions followed the same three regimes and could still be fully explained by the competition between processes. The detectability of non-zero intrinsic delays with IACTs, tested for an archetypal source, seem to require flaring episodes with a variation of physical quantities that are substantial but still realistic. The lack of detectable time delays in actual observations could be explained by the fact that multiple physical quantities vary simultaneously and could cancel their respective influence. A more realistic explanation is that standard flare models need to be reconsidered. A natural extent of this study would then focus on the effect brought on intrinsic delays by a simultaneous variation of several parameters. The model could also be improved by extending it to hadronic processes or transition to a two-zone model.

We also performed a multi-frequency study which highlighted a strong correlation and symmetry between time delays in the X-ray (unaffected by LIV) and gamma-ray (where LIV effects could arise) energy domains. The measurement of the euclidian distance between the low and high energy time delay distributions helps quantify this correlation. Furthermore, it may hold a predicting power: deduce intrinsic delays in the gamma-ray energies from the detection and study of delays in the X-ray domain. The introduction of LIV effects in the simulations leads to a significant break of the symmetry between the X-ray and gamma-ray domains, thus leading to higher values of the euclidian distance. We have identified for the first time a threshold on the euclidian distance above which time delays can no longer be explained by intrinsic effects in a pure SSC scenario, and strongly suggests the presence of externally-induced time delays. The next step would be to perform this study with an improved version of the euclidian distance method, namely the dynamic time warping (usually referred as DTW). A complementary study

is also performed with hardness-intensity diagrams built from spectral energy distributions which show hysteresis patterns. Similarly to the euclidian distance, hysteresis loop orientation can help identify the presence of non-intrinsic time delays. Finally, another phenomenology effect, namely the modification of kinematic interactions and in particular between gamma-rays and the EBL, was qualitatively and simultaneously tested through extreme models of EBL absorption. It appeared intrinsic time delays behaviour would not be significantly affected by the LIV-modified EBL absorption. As the Klein-Nishina effect and the modification of EBL absorption do not break the delays symmetry, we should be able to quantify the discrepancies and discriminate between intrinsic and LIV contributions to the observed time delays with this method.

Regarding the second approach, namely the population study, this work aims at preparing LIV time-of-flight searches that are to be performed with instruments from current generation (H.E.S.S., MAGIC, VERITAS, Fermi, etc.) or future generations like CTA. An analysis software (*LIVelihood*) based on a maximum likelihood estimation has been developed to provide a standardised combination method. The method was carefully tested and calibrated using simulated datasets based on several representative sources observed at TeV energies that had been analysed in previous LIV studies. A consortium between H.E.S.S., MAGIC and VERITAS experiments has been created to enlarge the catalog of usable datasets that are to be combined in this multi-source analysis. For this work, a total of seven sources are used: one gamma-ray burst, three blazars and three pulsars. The multi-instrument and multi-source strategy - anticipating CTA operations - required a careful treatment of the background, instrument responses and systematics. Moreover, two lag-distance models are used and compared for the first time.

The attention to details and the will to avoid any approximations in the computation brought a complex model that required optimisation. A tabulation strategy was implemented in order to reduce the computational load and bring down the numerical analysis duration to a few hours. Furthermore, a careful calibration was performed to assess the method performances and correct eventual issues leading to erroneous results. The upper limits on the energy scale E_{QG} obtained for individual sources are comparable to the ones obtained in previous publications suggesting a correct calibration of the method. Results show that combinations are dominated by the most stringent individual source in the tested sample, but still improve the limit obtained on E_{QG}. The lag-distance models impose different "power relationships" between sources. One model tends to emphasise the most stringent source contribution such that combinations yield similar limits than individual sources analyses. The second model on the other hand tends to balance all sources contribution such that combinations yield significantly higher limits on E_{QG}. The systematics appear to bring down the limits by a factor two, pointing out the importance of an accurate treatment of the uncertainties for a proper interpretation of the results. Moreover, systematic uncertainties tend to harmonise the limits obtained between the superluminal and subluminal scenarii. The next step will be to use this method on all usable data (previously analysed or not) from H.E.S.S., MAGIC, VERITAS, and possibly Fermi to yield much stronger upper limits on the quantum gravity energy scale. The software could also be easily adapted to test other lag-distance models, to perform a combined search for time delay and LIV-induced modifications of high energy spectra, or to test models of intrinsic delays.

The advent of the Cherenkov telescope array (CTA) will certainly help improve the current state of this study. The announced improvement on the source monitoring, attainable energies, and data quality should help both approaches on the question of discriminating intrinsic energy-dependent time delays from LIV-induced ones. Indeed, it should provide a larger number of

usable data sets for LIV searches, detected at higher fluxes, with higher energies and allow to detect sources at larger redshift. It will also provide more precise emission spectra which will help constraining source models that are currently in use.

Appendix A

Solution of the time dependent SSC differential equation

The general solution of Equation 4.21 was derived by Katarzynski et al. [71, 76]. For leptons of energy γ distributed along a broken power law, the solution takes the following form:

$$N^*(\gamma,t) = \left[N_0 S_1(\gamma,t)^{-n} - \frac{N_0 \gamma_{\rm cut}^{n-2}}{S_1(\gamma,t)^2}\right] S_2(\gamma,t). \tag{A.1}$$

N_0 is the initial lepton density, n and $\gamma_{\rm cut}$ are the index and break value of the broken power law. S_1 and S_2 are defined as follows:

$$S_1(\gamma,t) = [I_1(t) - \gamma I_2(t)]\,\gamma; \tag{A.2}$$

$$S_2(\gamma,t) = \exp\left[\int_{t_0}^{t} dt' \, \frac{\gamma C^{\rm aa}(t') I_2(t') - \gamma C^{\rm aa}(t') I_2(t) + C^{\rm aa}(t') I_1(t) - 2 I_1(t') C^{\rm cool}(t')}{\gamma I_2(t') - \gamma I_2(t) + I_1(t)}\right]. \tag{A.3}$$

For simplicity, the processes coefficients $C(x)$ are parametrised as follows:

$$C^{\rm aa}(x) = C^{\rm acc}(x) - C^{\rm adia}(x) = \frac{A}{x^{m_a}} - \frac{m_r}{x}; \tag{A.4}$$

$$C^{\rm cool}(x) = C^{\rm ssc}(x) + C^{\rm eic} = \frac{B}{x^{m_b}} + E \tag{A.5}$$

with A, B, C, E constant scalars associated to acceleration, SSC cooling and EIC cooling processes respectively. m_a, m_b and m_r are the acceleration, SSC cooling and adiabatic evolution rates. Finally, the integrals I_1 and I_2 are defined as follows:

$$I_1(t) = \exp\left[\int_{t_0}^{t} C^{\rm aa}(x) dx\right]; \tag{A.6}$$

$$I_2(t) = \int_{t_0}^{t} C^{\rm cool}(x) I_1(x) dx. \tag{A.7}$$

Let us now derive the analytical expressions of these two integrals which will define the validity domain for model parameters. Depending on the value of m_a (either $m_a = 1$ or $m_a \neq 1$) the solution will take a different form.

Derivation for the $m_a = 1$ case

In the case where $m_a = 1$, Equation A.6 and A.7 derivation is straightforward. The most generic expressions (including adiabatic and EIC processes) read:

$$\begin{aligned} I_1(y) &= \exp\left[\int_{t_0}^{y} dt\ \left(\frac{A}{t} - \frac{m_r}{t}\right)\right] \\ &= \exp\left[A(\log y - \log t_0) - m_r(\log y - \log t_0)\right] \\ &= y^{A-m_r} - t_0^{m_r-A}; \end{aligned} \tag{A.8}$$

$$\begin{aligned} I_2(x) &= \int_{t_0}^{x} dy\ \left(E + Cy^{-m_b}\right)\left(y^{A-m_r} - t_0^{A-m_r}\right) \\ &= t_0^{m_r-A}\left[\int_{t_0}^{x} dy\ Ey^{A-m_r} + \int_{t_0}^{x} dy\ Cy^{A-m_r-m_b}\right] \\ &= t_0^{m_r-A}\left[\frac{E}{1+A-m_r}\left(x^{1+A-m_r} - t_0^{1+A-m_r}\right) + \frac{C}{1+A-m_r-m_b}\left(x^{1+A-m_r-m_b} - t_0^{1+A-m_r-m_b}\right)\right]. \end{aligned} \tag{A.9}$$

The pure SSC model with no adiabatic effect is recovered by setting $m_r = 0$ and $E = 0$.

Derivation for the $m_a \neq 1$ case

In the case where $m_a \neq 1$, the derivation of Equation A.6 and A.7 is more complex and requires to use tricks. Let's start again with the base expressions:

$$\begin{aligned} I_1(y) &= \exp\left[\int_{t_0}^{y} dt\ \left(\frac{A}{t^{m_a}} - \frac{m_r}{t}\right)\right] \\ &= \exp\left[\frac{A}{1-m_a}\left(y^{1-m_a} - t_0^{1-m_a}\right) - m_r\left(\log y - \log t_0\right)\right] \\ &= t_0^{m_r} y^{-m_r} \exp\left[\frac{At_0^{1-m_a}}{m_a - 1}\right] \exp\left[\frac{Ay^{1-m_a}}{1-m_a}\right]; \end{aligned} \tag{A.10}$$

$$\begin{aligned} I_2(x) &= \int_{t_0}^{x} dy\ \left(E + Cy^{-m_b}\right) t_0^{m_r} y^{-m_r} \exp\left[\frac{At_0^{1-m_a}}{m_a-1}\right] \exp\left[\frac{Ay^{1-m_a}}{1-m_a}\right] \\ &= t_0^{m_r} \exp\left[\frac{At_0^{1-m_a}}{m_a-1}\right] E \int_{t_0}^{x} dy\ y^{-m_r} \exp\left[\frac{Ay^{1-m_a}}{1-m_a}\right] \quad (1) \\ &+ t_0^{m_r} \exp\left[\frac{At_0^{1-m_a}}{m_a-1}\right] C \int_{t_0}^{x} dy\ y^{-m_r-m_b} \exp\left[\frac{Ay^{1-m_a}}{1-m_a}\right], \quad (2) \end{aligned} \tag{A.11}$$

with (1) and (2) the parts of the solution associated to EIC and SSC processes respectively.

We will now focus on part (2) of Equation A.11. We perform a change of variable:

$$X = \frac{Ay^{1-m_a}}{m_a - 1} \quad \Longleftrightarrow \quad y = \left[\frac{X(m_a-1)}{A}\right]^{\frac{1}{1-m_a}}, \tag{A.12}$$

with

$$\frac{dy}{dX} = \left[\frac{m_a-1}{A}\right]^{\frac{1}{1-m_a}} \frac{1}{1-m_a} X^{\frac{1}{1-m_a}-1} \tag{A.13}$$

and

$$\begin{cases} t_0 \longrightarrow t_0' = \frac{At_0^{1-m_a}}{m_a-1} \\ \\ x \longrightarrow x' = \frac{Ax^{1-m_a}}{m_a-1}. \end{cases} \tag{A.14}$$

We therefore have:

$$\begin{aligned} (2) &= \frac{t_0^{m_r}}{1-m_a} \exp\left[\frac{At_0^{1-m_a}}{m_a-1}\right] C \int_{t_0'}^{x'} dX \, \exp^{-X} \left[\frac{X(m_a-1)}{A}\right]^{\frac{-m_r-m_b}{1-m_a}} \left[\frac{m_a-1}{A}\right]^{\frac{1}{1-m_a}} X^{\frac{1}{1-m_a}-1} \\ &= \frac{Ct_0^{m_r}}{1-m_a} \exp\left[\frac{At_0^{1-m_a}}{m_a-1}\right] \left[\frac{m_a-1}{A}\right]^{\frac{1-m_r-m_b}{1-m_a}} \times \int_{t_0'}^{x'} dX \, \exp^{-X} X^{\frac{1-m_r-m_b}{1-m_a}-1}. \end{aligned} \tag{A.15}$$

That last integral is an incomplete gamma function denoted $I_{\gamma,i}$ which generic expression reads

$$I_{\gamma,i}(a,x) = \int_x^{\infty} dt \, \exp^{-t} t^{a-1} = \Gamma(a) - \int_0^x dt \, \exp^{-t} t^{a-1}, \tag{A.16}$$

with $\Gamma(a)$ the standard gamma function. This integral is defined only for the following conditions:

$$\begin{cases} x > 0 \\ a > 0. \end{cases} \tag{A.17}$$

This means we have

$$\begin{aligned} \int_{t_0'}^{x'} dX \, \exp^{-X} X^{\frac{1-m_r-m_b}{1-m_a}-1} &= I_{\gamma,i}\left(\frac{1-m_r-m_b}{1-m_a}, X\right) \\ &= I_{\gamma,i}\left(\frac{1-m_r-m_b}{1-m_a}, \frac{Ay^{1-m_a}}{m_a-1}\right) \end{aligned} \tag{A.18}$$

with the following necessary conditions:

$$\begin{cases} \frac{1-m_r-m_b}{1-m_a} > 0 \\ \\ \frac{Ay^{1-m_a}}{m_a-1} > 0. \end{cases} \tag{A.19}$$

Similarly, we can show that

$$(1) = \frac{Et_0^{m_r}}{1-m_a} \exp\left[\frac{At_0^{1-m_a}}{m_a-1}\right] \left[\frac{m_a-1}{A}\right]^{\frac{1-m_r}{1-m_a}} \times I_{\gamma,i}\left(\frac{1-m_r}{1-m_a}, \frac{Ay^{1-m_a}}{m_a-1}\right). \tag{A.20}$$

with the following necessary conditions:

$$\begin{cases} \frac{1-m_r}{1-m_a} > 0 \\ \\ \frac{Ay^{1-m_a}}{m_a-1} > 0. \end{cases} \tag{A.21}$$

Finally, we have

$$I_2(x) = (2) \tag{A.22}$$

when only SSC processes are accounted for, or

$$I_2(x) = (1) + (2) \tag{A.23}$$

when both SSC and EIC processes are accounted for. On the other hand, adiabatic effects can be neglected by simply setting $m_r = 0$.

Along with the necessary conditions for the incomplete gamma functions to be well defined, other conditions arise for the denominators to be non-zero. Either way, these conditions are changed by adiabatic and EIC processes. More precisely, the conditions are more constraining when these processes are introduced. A summary of these conditions is given in Section 4.1.1.3.

Appendix B

Convergence and calibration plots produced with the *LIVelihood* software

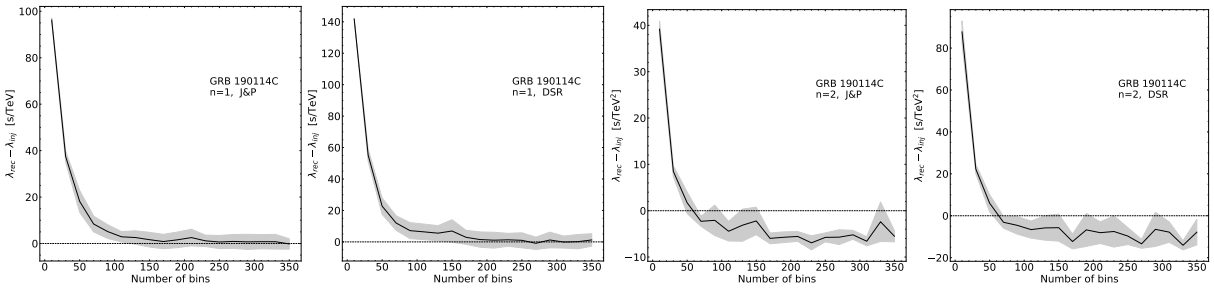

(a) GRB 190114C $n = 1$, J&P. (b) GRB 190114C $n = 1$, DSR. (c) GRB 190114C $n = 2$, J&P. (d) GRB 190114C $n = 2$, DSR.

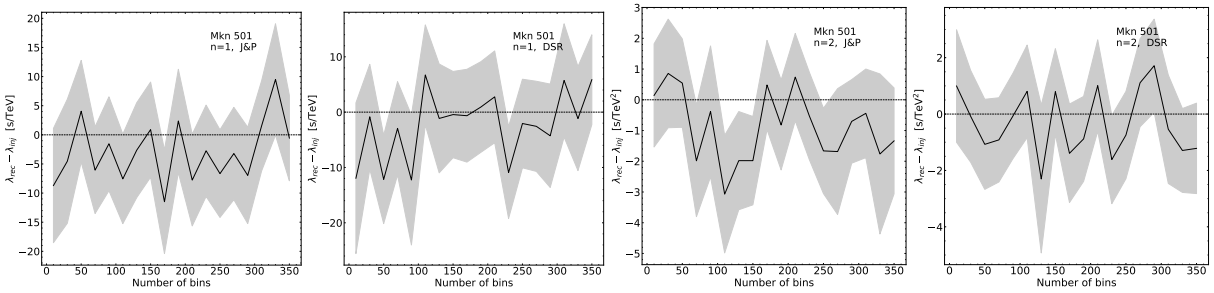

(e) Mkn 501 $n = 1$, J&P. (f) Mkn 501 $n = 1$, DSR. (g) Mkn 501 $n = 2$, J&P. (h) Mkn 501 $n = 2$, DSR.

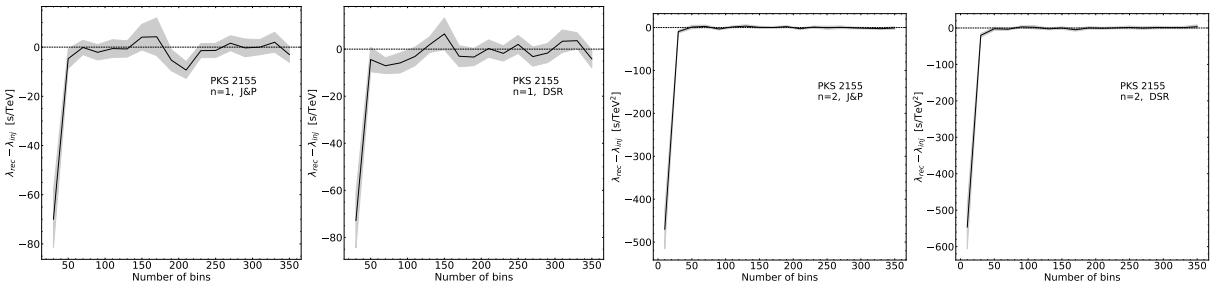

(i) PKS 2155-304 $n = 1$, J&P. (j) PKS 2155-304 $n = 1$, DSR. (k) PKS 2155-304 $n = 2$, J&P. (l) PKS 2155-304 $n = 2$, DSR.

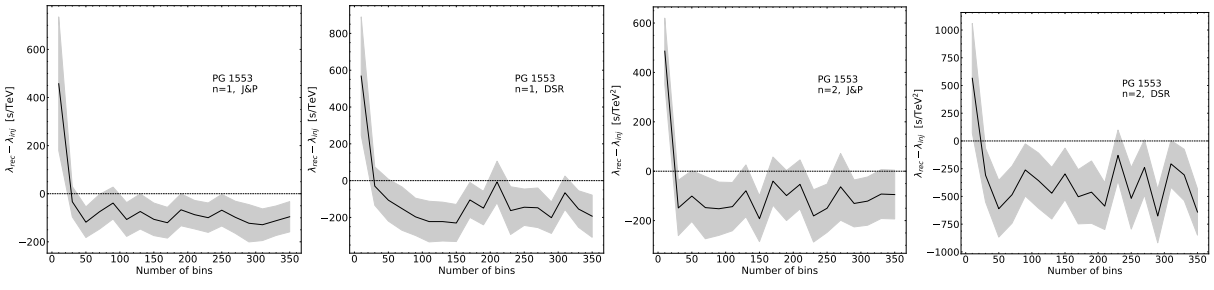

(m) PG 1553+113 $n = 1$, J&P. (n) PG 1553+113 $n = 1$, DSR. (o) PG 1553+113 $n = 2$, J&P. (p) PG 1553+113 $n = 2$, DSR.

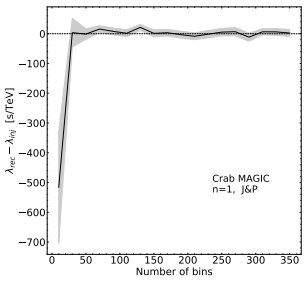

(q) Crab (MAGIC) $n = 1$, J&P.

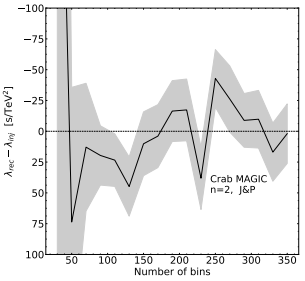

(r) Crab (MAGIC) $n = 2$, J&P.

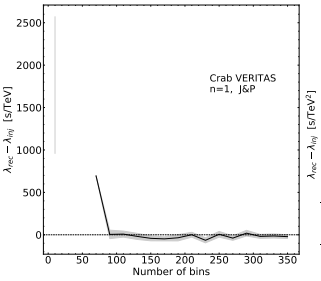

(s) Crab (VERITAS) $n = 1$, J&P.

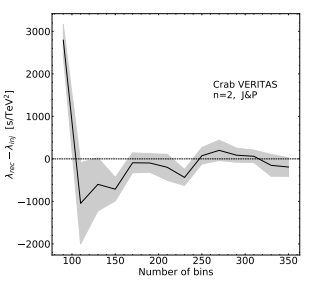

(t) Crab (VERITAS) $n = 2$, J&P.

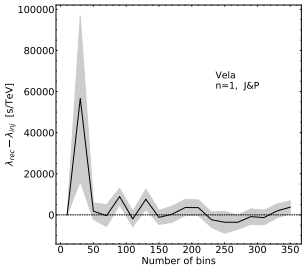

(u) Vela $n = 1$, J&P.

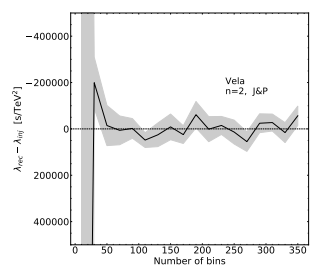

(v) Vela $n = 2$, J&P.

Figure B.1: Convergence plots for all individual sources. Note the y axis boundaries are different in each case. The small offsets present after convergence in some cases are absorbed in the uncertainty enveloppe (gray) when accounting for IRFs.

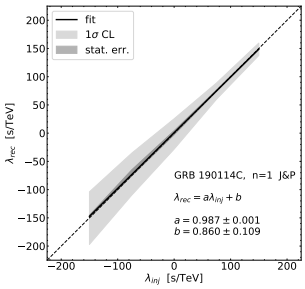

(a) GRB 190114C $n = 1$, J&P.

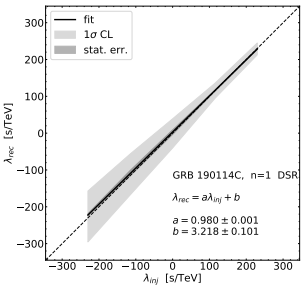

(b) GRB 190114C $n = 1$, DSR.

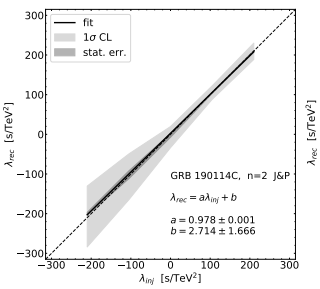

(c) GRB 190114C $n = 2$, J&P.

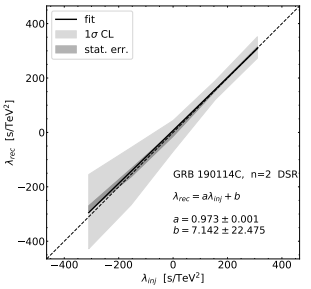

(d) GRB 190114C $n = 2$, DSR.

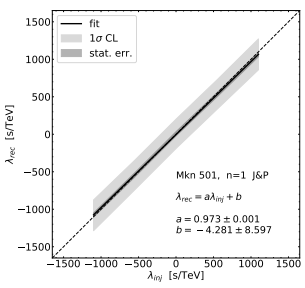

(e) Mkn 501 $n = 1$, J&P.

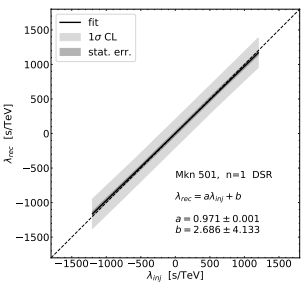

(f) Mkn 501 $n = 1$, DSR.

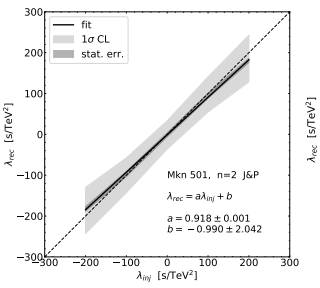

(g) Mkn 501 $n = 2$, J&P.

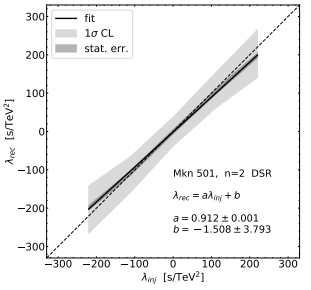

(h) Mkn 501 $n = 2$, DSR.

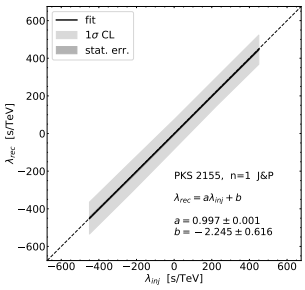

(i) PKS 2155-304 $n = 1$, J&P.

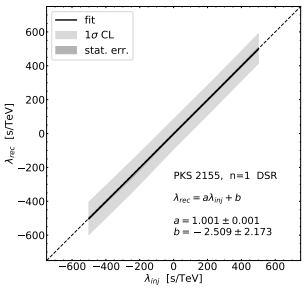

(j) PKS 2155-304 $n = 1$, DSR.

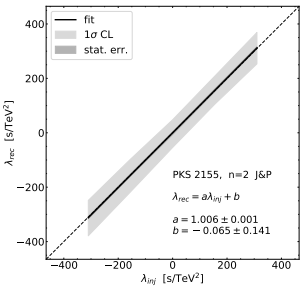

(k) PKS 2155-304 $n = 2$, J&P.

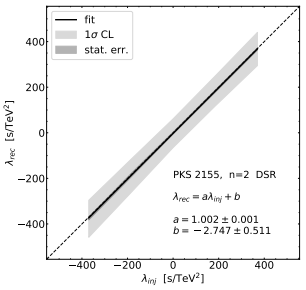

(l) PKS 2155-304 $n = 2$, DSR.

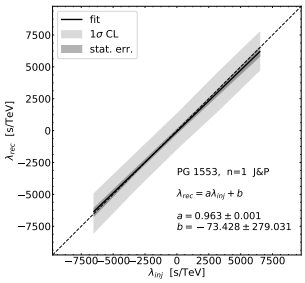

(m) PG 1553+113 $n = 1$, J&P.

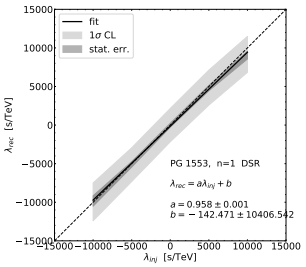

(n) PG 1553+113 $n = 1$, DSR.

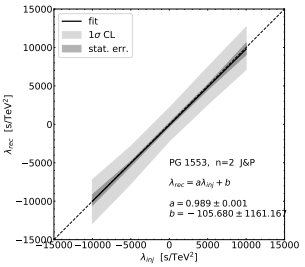

(o) PG 1553+113 $n = 2$, J&P.

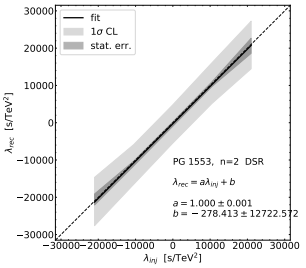

(p) PG 1553+113 $n = 2$, DSR.

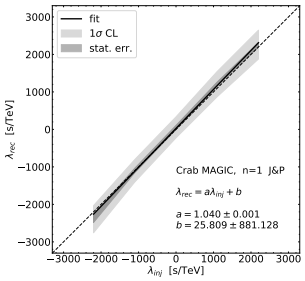

(q) Crab (MAGIC) $n = 1$, J&P.

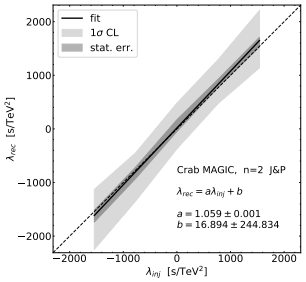

(r) Crab (MAGIC) $n = 2$, J&P.

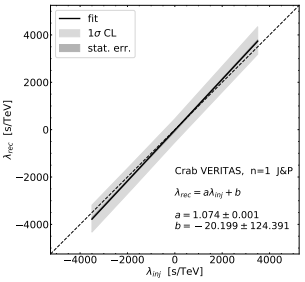

(s) Crab (VERITAS) $n = 1$, J&P.

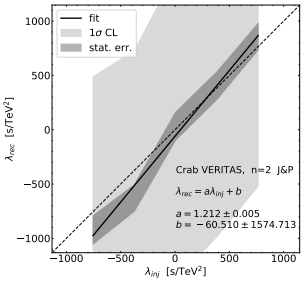

(t) Crab (VERITAS) $n = 2$, J&P.

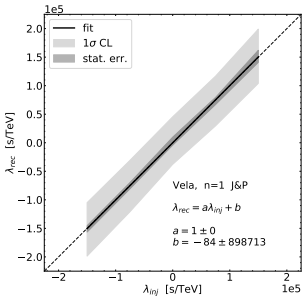

(u) Vela $n = 1$, J&P.

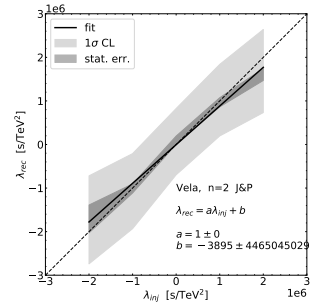

(v) Vela $n = 2$, J&P.

Figure B.2: Calibration plots for all individual sources. Note the y axis boundaries are different in each case.

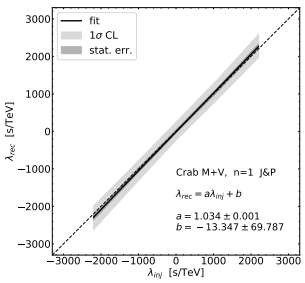

(a) Crab M + V
$n = 1$, J&P.

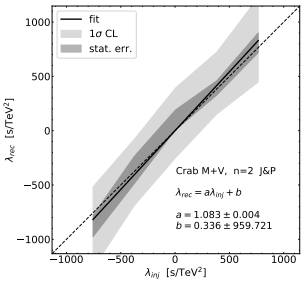

(b) Crab M + V
$n = 2$, J&P.

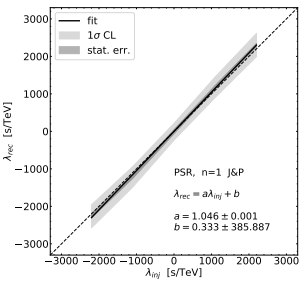

(c) PSR
$n = 1$, J&P.

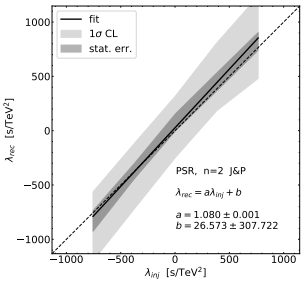

(d) PSR
$n = 2$, J&P.

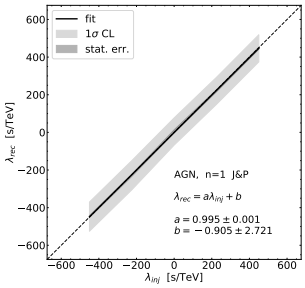

(e) AGN
$n = 1$, J&P.

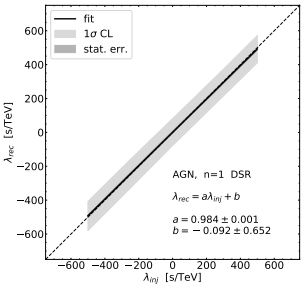

(f) AGN
$n = 1$, DSR.

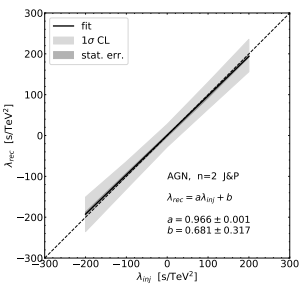

(g) AGN
$n = 2$, J&P.

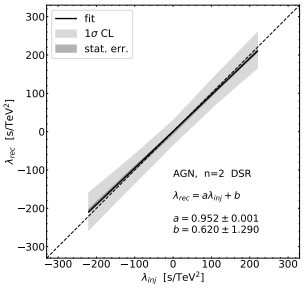

(h) AGN
$n = 2$, DSR.

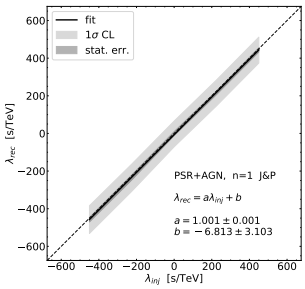

(i) AGN + PSR
$n = 1$, J&P.

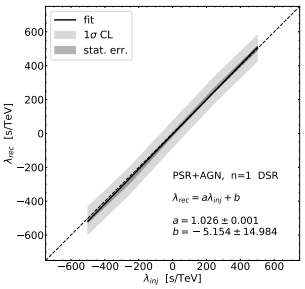

(j) AGN + PSR
$n = 1$, DSR.

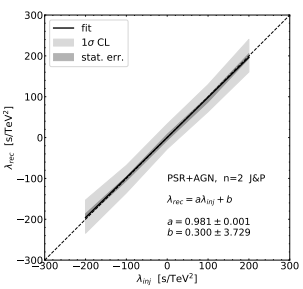

(k) AGN + PSR
$n = 2$, J&P.

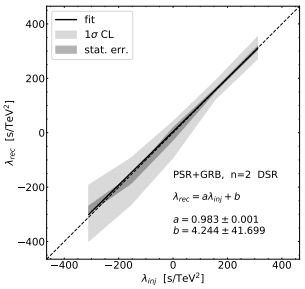

(l) AGN + PSR
$n = 2$, DSR.

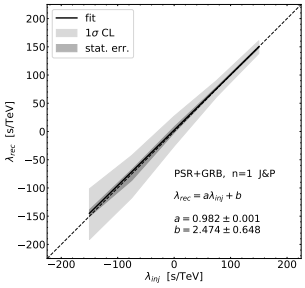

(m) GRB + PSR
$n = 1$, J&P.

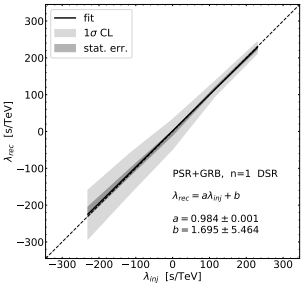

(n) GRB + PSR
$n = 1$, DSR.

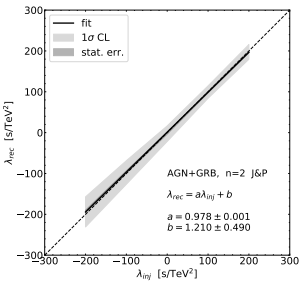

(o) GRB + PSR
$n = 2$, J&P.

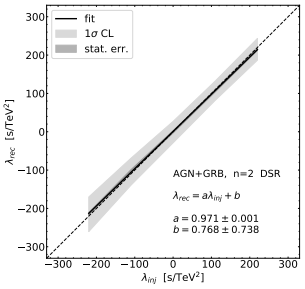

(p) GRB + PSR
$n = 2$, DSR.

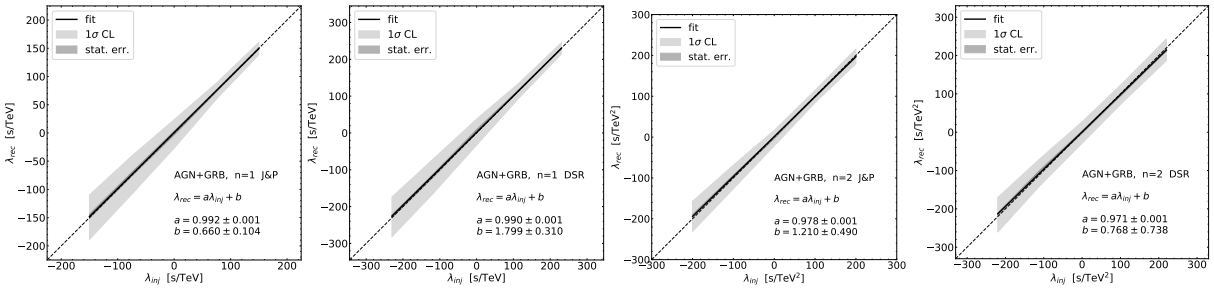

(q) GRB + AGN $n = 1$, J&P.

(r) GRB + AGN $n = 1$, DSR.

(s) GRB + AGN $n = 2$, J&P.

(t) GRB + AGN $n = 2$, DSR.

(u) All sources $n = 1$, J&P.

(v) All sources $n = 1$, DSR.

(w) All sources $n = 2$, J&P.

(x) All sources $n = 2$, DSR.

Figure B.3: Calibration plots for various combinations. Note the y axis boundaries are different in each case.

Bibliography

[1] B. P. Abbott, R. Abbott, T. D. Abbott, *et al.*, *Observation of Gravitational Waves from a Binary Black Hole Merger*, Phys. Rev. Lett.**116** (Feb., 2016) Feb. 061102, arXiv:1602.03837 [gr-qc].

[2] G. Aad, T. Abajyan, B. Abbott, *et al.*, *Observation of a new particle in the search for the Standard Model Higgs boson with the ATLAS detector at the LHC*, Physics Letters B **716** (Sept., 2012) Sept. 1–29, arXiv:1207.7214 [hep-ex].

[3] S. Chatrchyan, V. Khachatryan, A. M. Sirunyan, *et al.*, *Observation of a new boson at a mass of 125 GeV with the CMS experiment at the LHC*, Physics Letters B **716** (Sept., 2012) Sept. 30–61, arXiv:1207.7235 [hep-ex].

[4] C. Rovelli, *Strings, loops and others: a critical survey of the present approaches to quantum gravity*, arXiv e-prints (Mar., 1998) Mar. gr–qc/9803024, arXiv:gr-qc/9803024 [gr-qc].

[5] D. Vaid, *Quantum Gravity for Dummies*, arXiv e-prints (Feb., 2014) Feb. arXiv:1402.2757, arXiv:1402.2757 [physics.pop-ph].

[6] N. Bodendorfer, *An elementary introduction to loop quantum gravity*, arXiv e-prints (July, 2016) July arXiv:1607.05129, arXiv:1607.05129 [gr-qc].

[7] K. Wray, *An introduction to String Theory*, https://math.berkeley.edu/~kwray/papers/string_theory.pdf.

[8] A. Ashtekar and E. Bianchi, *A short review of loop quantum gravity*, Reports on Progress in Physics **84** (Apr., 2021) Apr. 042001, arXiv:2104.04394 [gr-qc].

[9] J. Aastrup and J. M. Grimstrup, *Intersecting Quantum Gravity with Noncommutative Geometry - a Review*, SIGMA **8** (Mar., 2012) Mar. 018, arXiv:1203.6164 [gr-qc].

[10] M. Reuter and F. Saueressig, *Quantum Einstein gravity*, New Journal of Physics **14** (May, 2012) May 055022, arXiv:1202.2274 [hep-th].

[11] D. Oriti, *The microscopic dynamics of quantum space as a group field theory*, arXiv e-prints (Oct., 2011) Oct. arXiv:1110.5606, arXiv:1110.5606 [hep-th].

[12] R. Loll, *Quantum gravity from causal dynamical triangulations: a review*, Classical and Quantum Gravity **37** (Jan., 2020) Jan. 013002, arXiv:1905.08669 [hep-th].

[13] A. Addazi, J. Alvarez-Muniz, R. Alves Batista, *et al.*, *Quantum gravity phenomenology at the dawn of the multi-messenger era – A review*, arXiv e-prints (Nov., 2021) Nov. arXiv:2111.05659, arXiv:2111.05659 [hep-ph].

[14] D. Boubaa, G. Faisel, and S. Khalil, *Beyond SM Physics and searches for SUSY at the LHC*, arXiv e-prints (May, 2020) May arXiv:2005.08069, arXiv:2005.08069 [hep-ph].

[15] J. Khoury, B. A. Ovrut, P. J. Steinhardt, and N. Turok, *Ekpyrotic universe: Colliding branes and the origin of the hot big bang*, Phys. Rev. D**64** (Dec., 2001) Dec. 123522, arXiv:hep-th/0103239 [hep-th].

[16] R. Lehnert, *The Lorentz violating extension of the standard model*, in *4th International Conference on Physics Beyond the Standard Model: Beyond the Desert (BEYOND 03)*, pp. 179–193. 1, 2004. arXiv:hep-ph/0401124.

[17] J. Ellis, N. E. Mavromatos, and D. V. Nanopoulos, *Quantum-Gravitational Diffusion and Stochastic Fluctuations in the Velocity of Light*, General Relativity and Gravitation **32** (Jan., 2000) Jan. 127–144, arXiv:gr-qc/9904068 [gr-qc].

[18] R. Gambini and J. Pullin, *Nonstandard optics from quantum space-time*, Phys. Rev. D**59** (June, 1999) June 124021, arXiv:gr-qc/9809038 [gr-qc].

[19] G. Amelino-Camelia, *Relativity: Special treatment*, Nature**418** (July, 2002) July 34–35, arXiv:gr-qc/0207049 [gr-qc].

[20] G. Rosati, G. Amelino-Camelia, A. Marcianò, and M. Matassa, *Planck-scale-modified dispersion relations in FRW spacetime*, Phys. Rev. D**92** (Dec., 2015) Dec. 124042, arXiv:1507.02056 [hep-th].

[21] G. Amelino-Camelia, J. Ellis, N. E. Mavromatos, D. V. Nanopoulos, and S. Sarkar, *Tests of quantum gravity from observations of γ-ray bursts*, Nature**393** (June, 1998) June 763–765, arXiv:astro-ph/9712103 [astro-ph].

[22] J. Ellis, R. Konoplich, N. E. Mavromatos, *et al.*, *Robust constraint on Lorentz violation using Fermi-LAT gamma-ray burst data*, Phys. Rev. D**99** (Apr., 2019) Apr. 083009, arXiv:1807.00189 [astro-ph.HE].

[23] U. Jacob and T. Piran, *Lorentz-violation-induced arrival delays of cosmological particles*, J. Cosmology Astropart. Phys.**2008** (Jan., 2008) Jan. 031, arXiv:0712.2170 [astro-ph].

[24] G. Rosati, G. Amelino-Camelia, A. Marcianò, and M. Matassa, *Planck-scale-modified dispersion relations in FRW spacetime*, Phys. Rev. D**92** (Dec., 2015) Dec. 124042, arXiv:1507.02056 [hep-th].

[25] Planck Collaboration, P. A. R. Ade, N. Aghanim, *et al.*, *Planck 2015 results. XIII. Cosmological parameters*, A&A**594** (Sept., 2016) Sept. A13, arXiv:1502.01589 [astro-ph.CO].

[26] A. Cooray, *Extragalactic background light measurements and applications*, Royal Society Open Science **3** (Mar., 2016) Mar. 150555, arXiv:1602.03512 [astro-ph.CO].

[27] T. Terzić, D. Kerszberg, and J. Strišković, *Probing Quantum Gravity with Imaging Atmospheric Cherenkov Telescopes*, Universe **7** (2021) . https://www.mdpi.com/2218-1997/7/9/345.

[28] F. Piron, *Gamma-ray bursts at high and very high energies*, Comptes Rendus Physique **17** (June, 2016) June 617–631, arXiv:1512.04241 [astro-ph.HE].

[29] R. Margutti and R. Chornock, *First Multimessenger Observations of a Neutron Star Merger*, arXiv e-prints (Dec., 2020) Dec. arXiv:2012.04810, arXiv:2012.04810 [astro-ph.HE].

[30] I. A. Grenier and A. K. Harding, *Gamma-ray pulsars: A gold mine*, Comptes Rendus Physique **16** (Aug., 2015) Aug. 641–660, arXiv:1509.08823 [astro-ph.HE].

[31] J. Bell Burnell, *The past, present and future of pulsars*, Nature Astronomy **1** (Dec., 2017) Dec. 831–834.

[32] V. Beckmann and C. R. Shrader, *Active Galactic Nuclei*. 2012.

[33] P. Padovani, D. M. Alexander, R. J. Assef, *et al.*, *Active galactic nuclei: what's in a name?*, A&A Rev.**25** (Aug., 2017) Aug. 2, arXiv:1707.07134 [astro-ph.GA].

[34] R. Antonucci, *Unified models for active galactic nuclei and quasars.*, ARA&A**31** (Jan., 1993) Jan. 473–521.

[35] C. M. Urry and P. Padovani, *Unified Schemes for Radio-Loud Active Galactic Nuclei*, PASP**107** (Sept., 1995) Sept. 803, arXiv:astro-ph/9506063 [astro-ph].

[36] J. P. Norris and J. T. Bonnell, *Short Gamma-Ray Bursts with Extended Emission*, ApJ**643** (May, 2006) May 266–275, arXiv:astro-ph/0601190 [astro-ph].

[37] J. P. Norris, G. F. Marani, and J. T. Bonnell, *Connection between Energy-dependent Lags and Peak Luminosity in Gamma-Ray Bursts*, ApJ**534** (May, 2000) May 248–257, arXiv:astro-ph/9903233 [astro-ph].

[38] M. Ajello, M. Arimoto, M. Axelsson, *et al.*, *A Decade of Gamma-Ray Bursts Observed by Fermi-LAT: The Second GRB Catalog*, ApJ**878** (June, 2019) June 52, arXiv:1906.11403 [astro-ph.HE].

[39] A. Nepomuk Otte, *Prospects of performing Lorentz invariance tests with VHE emission from pulsars*, arXiv e-prints (Aug., 2012) Aug. arXiv:1208.2033, arXiv:1208.2033 [astro-ph.HE].

[40] G. Fossati, L. Maraschi, A. Celotti, A. Comastri, and G. Ghisellini, *A unifying view of the spectral energy distributions of blazars*, MNRAS**299** (Sept., 1998) Sept. 433–448, arXiv:astro-ph/9804103 [astro-ph].

[41] G. Ghisellini, C. Righi, L. Costamante, and F. Tavecchio, *The Fermi blazar sequence*, MNRAS**469** (July, 2017) July 255–266, arXiv:1702.02571 [astro-ph.HE].

[42] T. Hovatta and E. Lindfors, *Relativistic Jets of Blazars*, New A Rev.**87** (Dec., 2019) Dec. 101541, arXiv:2003.06322 [astro-ph.HE].

[43] M. Böttcher, *Progress in Multi-wavelength and Multi-Messenger Observations of Blazars and Theoretical Challenges*, Galaxies **7** (Jan., 2019) Jan. 20, arXiv:1901.04178 [astro-ph.HE].

[44] E. Fermi, *On the Origin of the Cosmic Radiation*, Phys. Rev. **75** (Apr, 1949) Apr 1169–1174. https://link.aps.org/doi/10.1103/PhysRev.75.1169.

[45] H. Che and G. P. Zank, *A Brief Review on Particle Acceleration in Multi-island Magnetic Reconnection*, in *Journal of Physics Conference Series*, vol. 1332 of *Journal of Physics Conference Series*, p. 012003. Nov., 2019. arXiv:1908.09155 [astro-ph.SR].

[46] D. A. Uzdensky, *Radiative Magnetic Reconnection in Astrophysics*, vol. 427, p. 473. 2016.

[47] G. B. Rybicki and A. P. Lightman, *Radiative processes in astrophysics*. 1979.

[48] M. S. Longair, *High Energy Astrophysics*. 2011.

[49] F. C. Jones, *Calculated Spectrum of Inverse-Compton-Scattered Photons*, Physical Review **167** (Mar., 1968) Mar. 1159–1169.

[50] F. A. Aharonian, D. Khangulyan, and L. Costamante, *Formation of hard very high energy gamma-ray spectra of blazars due to internal photon-photon absorption*, MNRAS**387** (July, 2008) July 1206–1214, arXiv:0801.3198 [astro-ph].

[51] S. Inoue and F. Takahara, *Electron Acceleration and Gamma-Ray Emission from Blazars*, ApJ**463** (June, 1996) June 555.

[52] W. B. Atwood, A. A. Abdo, M. Ackermann, *et al.*, *The Large Area Telescope on the Fermi Gamma-Ray Space Telescope Mission*, ApJ**697** (June, 2009) June 1071–1102, arXiv:0902.1089 [astro-ph.IM].

[53] N. Gehrels, G. Chincarini, P. Giommi, *et al.*, *The Swift Gamma-Ray Burst Mission*, ApJ**611** (Aug., 2004) Aug. 1005–1020, arXiv:astro-ph/0405233 [astro-ph].

[54] N. Otte, *Observation of VHE Gamma-Rays from the Vicinity of magnetized Neutron Stars and Development of new Photon-Detectors for Future Ground based Gamma-Ray Detectors*. PhD thesis, 09, 2007.

[55] C. Bigongiari, *The MAGIC telescope*, in *International Europhysics Conference on High Energy Physics, HEP2005*, p. 20. Jan., 2005. arXiv:astro-ph/0512184 [astro-ph].

[56] J. Holder, R. W. Atkins, H. M. Badran, *et al.*, *The first VERITAS telescope*, Astroparticle Physics **25** (July, 2006) July 391–401, arXiv:astro-ph/0604119 [astro-ph].

[57] K. Bernlöhr, O. Carrol, R. Cornils, *et al.*, *The optical system of the H.E.S.S. imaging atmospheric Cherenkov telescopes. Part I: layout and components of the system*, Astroparticle Physics **20** (Nov., 2003) Nov. 111–128, arXiv:astro-ph/0308246 [astro-ph].

[58] P. Hofverberg, R. Kankanyan, M. Panter, *et al.*, *Commissioning and Initial Performance of the H.E.S.S. II Drive System*, in *International Cosmic Ray Conference*, vol. 33 of *International Cosmic Ray Conference*, p. 3092. Jan., 2013. arXiv:1307.4550 [astro-ph.IM].

[59] B. Bi, M. Barcelo, C. Bauer, *et al.*, *Performance of the New FlashCam-based Camera in the 28\,m Telescope of H.E.S.S*, arXiv e-prints (Aug., 2021) Aug. arXiv:2108.03046, arXiv:2108.03046 [astro-ph.IM].

[60] M. de Naurois and L. Rolland, *A high performance likelihood reconstruction of γ-rays for imaging atmospheric Cherenkov telescopes*, Astroparticle Physics **32** (Dec., 2009) Dec. 231–252, arXiv:0907.2610 [astro-ph.IM].

[61] R. D. Parsons and J. A. Hinton, *A Monte Carlo template based analysis for air-Cherenkov arrays*, Astroparticle Physics **56** (Apr., 2014) Apr. 26–34, arXiv:1403.2993 [astro-ph.IM].

[62] A. M. Hillas, *Cerenkov Light Images of EAS Produced by Primary Gamma Rays and by Nuclei*, in *19th International Cosmic Ray Conference (ICRC19), Volume 3*, vol. 3 of *International Cosmic Ray Conference*, p. 445. Aug., 1985.

[63] T. Garrigoux, *Étude des emissions diffuses avec l'expérience H.E.S.S.* Theses, Université Pierre et Marie Curie - Paris VI, May, 2015. https://tel.archives-ouvertes.fr/tel-01208228.

[64] D. Berge, S. Funk, and J. Hinton, *Background modelling in very-high-energy γ-ray astronomy*, A&A**466** (May, 2007) May 1219–1229, arXiv:astro-ph/0610959 [astro-ph].

[65] G. P. Rowell, *A new template background estimate for source searching in TeV gamma -ray astronomy*, A&A**410** (Oct., 2003) Oct. 389–396, arXiv:astro-ph/0310025 [astro-ph].

[66] F. Piron, *Etude des propriétés spectrales et de la variabilité de l'emission gamma supérieure à 250 GeV des noyaux actifs de galaxies de type blazar observés dans le cadre de l'expérience C.A.T.* Theses, Université Paris Sud - Paris XI, May, 2000. https://tel.archives-ouvertes.fr/tel-00002448.

[67] Cherenkov Telescope Array Consortium, B. S. Acharya, I. Agudo, *et al.*, *Science with the Cherenkov Telescope Array*. 2019.

[68] R. D. Blandford and A. Königl, *Relativistic jets as compact radio sources.*, ApJ**232** (Aug., 1979) Aug. 34–48.

[69] A. P. Marscher and W. K. Gear, *Models for high-frequency radio outbursts in extragalactic sources, with application to the early 1983 millimeter-to-infrared flare of 3C 273.*, ApJ**298** (Nov., 1985) Nov. 114–127.

[70] A. Celotti, L. Maraschi, and A. Treves, *A Model for the Spectral Variability of BL Lacertae Objects at High Frequencies*, ApJ**377** (Aug., 1991) Aug. 403.

[71] K. Katarzyński, H. Sol, and A. Kus, *The multifrequency variability of Mrk 421*, A&A**410** (Oct., 2003) Oct. 101–115.

[72] M. Joshi and M. Böttcher, *Time-dependent Radiation Transfer in the Internal Shock Model Scenario for Blazar Jets*, ApJ**727** (Jan., 2011) Jan. 21, arXiv:1011.3113 [astro-ph.CO].

[73] T. R. Lewis, P. A. Becker, and J. D. Finke, *Time-dependent Electron Acceleration in Blazar Transients: X-Ray Time Lags and Spectral Formation*, ApJ**824** (June, 2016) June 108, arXiv:1603.07386 [astro-ph.HE].

[74] C. Perennes, H. Sol, and J. Bolmont, *Modeling spectral lags in active galactic nucleus flares in the context of Lorentz invariance violation searches*, A&A**633** (Jan., 2020) Jan. A143, arXiv:1911.10377 [astro-ph.HE].

[75] V. L. Ginzburg and S. I. Syrovatskii, *The Origin of Cosmic Rays*. 1964.

[76] K. Katarzyński, H. Sol, and A. Kus, *The multifrequency emission of Mrk 501. From radio to TeV gamma-rays*, A&A**367** (Mar., 2001) Mar. 809–825.

[77] T. M. Kneiske, K. Mannheim, and D. H. Hartmann, *Implications of cosmological gamma-ray absorption. I. Evolution of the metagalactic radiation field*, A&A**386** (Apr., 2002) Apr. 1–11, arXiv:astro-ph/0202104 [astro-ph].

[78] T. M. Kneiske, T. Bretz, K. Mannheim, and D. H. Hartmann, *Implications of cosmological gamma-ray absorption. II. Modification of gamma-ray spectra*, A&A**413** (Jan., 2004) Jan. 807–815, arXiv:astro-ph/0309141 [astro-ph].

[79] J. Albert, E. Aliu, H. Anderhub, *et al.*, *Variable Very High Energy γ-Ray Emission from Markarian 501*, ApJ**669** (Nov., 2007) Nov. 862–883, arXiv:astro-ph/0702008 [astro-ph].

[80] H. E. S. S. Collaboration, A. Abramowski, F. Acero, *et al.*, *A multiwavelength view of the flaring state of PKS 2155-304 in 2006*, A&A**539** (Mar., 2012) Mar. A149, arXiv:1201.4135 [astro-ph.HE].

[81] T. Takahashi, M. Tashiro, G. Madejski, *et al.*, *ASCA Observation of an X-Ray/TeV Flare from the BL Lacertae Object Markarian 421*, ApJ**470** (Oct., 1996) Oct. L89.

[82] A. Tramacere, P. Giommi, M. Perri, F. Verrecchia, and G. Tosti, *Swift observations of the very intense flaring activity of Mrk 421 during 2006. I. Phenomenological picture of electron acceleration and predictions for MeV/GeV emission*, A&A**501** (July, 2009) July 879–898, arXiv:0901.4124 [astro-ph.HE].

[83] A. U. Abeysekara, S. Archambault, A. Archer, *et al.*, *A Search for Spectral Hysteresis and Energy-dependent Time Lags from X-Ray and TeV Gamma-Ray Observations of Mrk 421*, ApJ**834** (Jan., 2017) Jan. 2, arXiv:1611.04626 [astro-ph.HE].

[84] M. Böttcher and M. G. Baring, *Multi-wavelength Variability Signatures of Relativistic Shocks in Blazar Jets*, ApJ**887** (Dec., 2019) Dec. 133, arXiv:1911.02834 [astro-ph.HE].

[85] M. Fairbairn, A. Nilsson, J. Ellis, J. Hinton, and R. White, *The CTA sensitivity to Lorentz-violating effects on the gamma-ray horizon*, J. Cosmology Astropart. Phys.**2014** (June, 2014) June 005, arXiv:1401.8178 [astro-ph.HE].

[86] T. C. Weekes, M. F. Cawley, D. J. Fegan, *et al.*, *Observation of TeV Gamma Rays from the Crab Nebula Using the Atmospheric Cerenkov Imaging Technique*, ApJ**342** (July, 1989) July 379.

[87] M. Punch, C. W. Akerlof, M. F. Cawley, *et al.*, *Detection of TeV photons from the active galaxy Markarian 421*, Nature**358** (Aug., 1992) Aug. 477–478.

[88] MAGIC Collaboration, J. Albert, E. Aliu, *et al.*, *Probing quantum gravity using photons from a flare of the active galactic nucleus Markarian 501 observed by the MAGIC telescope*, Physics Letters B **668** (Oct., 2008) Oct. 253–257, arXiv:0708.2889 [astro-ph].

[89] J. D. Scargle, J. P. Norris, and J. T. Bonnell, *An Algorithm for Detecting Quantum Gravity Photon Dispersion in Gamma-Ray Bursts: DisCan*, ApJ**673** (Feb., 2008) Feb. 972–980.

[90] V. Vasileiou, A. Jacholkowska, F. Piron, *et al.*, *Constraints on Lorentz invariance violation from Fermi-Large Area Telescope observations of gamma-ray bursts*, Phys. Rev. D**87** (June, 2013) June 122001, arXiv:1305.3463 [astro-ph.HE].

[91] S. D. Biller, A. C. Breslin, J. Buckley, *et al.*, *Limits to Quantum Gravity Effects on Energy Dependence of the Speed of Light from Observations of TeV Flares in Active Galaxies*, Phys. Rev. Lett.**83** (Sept., 1999) Sept. 2108–2111, arXiv:gr-qc/9810044 [gr-qc].

[92] B. Zitzer and VERITAS Collaboration, *Lorentz Invariance Violation Limits from the Crab Pulsar using VERITAS*, in *International Cosmic Ray Conference*, vol. 33 of *International Cosmic Ray Conference*, p. 2768. Jan., 2013. arXiv:1307.8382 [astro-ph.HE].

[93] T.-P. Li, J.-L. Qu, H. Feng, *et al.*, *Timescale Analysis of Spectral Lags*, Chinese J. Astron. Astrophys.**4** (Dec., 2004) Dec. 583–598, arXiv:astro-ph/0407458 [astro-ph].

[94] I. M. Dremin, O. V. Ivanov, and V. A. Nechitailo, *REVIEWS OF TOPICAL PROBLEMS: Wavelets and their uses*, Physics Uspekhi **44** (May, 2001) May 447–478, arXiv:hep-ph/0101182 [hep-ph].

[95] J. Ellis, N. E. Mavromatos, D. V. Nanopoulos, and A. S. Sakharov, *Quantum-gravity analysis of gamma-ray bursts using wavelets*, A&A**402** (May, 2003) May 409–424, arXiv:astro-ph/0210124 [astro-ph].

[96] M. Martínez and M. Errando, *A new approach to study energy-dependent arrival delays on photons from astrophysical sources*, Astroparticle Physics **31** (Apr., 2009) Apr. 226–232, arXiv:0803.2120 [astro-ph].

[97] P. Kaaret, *Pulsar radiation and quantum gravity*, A&A**345** (May, 1999) May L32–L34, arXiv:astro-ph/9903464 [astro-ph].

[98] F. Aharonian, A. G. Akhperjanian, U. Barres de Almeida, *et al.*, *Limits on an Energy Dependence of the Speed of Light from a Flare of the Active Galaxy PKS 2155-304*, Phys. Rev. Lett.**101** (Oct., 2008) Oct. 170402, arXiv:0810.3475 [astro-ph].

[99] H. E. S. S. Collaboration, A. Abramowski, F. Acero, *et al.*, *Search for Lorentz Invariance breaking with a likelihood fit of the PKS 2155-304 flare data taken on MJD 53944*, Astroparticle Physics **34** (Apr., 2011) Apr. 738–747, arXiv:1101.3650 [astro-ph.HE].

[100] M. Martínez and M. Errando, *A new approach to study energy-dependent arrival delays on photons from astrophysical sources*, Astroparticle Physics **31** (Apr., 2009) Apr. 226–232, arXiv:0803.2120 [astro-ph].

[101] H. Abdalla, F. Aharonian, F. Ait Benkhali, *et al.*, *The 2014 TeV γ-Ray Flare of Mrk 501 Seen with H.E.S.S.: Temporal and Spectral Constraints on Lorentz Invariance Violation*, ApJ**870** (Jan., 2019) Jan. 93, arXiv:1901.05209 [astro-ph.HE].

[102] M. Chrétien, J. Bolmont, and A. Jacholkowski, *Constraining photon dispersion relation from observations of the Vela pulsar with H.E.S.S*, in *34th International Cosmic Ray Conference (ICRC2015)*, vol. 34 of *International Cosmic Ray Conference*, p. 764. July, 2015. arXiv:1509.03545 [astro-ph.HE].

[103] MAGIC Collaboration, M. L. Ahnen, S. Ansoldi, *et al.*, *Constraining Lorentz Invariance Violation Using the Crab Pulsar Emission Observed up to TeV Energies by MAGIC*, ApJS**232** (Sept., 2017) Sept. 9, arXiv:1709.00346 [astro-ph.HE].

[104] V. A. Acciari, S. Ansoldi, L. A. Antonelli, *et al.*, *Bounds on Lorentz Invariance Violation from MAGIC Observation of GRB 190114C*, Phys. Rev. Lett.**125** (July, 2020) July 021301, arXiv:2001.09728 [astro-ph.HE].

[105] J. Ellis, N. E. Mavromatos, D. V. Nanopoulos, A. S. Sakharov, and E. K. G. Sarkisyan, *Robust limits on Lorentz violation from gamma-ray bursts*, Astroparticle Physics **25** (July, 2006) July 402–411, arXiv:astro-ph/0510172 [astro-ph].

[106] G. D'Amico, T. Terzić, J. Strišković, *et al.*, *Signal estimation in on/off measurements including event-by-event variables*, Phys. Rev. D**103** (June, 2021) June 123001, arXiv:2105.01019 [physics.data-an].

[107] The LHAASO Collaboration, *Exploring Lorentz Invariance Violation from Ultra-high-energy Gamma Rays Observed by LHAASO*, arXiv e-prints (June, 2021) June arXiv:2106.12350, arXiv:2106.12350 [astro-ph.HE].

Résumé:

Certains modèles de gravitation quantique, développés en vue d'une unification de la relativité générale et de la mécanique quantique, prédisent une violation de l'invariance de Lorentz (VIL) à l'énergie de Planck, induisant une vitesse des photons dans le vide dépendante de leur énergie. La VIL peut être sondée grâce à la recherche de délais temporels dépendant de l'énergie dans les émissions aux TeV de sources gamma distantes et variables telles que les noyaux actifs de galaxies, sursauts gamma et pulsars. Toutefois, des délais temporels peuvent également être générés par les processus radiatifs de ces sources qui nécessitent donc d'être étudiés, en particulier grâce à la modélisation des mécanismes d'émission. Ce manuscrit présente un modèle de blazar dépendant du temps basé sur un scénario leptonique, et l'étude des délais intrinsèques obtenus ainsi que leurs propriétés. De fortes corrélations et symétries entre les délais temporels dans les domaines des rayons X et gamma sont mises en évidence, qui peuvent être utilisées pour différencier les effets intrinsèques des effets de propagation. Contrairement au VIL, les délais intrinsèques ne dépendent pas directement de la distance de la source. Ces deux effets pourraient donc également être séparés grâce à une analyse multi-sources. Un consortium a été formé entre H.E.S.S., MAGIC et VERITAS afin d'élargir le catalogue de données exploitables. Un logiciel d'analyse poussée a été développé dans le but de tester et calibrer une nouvelle méthode standardisée de combinaison de données, menant à des contraintes sur l'échelle en énergie de gravitation quantique à la fois fortes et robustes.

Mots-clés: Astrophysique des hautes énergies; Blazars; Délais temporels; Modèle leptonique d'émission; Violation d'invariance de Lorentz;

Abstract:

Some models of quantum gravity, aiming at unifying general relativity and quantum mechanics, predict a Lorentz invariance violation (LIV) at Planck energy, expected to induce an energy-dependent velocity of photons in vacuum. One way to probe LIV is to look for energy-dependent time delays in the TeV gamma-ray signal coming from remote and variable cosmic sources such as active galactic nuclei, gamma-ray bursts and pulsars. However, time delays can also be generated from sources' radiative processes which are yet to be discriminated from LIV propagation effects. This distinction should be possible through the modelisation of sources emission mechanisms. This manuscript presents a time dependent leptonic model of blazar flares, and reviews the study of intrinsic time delays and their properties. Strong correlation and symmetry between time delays in the X-ray and gamma-ray domains are highlighted, which can be used to discriminate intrinsic from propagation effects. Contrary to LIV effects, intrinsic delays should not directly depend on the source distance. It should also be possible to separate both effects through population studies. A consortium between H.E.S.S., MAGIC and VERITAS experiments has been created to enlarge the catalog of usable datasets and combine them in a multi-source analysis. An advanced analysis software has been developed to test and calibrate a new standardised combination method, which is found to yield strong and robust constraints on the quantum gravity energy scale.

Key words: Very high energy astronomy; Blazars; Time delays; Leptonic emission model; Lorentz invariance violation;